UCLouvain

epl

École polytechnique de Louvain

Modeling and control of a root-growth experimental set-up

Author: **Noélie DENIS**
Supervisor: **Denis DOCHAIN**
Readers: **Xavier DRAYE, Robert DAVID**
Academic year 2023–2024
Master [120] in Mechanical Engineering

Abstract

In the context of climate change of today, analyzing the growth of plant roots is important regarding the optimization of the plant cultivation. Root growth takes place inside the soil so it is complex to observe. In the greenhouses of UCLouvain, an aeroponic observation method, known as RootPhAir platform has been developed. The aim of this thesis is to develop a dynamical model based on energy balance in the experimental set-up, and to design and implement a control strategy based on this model in order to control the temperature inside the chamber in spite of variations of the greenhouse temperature. This control is made by controlling the temperature of the misting solution. By making temperature measurements in the initial set-up and using methods of parameters identification, the model governing the energy transfer is established. A PI controller is simulated but not applied in practice. However, a circuit that cools down the misting solution is added. This permits to regulate as wanted the temperature inside the chamber. Nevertheless, it is not efficient in all situations.

Acknowledgments

I would like to express my gratitude to everyone who supported me in any way during the writing of this thesis,

My supervisor, Denis Dochain, always avalaible to help me understand and give me explanations and advice,

Xavier Draye, for its guidance to understand the experimental set-up,

Marc Migon, who provided me with temperature data of the greenhouse,

Adrien Banse and Donation Dumont, who helped me with the development of the dynamical model based on energy balance in the experimental set-up,

François Wielant, who helped me with the development of the temperature control strategy,

Thomas Dagbert, who helped me set up the cooling circuit,

Robert David, for agreeing to be on my jury,

My parents, for their sound advice and their supporting throughout the writing of my dissertation, and more generally during my studies.

And, my family and friends, for their constant support.

During the writing of this thesis, I acknowledge the use of ChatGPT 3.5 (OpenAI, https://www.openai.com/chatgpt) for rephrasing sentences, the use of DeepL Translator (https://www.deepl.com/en/translator) to translate text from French to English and the use of DeepLWrite (https://www.deepl.com/en/write) to paraphrase some sentences.

Contents

Glossary

α	Absorptivity	[-]
α	Thermal conductance	$\left[\frac{kJ}{sK}\right]$
α_{exp1}	Thermal conductance determined from experiment 1	$\left[\frac{kJ}{sK}\right]$
α_{exp2a}	Thermal conductance determined from experiment 2a	$\left[\frac{kJ}{sK}\right]$
α_{exp2b}	Thermal conductance determined from experiment 2b	$\left[\frac{kJ}{sK}\right]$
α_{exp2}	Thermal conductance determined from experiment 2	$\left[\frac{kJ}{sK}\right]$
α_{exp3}	Thermal conductance determined from experiment 3	$\left[\frac{kJ}{sK}\right]$
α_{mean}	Mean value of the thermal conductances determined from the experiments	$\left[\frac{kJ}{sK}\right]$
β	Factor of exchange between T_{in} and T	[-]
ΔT_e	Variation of the temperature of the greenhouse	$[°C]$
ΔT_{in}	Variation of the temperature of the misting	$[°C]$
ΔT_{R134a}	Difference between the temperatures of the refrigerant R134a at the entrance and the exit of the evaporator	$[°C]$
$\dot{m}$	Mass flux of the misted water	$\left[\frac{kg}{s}\right]$
$\dot{m}_{air}$	Mass flow rate of the air	$\left[\frac{kg}{s}\right]$
$\dot{m}_{exp2a}$	Mass flux of the misted water determined from the step response of experiment 2a	$\left[\frac{kg}{s}\right]$

$\dot{m}_{exp2b}$ Mass flux of the misted water determined from the step response of experiment 2b $\left[\frac{kg}{s}\right]$

$\dot{m}_{exp3}$ Mass flux of the misted water determined from the step response of experiment 3 $\left[\frac{kg}{s}\right]$

$\dot{m}_{mean}$ Mean value of the mass fluxes of the misted water determined from the step responses of experiments 2a, 2b and 3 $\left[\frac{kg}{s}\right]$

$\dot{m}_{R134a}$ Mass flow rate of the refrigerant R134a $\left[\frac{kg}{s}\right]$

$\dot{T} = \frac{dT}{dt}$ Time derivative of the temperature inside the chamber $\left[\frac{^\circ C}{s}\right]$

$\dot{T}_n$ Time derivative of the temperature inside the chamber at time t_n $\left[\frac{^\circ C}{s}\right]$

ϵ Emissivity [-]

ϵ_i Error term of the linear regression model $\left[\frac{kJ}{s}\right]$

$\eta_{HE,cold}$ Efficiency of the heat exchange between the refrigerant and the cooling solution (glycol-water mixture) at the evaporator and between the glycol-water mixture and the misting solution [−]

$\eta_{HE,hot}$ Efficiency of the heat exchange between the refrigerant and the air of the greenhouse at the condenser [−]

$\frac{dT_{filtered}}{dt}$ Time derivative of the filtered and sampled mean of the temperatures inside the chamber $\left[\frac{^\circ C}{s}\right]$

$\frac{dT_{filtered}}{dt}_{filtered}$ Filtered time derivative of the filtered and sampled mean of the temperatures inside the chamber $\left[\frac{^\circ C}{s}\right]$

γ Intercept of the linear regression model $\left[\frac{kJ}{s}\right]$

$\hat{\alpha}$ Estimate of the slope of the linear regression model $\left[\frac{kJ}{sK}\right]$

$\hat{\gamma}$ Estimate of the intercept of the linear regression model $\left[\frac{kJ}{s}\right]$

$\overline{x}$ Average of the n realizations x_i $[^\circ C]$

$\overline{y}$ Average of the n realizations y_i $\left[\frac{kJ}{s}\right]$

ρ_w Density of water 1000 $\left[\frac{kg}{m^3}\right]$

σ	Stefan Boltzmann constant	$5.67 \cdot 10^{-8} \left[\frac{W}{m^2 K^4}\right]$
τ	Time constant	$[s]$
τ_d	Closed-loop time constant	$[s]$
τ_i	Integral time constant	$[s]$
τ_r	Response time	$[s]$
θ	Delay	$[s]$
A	Area	$[m^2]$
$c_{p,air}$	Mass heat capacity of the air	$\left[\frac{kJ}{kgK}\right]$
$c_{p,R134a}$	Mass heat capacity of the refrigerant R134a	$\left[\frac{kJ}{kgK}\right]$
$c_{p,w}$	Mass heat capacity of liquid water at 20°C	$4.185 \left[\frac{kJ}{kgK}\right]$
COP	Coefficient of performance	$[-]$
E	Emissive power	$\left[\frac{W}{m^2}\right]$
E_b	Upper limit to the emissive power	$\left[\frac{W}{m^2}\right]$
F_N	Nyquist frequency	$[Hz]$
f_s	Sampling frequency	$[Hz]$
$f_{c,1}$	Cutoff frequency of the first experiment	$[Hz]$
$f_{c,2;3}$	Cutoff frequency of the Second and third experiments	$[Hz]$
G	Irradiation	$\left[\frac{W}{m^2}\right]$
$G_1(s)$	Transfer function between T and T^*	[-]
$G_2(s)$	Transfer function between T and T_e	[-]
$G_c(s)$	Transfer function of the PI controller	[-]
G_{abs}	Absorbed radiation	$\left[\frac{W}{m^2}\right]$
$G_{dy}(s)$	Transfer function between T and T^*	[-]

h	Convection heat transfer coefficient	$\left[\frac{W}{m^2K}\right]$
$H_1(s)$	Transfer function between T and T_{in}	[-]
$H_2(s)$	Transfer function between T and T_e	[-]
$H_a(s)$	Transfer function of the actuator	[-]
$H_m(s)$	Transfer function of the measurement system of the controlled variable	[-]
k	Thermal conductivity	$\left[\frac{W}{mK}\right]$
K_m	Transfer function which adjusts the dimensions of the set-point	[-]
K_p	Proportional gain	[-]
K_e	Gain between T and T_e	[-]
K_{in}	Gain between T and T_{in}	[-]
P_{comp}	Power consumed by the compressor	$[W]$
P_{evap}	Power absorbed by the refrigerant	$[W]$
P_{in}	Power released to cool the misting water	$[W]$
q''	Convective heat flux	$\left[\frac{W}{m^2}\right]$
Q_{air}	Heat absorbed by the air at the condenser	$[kJ]$
Q_{cold}	Heat released by the cooling solution (glycol-water mixture) at the evaporator and absorbed from the misting solution	$[kJ]$
Q_{cond}	Heat released by the refrigerant at the condenser	$[kJ]$
Q_{evap}	Heat absorbed by the refrigerant at the evaporator	$[kJ]$
Q_{in}	Heat released by the misting solution	$[kJ]$
q_x	Heat rate by conduction	$[W]$
q''_x	Heat transfer rate in the x-direction per unit area perpendicular to the direction of transfer	$\left[\frac{W}{m^2}\right]$
s	Complex frequency	[-]
T	Temperature inside the chamber	$[^\circ C]$

T^*	Set-point	$[°C]$
T_1	Temperature inside the chamber measured by the sensor s01	$[°C]$
T_2	Temperature inside the chamber measured by the sensor s02	$[°C]$
T_4	Temperature inside the chamber measured by the sensor s04	$[°C]$
T_5	Temperature inside the chamber measured by the sensor s05	$[°C]$
T_6	Temperature inside the chamber measured by the sensor s06	$[°C]$
T_e	Temperature of the greenhouse	$[°C]$
T_s	Surface temperature	$[K]$
T_∞	Fluid temperature	$[K]$
$T_{air,1}$	Temperature of the air at the entrance of the evaporator	$[°C]$
$T_{air,2}$	Temperature of the air at the exit of the evaporator	$[°C]$
T_{cold}	Temperature of the glycol-water mixture	$[°C]$
$T_{e,filtered}$	Filtered and sampled temperature of the greenhouse	$[°C]$
$T_{e,measured}$	Temperature of the greenhouse outside the chamber measured by the probe of the "ARIA" supervision system of the greenhouses	$[°C]$
$T_{e,sampled}$	Sampled temperature of the greenhouse	$[°C]$
$T_{filtered}$	Filtered and sampled mean of the temperatures inside the chamber	$[°C]$
$T_{in,filtered}$	Filtered and sampled temperature of the misting solution	$[°C]$
$T_{in,measured}$	Temperature of the misted solution measured by the sensor s08	$[°C]$
$T_{in,sampled}$	Sampled temperature of the misting solution	$[°C]$
$T_{in,simulated}$	Temperature of the misted solution simulated	$[°C]$
$T_{in,1}$	Temperature of the misting solution at the entrance of the cooler	$[°C]$
$T_{in,2}$	Temperature of the misting solution at the exit of the cooler	$[°C]$
$T_{in,exp2a}$	Approximation of the temperature of the misting during experiment 2a	$[°C]$

$T_{in,exp2b}$ Approximation of the temperature of the misting during experiment 2b $[°C]$

$T_{in,exp3}$ Approximation of the temperature of the misting during experiment 3 $[°C]$

T_{in} Temperature of the misting $[°C]$

T^*_{in} Reference term $[°C]$

T_{mean} Mean value of the temperatures measured by the five sensors inside the chamber $[°C]$

T_{n+1} Temperature inside the chamber at time t_{n+1} $[°C]$

T_n Temperature inside the chamber at time t_n $[°C]$

$T_{R134a,1}$ Temperature of the refrigerant R134a at the exit of the evaporator $[°C]$

$T_{R134a,2}$ Temperature of the refrigerant R134a at the entrance of the condenser $[°C]$

$T_{R134a,3}$ Temperature of the refrigerant R134a at the exit of the condenser $[°C]$

$T_{R134a,4}$ Temperature of the refrigerant R134a at the entrance of the evaporator $[°C]$

T_{ref} Temperature of reference measured by a thermometer during the verification of the sensors $[°C]$

T_{s0i} Temperature measured by the sensor i during the verification of the sensors $[°C]$

$T_{sampled}$ Sampled mean of the temperatures inside the chamber $[°C]$

$T_{simulated}$ Temperature inside the chamber simulated $[°C]$

V Active volume of the chamber $4.6951[m^3]$

x Abscissa coordinate in a Cartesian coordinate system [-]

x_i Independent realization observed $[°C]$

y Ordinate coordinate in a Cartesian coordinate system [-]

y_i Dependent realization observed $\left[\frac{kJ}{s}\right]$

COPO Copolymer

CT Computed tomography

MRI Magnetic resonance imaging

PI Proportional-integral

PP Polypropylene

URI Uniform Resource Identifier

List of Figures

List of Tables

Chapter 1

Introduction

This thesis is concerned with the operation and control of an experimental set-up designed for studying the growth of plant roots. Analyzing the growth of plant roots is complex when considering that the root growth takes place inside the soil. A new experimental set-up to observe this growth has been developed a few years ago by researchers at UCLouvain. The problem with this device is that the temperature inside it is too much influenced by the temperature of the greenhouse which is in turn influenced by the outside temperature. For an optimal development of the roots, the temperature in the set-up needs to be as constant as possible and independent of the outside temperature.

The objectives of the study is to develop a dynamical model based on energy balance in the experimental set-up, and to design and implement a control strategy based on this model in order to control the temperature inside the chamber in spite of variations of the greenhouse temperature.

Chapter 2 gives an overview of the utility of observing the growth of the roots of plants and of the different ways of doing it.
Chapter 3 describes the set-up, his functioning and experiments measuring the temperatures that will be important for the rest of this thesis.
Chapter 4 develops the dynamical model of energy transfer in the experimental set-up on the basis of the measured temperatures.
Chapter 5 describes the design of a control strategy of the temperature inside the set-up based on the dynamical model.
Chapter 6 describes the practical implementation of the solution retained to regulate the temperature inside the experimental set-up.
Chapter 7 concludes the master thesis by summarize the study and results. It ends with prospects for improvement.

Chapter 2

Plant root growth

2.1 Overview

The objective of this chapter is to describe the experimental set-up dedicated to the study of the growth of plant roots.

Firstly, the motivation for studying plant root systems is presented. It develops the context of today in which optimizing the plant cultivation is becoming important. Then, the chapter presents various methods for observing plant root growth, ranging from field-based techniques to controlled environment methods such as aeroponics. The latter is the type of method to which the experimental set-up corresponds. Each method is discussed in terms of its applications, advantages and limitations.

2.2 Motivation for root observation

Agriculture is highly sensitive to climate change due to its dependence on weather conditions, leading to significant economic impacts. Variations in temperature, rainfall, and CO_2 levels affect the performance differently based on the crop type, location, and extent of climate change. Rising temperatures, extreme weather events and drought areas reduce crop yields, while increased precipitation can sometimes mitigate this effect. Despite some areas potentially benefiting from climate change through increased yields, these regional gains are unlikely to offset the overall negative impacts. Pest and disease prevalence is expected to rise with climate change, particularly in warmer, humid regions. This will lead to increased pesticide costs and potential crop damage, affecting both developed and developing countries. Weed growth and competition with crops will also be influenced by climate change. In fact, changes in climate conditions may also affect herbicide efficiency and open new geographical areas to weed infestations, necessitating new

management practices [21].
Whether it is about natural ecosystems or cultivated fields, the goal is to try to predict how they will behave with the very rapid climate changes. Adaptive strategies and improved irrigation practices are essential to mitigate these impacts and ensure agricultural sustainability. All farmers, all processing chains and all machinery must be adapted to climate change. Some will have to be shut down, and new ones built [3].

The integration of genetic, physiological, and ecophysiological knowledge is essential for developing agricultural practices that are resilient to climate change. By combining insights from these disciplines, plant-soil interactions can be better understood and strategies to improve crop performance under less than optimal conditions can be developed. This integrated approach will help ensure that agriculture remains sustainable and productive in the face of rapid environmental changes [14].

2.2.1 Genetics of plants

Plant genetics focuses on the study of genes, genetic variation, and heredity specifically in plants. It encompasses the molecular and cellular mechanisms of gene expression, inheritance patterns, and how genetic traits are passed from one generation to the next. This field also explores plant breeding, genetic modification, and biotechnology applications to improve crop yield, disease resistance, and stress tolerance. Plant genetics involves studying DNA sequences and mutations that impact plant traits and how these can be manipulated for agricultural advancements [31].

Genetics has been a cornerstone of plant selection for a long time. Humans began selecting plants when they domesticated them. By selecting the best plants for the next generation, populations gradually evolved. In the last century, this selection process, initially carried out by farmers, was taken over by research institutes and companies. They create varieties through selection and crossbreeding. All plants of the same variety are like clones and are sold to farmers based on their properties and performance under specific conditions. Companies cross various plants to generate new combinations, evaluating and selecting those with the best yield to become new varieties. A variety typically stays on the market for only a few years. This technique has improved performance under optimal conditions, such as irrigating when there is a lack of water and adding fertilizer when needed. However, future agriculture aims to reduce the use of fertilizers, irrigation, pesticides and other aspects. Thus, the focus is shifting towards disease resistance, which is currently the subject of extensive research in laboratories but is not yet integrated

into breeding companies [9].

No selection has been made for root parameters because roots are not easily observable in the field. Even if they could be observed, it would not be known which characteristics are important: Longer or shallower roots? Longevity? Root diameter? The goal is to determine if root characteristics are useful and heritable. If not, selecting for them would be pointless [22].

Genetic studies have provided valuable insights into the genetic basis of root growth and development. Atkinson et al. revealed genetic determinants of root traits associated with improved plant performance. Trait selection strategies have been developed to enhance root systems and water uptake in crops, contributing to the development of drought-tolerant and resource-efficient varieties [5].

2.2.2 Physiology of plants

Plant physiology is the study of how plants function. It covers various physiological processes including photosynthesis, respiration, mineral nutrition, water transport, and plant development. This field examines the biochemical and physical processes within plants that enable them to grow, reproduce, and respond to their environment. Physiology aims to understand the factors causing a root to branch out at certain times. Understanding these factors will help predict how a plant will adapt to different soils. This knowledge is crucial for developing plants that can thrive under varying environmental conditions [15].

The principal organs of a plant are the roots, the stems, the leaves, the flowers and the fruits. The main regions of a root are the stele, containing the phloem, the xylem, the pericycle and the endodermis, the cortex and the epidermis [15]. These parts can be seen on Figure 2.1.

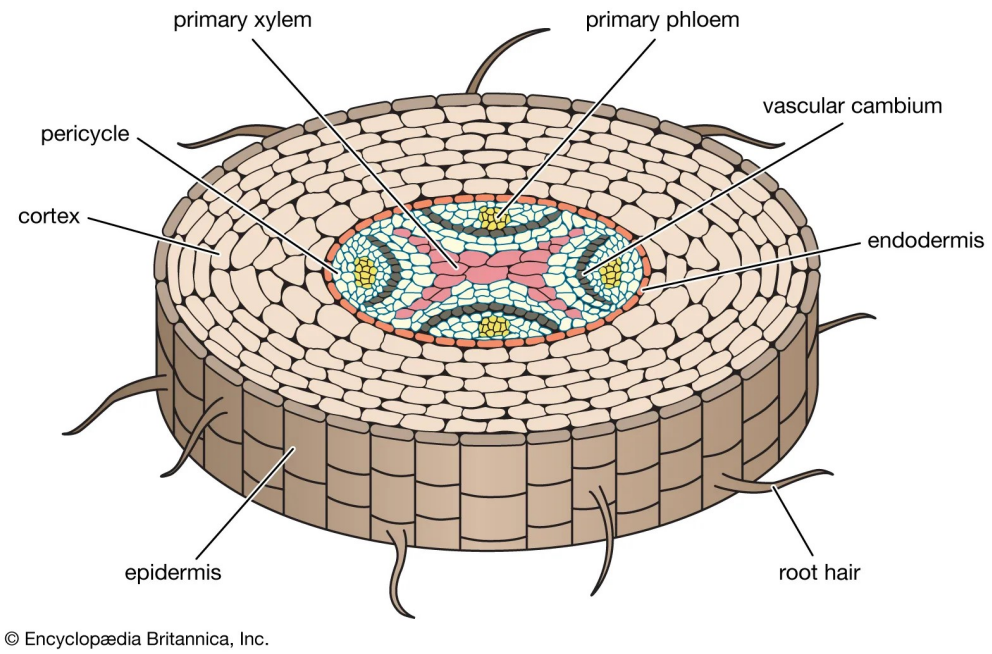

Figure 2.1: Cross section of a root [32]

Roots have four main functions. Firstly, they anchor the plant in the soil. Secondly, they act as a storage site for carbohydrates and organic molecules. Thirdly, they are where important molecules such as alkaloids or certain hormones are synthesized. Finally, they absorb and transport almost all the water and minerals absorbed by the plant to the stems [15].

The conduction of water and minerals in the vascular plants, also called tracheophytes, is handled by the conductive tissues, the xylem and the phloem. The xylem ensures the vertical transport of water, of dissolved minerals and sometimes of small organic molecules from roots to organs, from photosynthetic sites to storage sites or sites of high metabolic activity. The phloem ensures the transport of organic materials, from photosynthetic sites to storage sites or sites with high metabolic activity [15].

Plants draw their nutrients from the soil solution using the root system, with the exception of carbon and oxygen, which are supplied in the form of carbon dioxide from the air [15].

2.2.3 Ecophysiology of plants

Plant ecophysiology examines how plants interact with their physical environment and adapt to various environmental conditions. It merges aspects of ecology and plant physiology to understand how environmental factors like light, temperature, water availability, and soil conditions affect plant growth, physiology, and survival. This field studies plant responses to environmental stressors and how plants optimize their physiological processes to grow in different habitats.
Ecophysiology focuses on understanding where the root layers are located within a field, rather than just in a single plant. This discipline considers broader scales, such as a one-hectare field. It aims to demonstrate that in somewhat dry years, yield is directly proportional to the amount of water transpired [1].

In order to maintain the turgidity of leaf tissues and biochemical activities at a level compatible with survival, the water lost by plants during transpiration must be continuously resupplied. Many plants are capable of absorbing moisture from the air in the form of mist or dew, but leaf water absorption is negligible compared to root absorption.
The absorption by the root system creates a continual flow of water from the soil to the atmosphere through the plant, forming what is commonly referred to as the soil-plant-atmosphere continuum. This concept of the soil-plant-atmosphere continuum reinforces the observation that plants are not isolated organisms but are closely interconnected with their environment [15].

In order to understand the interactions between roots and soil water, it is useful to understand the nature of soils. Soil is an extremely complex medium. It consists of a solid phase made up of particles derived from parent rocks, organic matter at various stages of decomposition, a liquid phase composed of water or soil solution, gases in equilibrium with the atmosphere and a multitude of microorganisms. The solid phase, particularly the mineral particles, constitutes the primary source of nutrients. During rock decomposition, various elements are released into the soil solution, which then serves as the source of nutrients to be absorbed by plants. However, the soil solution is highly diluted (the total mineral content is on the order of $10^{-3}M$) and would quickly be depleted of nutrients if the solid phase did not continuously reconstitute it [15].

2.3 Methods to observe plant root growth

In the previous section, the motivations for observing plant roots were discussed. It highlighted their crucial role in water and nutrient uptake, plant anchorage and

interactions with soil microorganisms. Understanding root growth and development is essential solving the processes underlying plant development and optimizing agricultural practices. Over the years, researchers have employed various methods and techniques to observe and analyze root growth, ranging from traditional approaches to cutting-edge technologies [30]. This section explores a range of these methods, highlighting their applications, advantages and limitations.

2.3.1 Field-based methods

Rhizotrons

Rhizotron systems are growth chambers with one transparent wall, typically made of glass or clear plastic. Plants are grown with their roots adjacent to this wall, allowing researchers to directly observe and photograph root development over time [30].
An example of configuration is to put a seed, a blue fabric and a substrate between two plates. The blue fabric serves as a contrast with the root to better observe it. Behind this fabric, the substrate is humidified to feed the plant.
An alternative is to only have the plant, the fabric and a plastic film. This setup is put on a vertical plate and the bottom of the fabric soaks in water.

Rhizotrons is a non-destructive method which allows for continuous monitoring without disturbing the root environment. In fact, it provides a clear view of root development and growth patterns. It can be used in controlled environment conditions [30].

The problem with this method is that it cannot be used with very old plants. In fact, after 10-15 days, mushrooms begin to develop because it is not a sterile system and the roots quickly reach the ends of the plates. Moreover, the roots may alter their growth behavior due to the proximity to the transparent wall [30].

Minirhizotron systems

Minirhizotrons involve inserting a transparent tube into the soil. The tube is closed at both ends and once in a while, the cover is removed and a specialized camera or scanner is slid in to capture images of the roots growing along the tube's inner surface.
There are different types of minirhizotrons depending of the type of tube. Solid tubes are made from materials like glass, acrylic, polybutyrate and polycarbonate. Flexible or pressurized tubes are designed to withstand soil movements and pressures [20][30].

However, the problem with minirizotrons lies in the small sample size they examine. In a large and heterogeneous field, the soil conditions, root distribution, and plant interactions can vary significantly across different areas. Minirhizotrons typically observe a very narrow and specific section of the soil. This small sample might not accurately represent the diversity of root systems and soil interactions across the entire field. As a result, the data collected may provide an insufficient and unrepresentative view of the root system and soil interactions [24][30].

An altervative is then to install minirhizotron networks which is deploying multiple minirhizotron tubes across a field or experimental plot. This enables researchers to monitor root growth and interactions at multiple locations simultaneously, providing a high-throughput approach to studying root systems in the field.

Shovelomics

Shovelomics involves the rapid and systematic excavation of roots with a shovel to quantitatively assess root traits. A shovel is used to dig around a plant and pull it out. Measurements of angles, diameters, numbers, etc., can be taken. The different steps can be seen on Figure 2.2. This method retrieves primarily the superficial part of the root system. It enables the phenotyping of large plant populations in the field. It is quick and relatively inexpensive compared to advanced imaging methods but is less detailed. However, this technique does not provide information on root depth, which is crucial for understanding the water stock accessible to the plant [4][33].

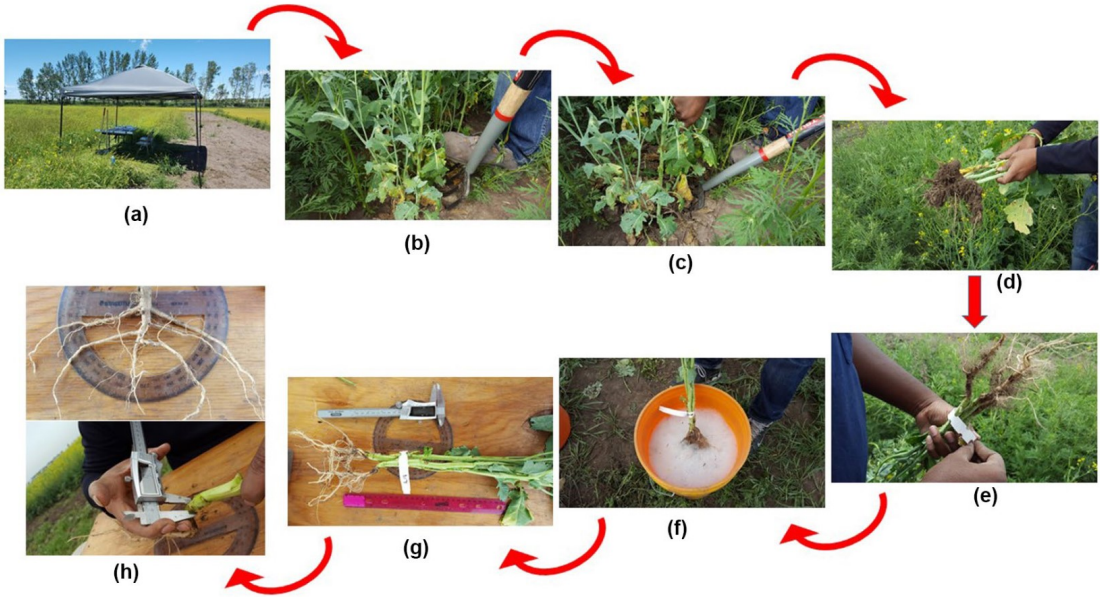

Figure 2.2: Phenotyping procedure of shovelomics: (a) Field work station, (b) selection of representative plants and excavation, (c) excavation, (d) dart clearing, (e) tagging, (f) washing, (g) phenotyping board, (h) data collection [4]

2.3.2 Controlled environment methods

Unlike field-based high-throughput methods, which involve studying root systems in their natural environment, these laboratory-based methods typically provide more controlled conditions for root observation and experimentation [30].

The aim of controlled environment methods is to be independent from the soil and its heterogeneity and to have a homogeneous environment. The roots are flexible, in function of the type of soil they see around them, they are going to change their behavior. They are going to speed up, slow down, turn left or right, branch out or not.
When a root system is removed from the soil, almost everything is broken. What can be derived intact is a map of the soil properties reflected by the root, rather than what the root actually is.
There are chemical reactions at the surface of the roots that, in soil, influence the water film. Notably, the pH and the amount of sugar are modified and thus micro-organisms grow. It is avoided in controlled environment methods.
They permit a precise control over environmental conditions, but the fact that roots are not growing in natural soil conditions may affect their development [30].

Hydroponics

In hydroponic systems, plants are grown with their roots submerged in a nutrient solution instead of soil. There is a large volume of water for a small surface area of roots, so that the roots do not influence the solution.
The nutrient solution permits that here is no need to feed the plants regularly but some species can be drowned. To avoid this, a small hose and an aquarium pump are used to oxygenate the water a bit [29].

This method facilitates easy access to the roots for observation, measurement and precise control over nutrient, water supply and environmental conditions. It facilitates the study of root physiology, nutrient uptake, and responses to abiotic stresses.
The problem with hydroponics is that nothing can be measured on the root parts, but well on the aerial parts [29].

Aeroponics

Aeroponic systems suspend plant roots in the air and periodically mist them with a nutrient solution.
In hydroponics, the roots float and clump together so they cannot be seen. In aeroponics, the view of roots is unobstructed. There is no constraint around the roots, no substrate, nothing is going to slow down, speed up or force a direction of the growth [19].

The issue with this method arises from the fact that all plants share the same artificial environment. For example, studying how 50 different varieties of wheat respond to varying levels of nitrogen requires observing the reaction of each plant's root system to different nitrogen concentrations. To achieve this, each wheat variety needs its own controlled environment to isolate the effect of nitrogen levels. In aeroponics, this would necessitate 50 separate containers or "boxes," with each box dedicated to a specific wheat variety and a particular nitrogen concentration. These boxes are typically large, occupy significant space, and each can only hold one type of nutrient solution at a time.

Magnetic resonance imaging (MRI)

MRI uses magnetic fields and radio waves to create high-resolution images of root systems and soil water content without the need for ionizing radiation. It is highly effective for studying living tissues and their interactions with the environment.
A column containing the plant is placed in the MRI scanner. This gives a 3D map of the presence of water. The roots appear as black spots because they are filled

with water [30].

However, MRI is expensive and requires non-metallic environments. The equipment is also sensitive to external magnetic fields and requires careful calibration. In addition, this analysis is done on small volumes and the acquisition time is still relatively long (30 minutes to 1 hour) [30].

X-ray computed tomography (CT)

X-ray CT uses X-rays to create cross-sectional images of roots within the soil, providing high-resolution, three-dimensional visualizations [37]. Mooney et al. showcased the utility of X-ray CT for non-invasive imaging of root systems [23].

The primary limitations include high costs, the need for sophisticated equipment and potential safety concerns related to X-ray exposure [30].

Chapter 3

Initial set-up

3.1 Overview

The previous chapter provided an overview of the importance of observing and analyzing plant root growth. The experimental set-up analyzed in this thesis is an aeroponic observation method.

The aim of this chapter is to describe this experimental facility, known as the RootPhAir platform.

Firstly, the functioning and various components of the platform are described. Next, experiments were carried out in order to collect data on the temperatures in the greenhouse and in the chamber in order to analyze temperature variations and heat exchanges in the next chapter. The procedure followed and the equipment used are described. The first rough results are given.

3.2 Experimental setup

The experimental chamber serves as a controlled environment for observing and analyzing the growth of plant roots in aeroponics. The following is a detailed description of the chamber and its components.
There are two chambers situated in a room of the greenhouses at UCLouvain in Belgium (50°39'56"N 4°37'10"E; Elevation 143.08 m [12]). A scheme of this room can be seen on Figure 3.1A). The greenhouse room has the following dimensions: length of 8 m, width of 8 m and height of 4 m. The chambers are two identical aeroponics boxes (Box A and Box B) [10]. The dimensions of the chambers can be found in Appendix A. The material used to build the boxes is polypropylene copolymer (PP COPO) [25]. Its typical value of thermal conductivity is $0.1 - 0.22 \frac{W}{mK}$

[27].

Each box has a capacity of 495 plants because it contains 99 strips capable of holding five plants each. The strips are polystyrene rectangles that have holes. The seed of the plants are set in Peat Foam plugs (inert material) inside these holes. This can be seen on Figure 3.1B) where the plugs are depicted in orange and the strips in blue [10].

To prevent root entanglement caused by the increasing weight of the root systems as plants grew, lightweight plastic structures are installed beneath each plant. These structures were carefully designed to minimize interference with root growth and to have minimal impact on image quality. A structural design example is presented on Figure 3.1B) [10].

This setup that includes the two aeroponic units is called RootPhAir platform and is a high throughput root phenotyping system designed for observing root system growth in aeroponics. The roots develop in a substrate-free environment, that is to say in the absence of mechanical constraints [10].

According to a researcher, the roots that can be observed in this setup need to be thick enough (diameter of more than 0.3 mm) because otherwise the roots are dragged along with the water droplets of the fogged solution and stick to the plastic structure that is under the plants. The root system development is no longer sufficiently visible. For example, plants like cereals, barley, wheat, rice, corn, beet and soybeans can be observed in the setup.

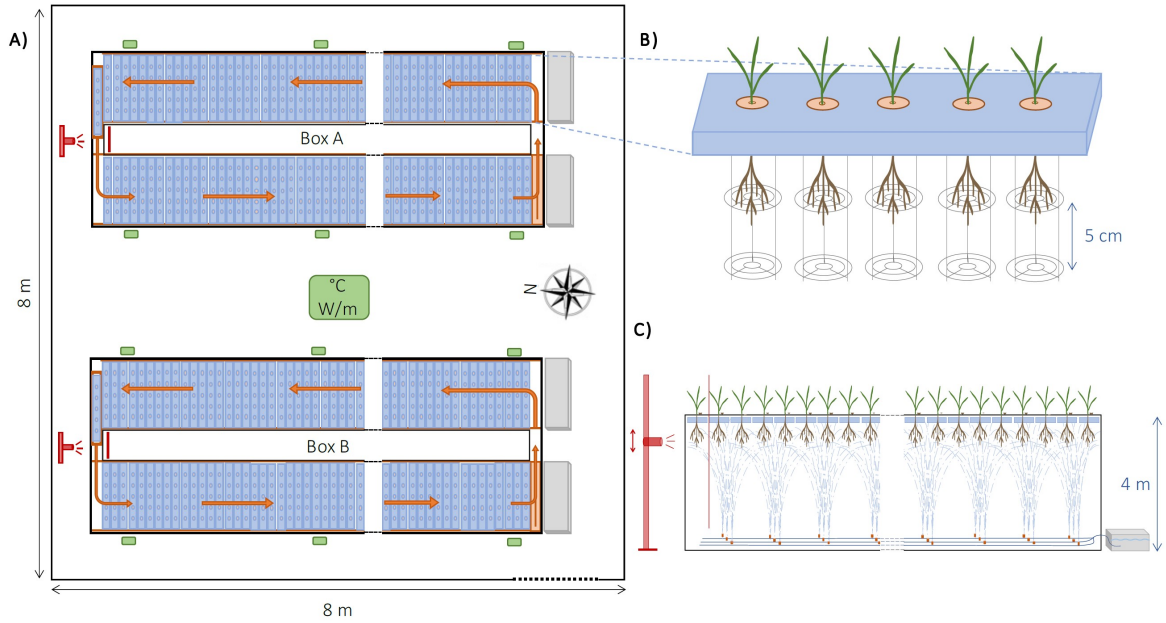

Figure 3.1: Schematic views of the RootPhAir platform: A) Aerial view illustrating the arrangement of the greenhouse layout accommodating two aeroponic boxes; B) Zooming in on one strip capable of accommodating five plants; C) Cross section of one aeroponic box [10]

3.2.1 Misting

A misting system is integrated into the chamber to provide a fine mist of nutrient solution directly to the root zone of plants. This system ensures that plant roots receive adequate moisture and nutrients for optimal growth and development. The misting system can be programmed to deliver precise amounts of nutrient solution at specified intervals.
The nutritive solution is fogged from the bottom of the chambers. It contains nutrients and water to feed the plants. The cross-sectional representation of one aeroponic box can be seen on Figure 3.1C). It shows sprayers positioned beneath the roots, with the four tanks containing the nutritive solution connected to them situated on one side of the box (illustrated in grey) [10].

The circuit of the misting is depicted on Figure 3.2. The solution is pumped from the reservoir tanks (illustrated in grey) by a pump (P) and passes through filters (F1 and F2) to evacuate some impurities. When the electrovalve (EV1) is opened, the pressure rises in the misting bars and the water comes out through the nozzles. This is a misting episode. There are 28 misting nozzles spread all over the soil of

the aeroponic box (illustrated in green). The misting water that percolates down the walls and roots falls to the bottom of the chamber. Its floor slopes slightly towards the two water tanks and has two collectors at its lowest point, which in turn are connected to the tanks. Excess water therefore ends up in the water tanks.

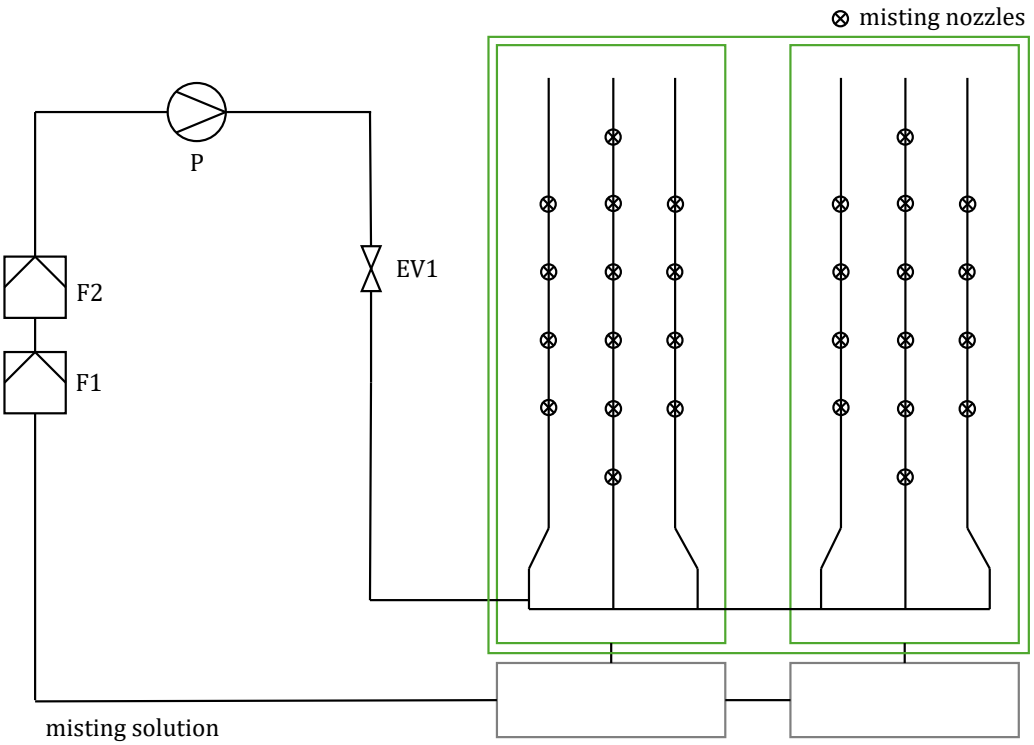

Figure 3.2: Scheme of the misting circuit

3.2.2 Imaging system

The chamber is equipped with a digital camera for capturing high-resolution images of root growth. It features a back-light scanning setup with a monochrome high-resolution horizontal linescan camera (4K, Teledyne Dalsa, Spider) that moves vertically in front of a red backlight. It is depicted on Figure 3.1C). This configuration yields images characterized by high contrast, with dark root pixels and clear background pixels (see Figure 3.3). About 130 images per root system are captured for an experiment lasting two weeks. In fact, given the time needed to scan 495 plants, the revolution period (and temporal phenotyping resolution) is approximately 2 hours. Each plant has a unique URI (Uniform Resource Identifier) to be identified. The plants are continuously moved inside the aeroponic boxes by conveyors. This provides the throughput needed to record dense time series. On Figure 3.1A), the direction of rotation of the 99 strips can be seen in orange and the position of the camera in red. The platform's complete automation is managed by in-house software programs [10].

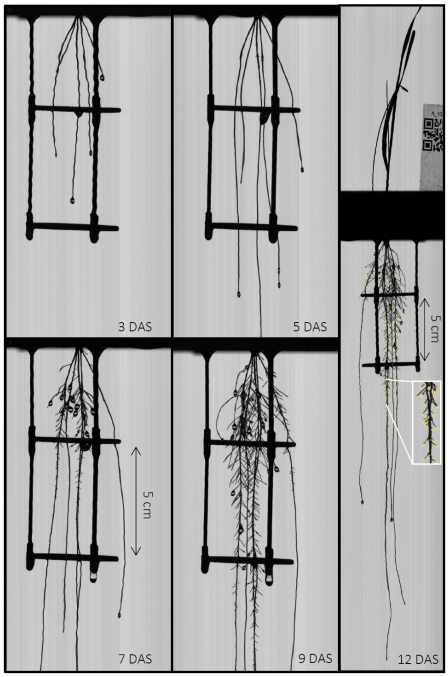

Figure 3.3: Example of images taken by the camera in the RootPhAir platform [10]

3.3 Temperature measurements

The objective of the experiments is to observe the relations between the variation of temperatures inside the chamber (T_1, T_2, T_4, T_5 and T_6), outside the chamber ($T_{e,measured}$) and the temperature of the misting ($T_{in,measured}$).
In order to achieve this, three different experiments were conducted. The first one consists of controlling the temperature of the greenhouse and the two others controlling the temperature of the misting. A detailed description of the different experimental conditions and variables is made in 3.3.2.

The misting system does on for 15 seconds, then stops during 105 seconds, and this cycle repeats during all experiments.

The procedure for collecting temperature data involved the following steps:

- Temperature sensors were connected to a data acquisition system capable of recording temperature measurements at regular intervals.
- For each experiment, the greenhouse or misting temperature was set to a predetermined level.
- Temperature data were collected continuously throughout the duration of each experiment.
- Finally, the accuracy of the measurements done by the sensors were verified.

3.3.1 Material

The following tools and instruments were used for data acquisition during the experiments:

Sensors

Temperature sensors were placed at different heights and distances from heat sources inside the chamber to ensure coverage of temperature gradients. The sensors that were used are DS18B20 digital thermometers. They provide temperature measurements ranging from 9 to 12 bits in Celsius and feature an alarm function with customizable upper and lower trigger points that persist even when power is off. They operate over a 1-Wire bus, so they require only one data line (along with ground) for communication with a central microprocessor. Furthermore, an external power supply is not needed because the sensors draw power directly from the data line. Finally, each DS18B20 possesses a unique 64-bit serial code. Multiple units can operate on the same 1-Wire bus. This facilitates the use of a single microprocessor to oversee numerous sensors spread across a wide area [2].

The different sensors that were installed in the greenhouse are shown on Figure 3.4. The sensor s08 is the one connected to the start of the misting solution that comes from the external water supply.

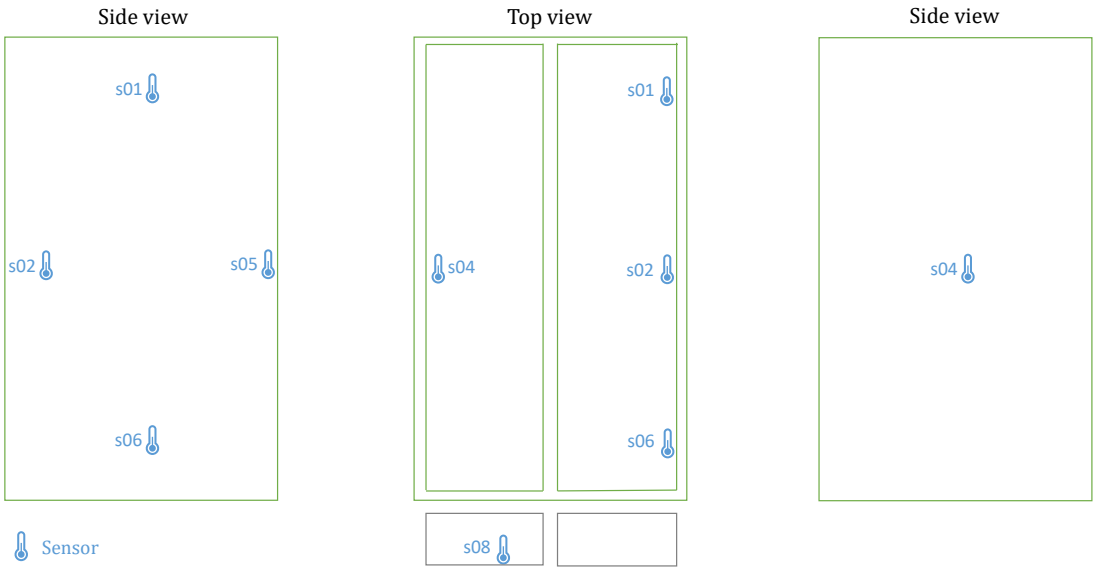

Figure 3.4: Schematic of the placement of the sensors inside and outside the experimental set-up

Data acquisition system

A data acquisition system, comprising a Raspberry Pico, was used to collect and record temperature data from the sensors.
The data acquisition system was configured to record temperature data from the sensors every 10 seconds. Some measurements have an interval of 11 seconds. This is explained in 4.3.2.

Computer interface

A computer interface permits to start and stop the logger.

Reference thermometer

A reference thermometer was used to verify temperature sensors after data collection.

3.3.2 Data collection

All the data collected during the experiments and the time between them can be seen on Figure 3.5. The first experiment took place between 6 a.m. on October 19, 2023 and 9 a.m. on October 20, 2023, the second experiment between 11:16 a.m.

and 1:56 p.m. on October 20, 2023 and the third experiment between 2:23 p.m. and 5:16 p.m. on October 20, 2023. The different measured temperatures are the following:

- T_1: Temperature inside the chamber measured by the sensor s01.
- T_2: Temperature inside the chamber measured by the sensor s02.
- T_4: Temperature inside the chamber measured by the sensor s04.
- T_5: Temperature inside the chamber measured by the sensor s05.
- T_6: Temperature inside the chamber measured by the sensor s06.
- $T_{in,measured}$: Temperature of the misted solution measured by the sensor s08. An assumption is made that no heat is lost in the circuit from the reservoir tank to the chamber.
- $T_{e,measured}$: Temperature of the greenhouse measured by the probe of the "ARIA" supervision system of the greenhouses.

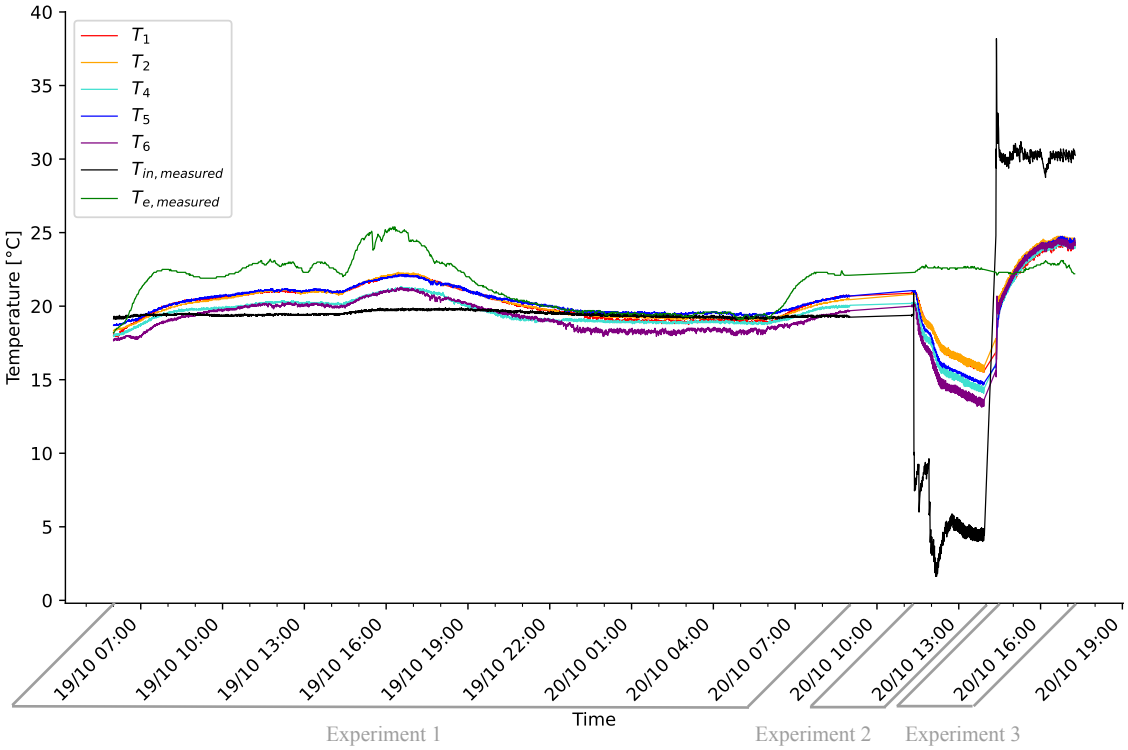

Figure 3.5: Temperatures measured by the sensors during the three experiments

Experiment 1: Variation of greenhouse temperature

During the first experiment, the temperature of the greenhouse is being varied, while the temperature of the misting is nearly constant coming from tap water at around 19.5°C. It permits to observe the effect of the greenhouse temperature on the temperatures measured by the sensors inside the chamber.
The requested temperature in the greenhouse was set on 22°C from 6 a.m. to 2 p.m. on October 19, 2023. Then, until 6 a.m. on October 20, 2023, the instruction was set on 5°C. From 6 a.m. to 9 a.m. on October 20, 2023, the requested temperature was again set on 20°C. The actual temperature inside the greenhouse T_e is given by the probe of the "ARIA" supervision system of the greenhouses. It can be seen, on Figure 3.6, that when 22°C is requested, $T_{e,measured}$ is close to the set point. However, the instruction of 5°C is never respected due to the high dependence of the greenhouse to the outside of it. $T_{e,measured}$ increases to about 25°C and decreases until about 20°C.

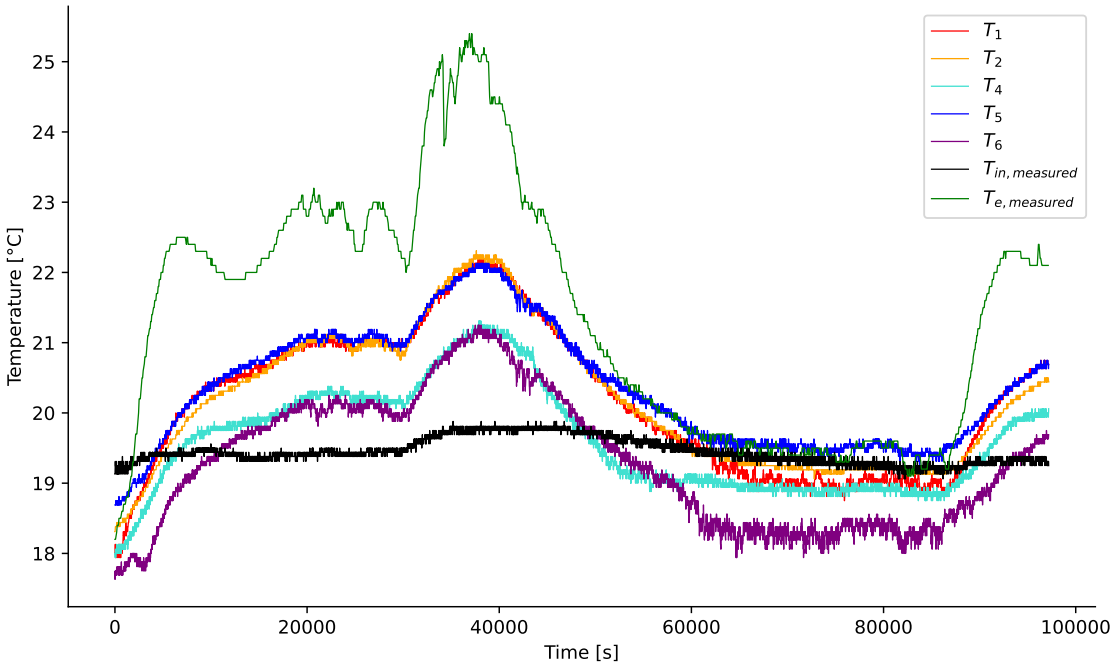

Figure 3.6: Temperatures measured by sensors between 6 a.m. on October 19, 2023 and 9 a.m. on October 20, 2023 when the greenhouse temperature is controlled

Experiment 2: Cold misted water

The second experiment focused on varying the temperature of the misting system, while keeping the greenhouse temperature nearly constant at around 22.5°C. The temperature of the misting system (measured by the sensor $s08$) was adjusted to a predetermined level. By controlling the misting temperature independently of the greenhouse temperature, the impact of it is being observed on the temperature of the chamber.
Between 11:16 a.m. and 1:56 p.m. on October 20, 2023, the misted water was cooled. This was done by adding crushed ice by doses of 1 liter but the re-increase of temperature was fast. Then, at 11:54 a.m., 20 liters of crushed ice was added to decrease at its lowest. The ice stock in the water was maintained to have a temperature of the misted water in the range of 3-5°C. This temperature measured by the sensor s08 can be seen on the Figure 3.7.

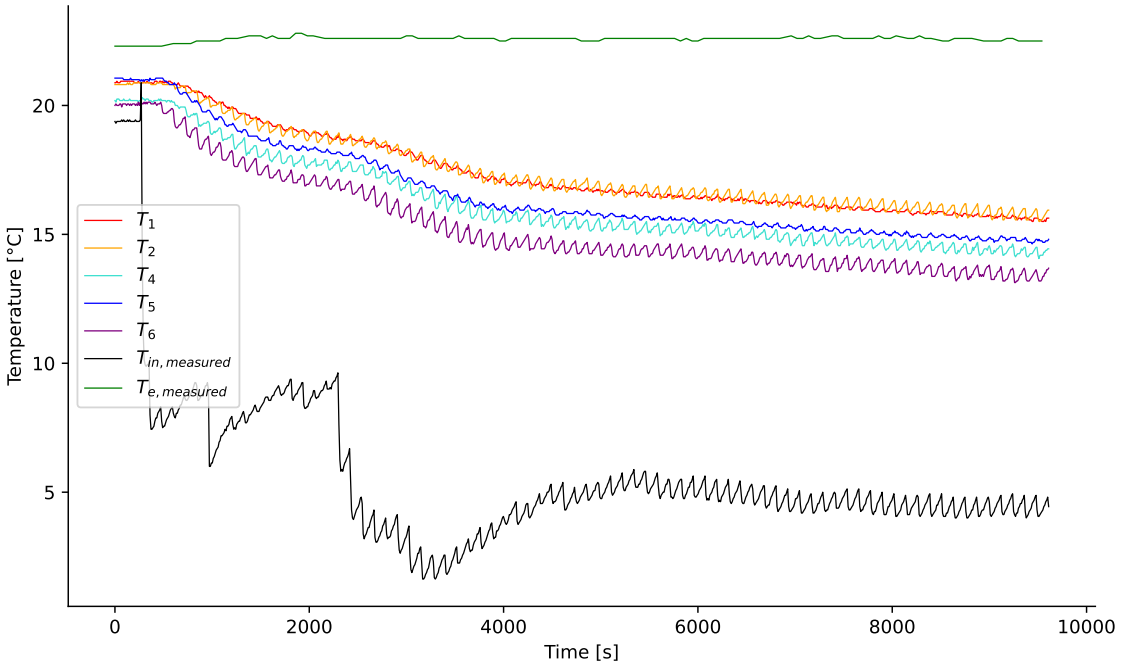

Figure 3.7: Temperatures measured by sensors between 11:16 a.m. and 1:56 p.m. on October 20, 2023 when the misted water is cold

Experiment 3: Hot misted water

Similar to the second experiment, the third experiment involved manipulating the temperature of the misting system within the chamber, while keeping the greenhouse temperature nearly constant at around 22.5°C. However, in this case, the misting temperature was set to a different level, representing an alternative misting condition. Between 2:23 p.m. and 5:16 p.m. on October 20, 2023, the misted water was heated. This temperature ($T_{in,measured}$) measured by the sensor s08 can be seen on the Figure 3.8.

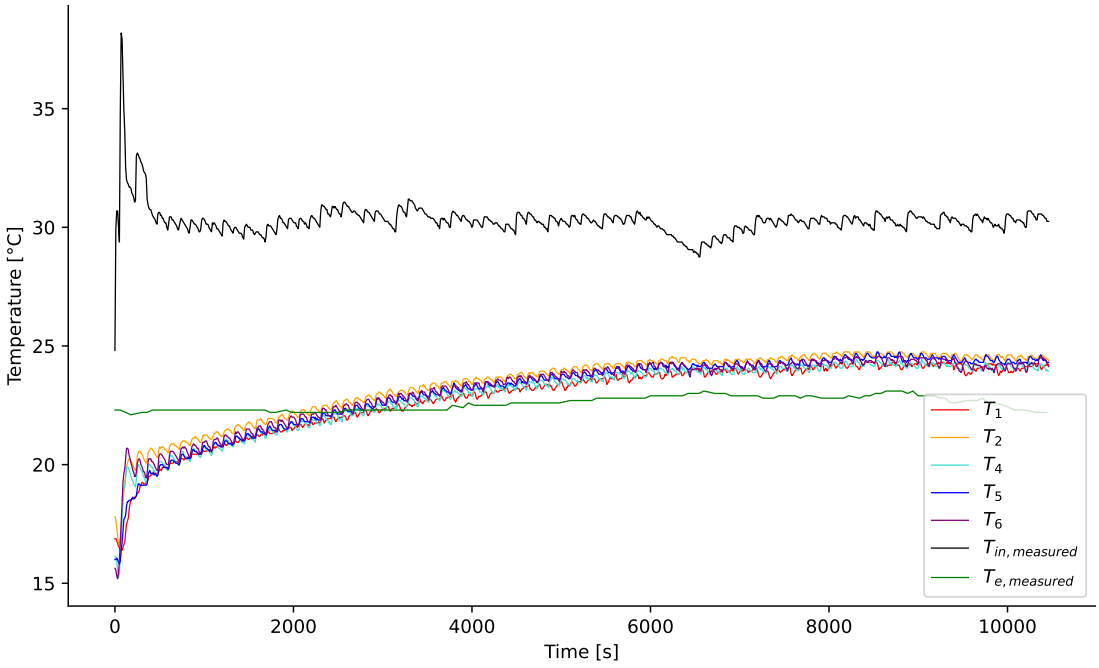

Figure 3.8: Temperatures measured by the sensors between 2:23 p.m. and 5:16 p.m. on October 20, 2023 when the misted water is hot

3.3.3 Verification of the sensors

The sensors were verified using reference data.
First, each sensor was immersed in a tray of ice cubes. A reference thermometer was used to measure the temperature next to the sensor. It was round 0°C.
Then, each sensor was immersed in a water bath round 30°C. The reference thermometer was used to measure the temperature next to the sensor.

The temperatures measured by the sensors during this verification are represented on Figure 3.9. The sensor s07 has not yet been introduced but will be used in Chapter 6.

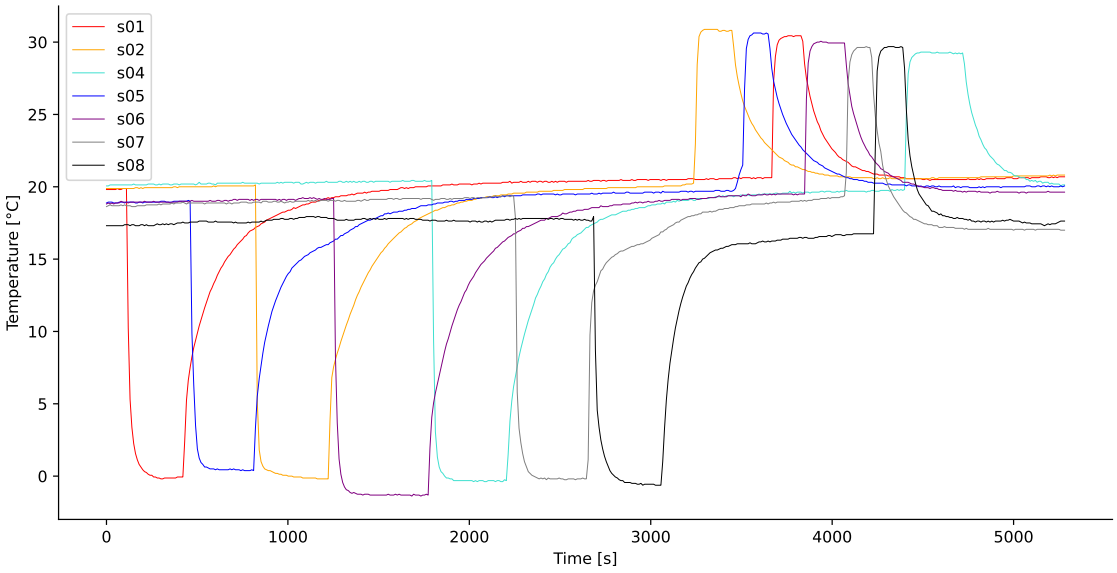

Figure 3.9: Temperatures measured by the sensors during verification

From this were obtained the error offsets of each sensor compared to the temperatures measured by the thermometer. The measurements and the error offsets ($T_{ref} - T_{s0i}$ with $i \in \{1, ..., 8\}$) can be seen in Table 3.1.

Sensor	Cold temperature			Hot temperature		
	T_{ref} [°C]	T_{s0i} [°C] $i \in \{1, ..., 8\}$	$T_{ref} - T_{s0i}$	T_{ref} [°C]	T_{s0i} [°C] $i \in \{1, ..., 8\}$	$T_{ref} - T_{s0i}$
s01	0	-0.06	0.06	30.6	30.44	0.16
s02	0.05	-0.19	0.24	31	30.81	0.19
s04	0	-0.31	0.31	30	29.25	0.75
s05	0.1	0.44	-0.34	30.8	30.56	0.24
s06	-0.1	-1.31	1.21	30.4	29.94	0.46
s07	0.1	-0.19	0.29	30.3	29.69	0.61
s08	0	-0.56	0.56	30.2	29.63	0.57

Table 3.1: Temperatures measured during the verification of the sensors and error offsets

The error offsets are quite small so they can be neglected and the data measured by the sensors can be considered correct.

Chapter 4

Modeling energy transfer in the experimental setup

4.1 Overview

In the previous chapter, the experimental setup was detailed and initial temperature measurements were conducted to establish a basic understanding of the thermal behavior within the system.

The primary objective of this chapter is to develop a dynamical model of energy transfer in the experimental set-up. With an accurate model, the temperature inside the chamber will be predictable in function of the temperatures inside the greenhouse and of the misted water.

Firstly, an overview on the heat transfer mechanisms is done to understand the typical functioning of heat exchange.
Then, the data collected during the three experiments, explained in Section 3.3.2, need to be preprocessed to be used during the further procedure.
Afterwards, the equation of the heat balance in the RootPhAir platform is established.
This equation contains unknowns and the values of them are being determined next. The identification of these parameters is done by analyzing the dynamic response of the system and by performing a linear regression.
Finally, the mass flow rate, that was considered unknown so far, is measured and the identification of the other unknown parameters is done by performing a linear regression again.

4.2 Theoretical background on heat transfer mechanisms

According to Incropera et al., "Heat transfer (or heat) is thermal energy in transit due to a spatial temperature difference." (p. 2) [17].

4.2.1 Modes of heat transfer

There are three primary modes of heat transfer: conduction, convection and radiation [7][17].

Conduction

There is conduction when heat is transferred through a material due to molecular collisions and diffusion. Via interactions between the particles within a substance, energy is transferred from particles with higher energy to those with lower energy. The physical mechanism of conduction can be illustrated by considering a gas with a temperature gradient, where no bulk motion exists. In this scenario, the gas occupies the space between two surfaces maintained at different temperatures. Temperature at any point is associated with the energy of gas molecules nearby, which includes their random translational, rotational and vibrational motions. Higher temperatures correspond to higher molecular energies. When neighboring molecules collide, energy is transferred from more energetic to less energetic molecules. In the presence of a temperature gradient, energy transfer by conduction occurs in the direction of decreasing temperature. Even in the absence of collisions, a net transfer of energy occurs due to the constant crossing of a hypothetical plane by molecules from above and below, resulting in a diffusion of energy.
This process is similar in liquids, where molecules are closely spaced, and in solids, where conduction is attributed to lattice vibrations induced by atomic motion. In electrical nonconductors, energy transfer occurs exclusively via lattice waves, while in conductors, it also involves the translational motion of free electrons [7][17].
The rate equation for conduction is the Fourier's law. For the one-dimensional plane wall shown in Figure 4.1, with a temperature distribution $T(x)$, the rate equation is expressed as follows [17]:

$$q''_x = -k\frac{dT}{dx}$$

where

- q''_x : heat transfer rate in the x-direction per unit area perpendicular to the direction of transfer $[\frac{W}{m^2}]$
- k : thermal conductivity $[\frac{W}{mK}]$

The heat rate by conduction q_x ($[W]$) through a plane wall of area A ($[m^2]$) is given by [17]:

$$q_x = q''_x A$$

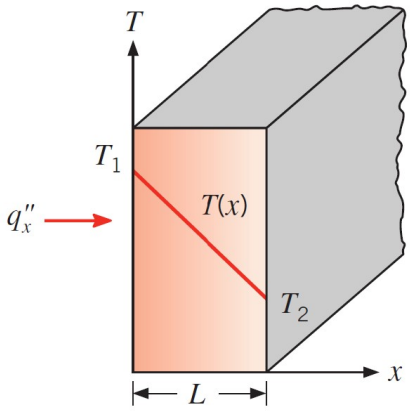

Figure 4.1: One-dimensional conductive heat transfer [17]

Convection

There is convection when heat is transferred through a fluid (liquid or gas) by the movement of fluid molecules. There are two possible mechanisms: energy transfer due to random molecular motion (diffusion) and energy transfer by the bulk motion of the fluid. This bulk motion occurs when large numbers of molecules move collectively or in aggregates. This contributes to heat transfer in the presence of a temperature gradient. The term "convection" refers to this cumulative transport, while "advection" specifically denotes transport due to bulk fluid motion.
In the context of fluid flow over a heated surface, a velocity boundary layer forms in the fluid, where the velocity varies from zero at the surface to a finite value associated with the flow. Additionally, a thermal boundary layer forms, where the temperature varies from the surface temperature to the temperature of the outer flow. Convection heat transfer occurs from the surface to the outer flow within these boundary layers.
Convection heat transfer is sustained by both random molecular motion and bulk fluid motion within the boundary layer. Near the surface, where fluid velocity is low, diffusion dominates, while bulk fluid motion becomes more significant as the boundary layer grows downstream.
Convection heat transfer can be classified based on the nature of the flow: forced convection, induced by external means like fans or pumps, and free (or natural) convection, induced by buoyancy forces due to temperature variations in the fluid. Mixed convection may also occur when conditions lead to a combination of forced and natural convection.

Convection heat transfer primarily involves the transfer of sensible (internal thermal) energy of the fluid. However, latent heat exchange may also occur in some processes, particularly those involving phase changes between liquid and vapor states [7][17]. The rate equation for convection is the Newton's law of cooling [7][17]:

$$q'' = h(T_s - T_\infty)$$

where

- q'': convective heat flux $\left[\frac{W}{m^2}\right]$
- h: convection heat transfer coefficient $\left[\frac{W}{m^2 K}\right]$
- T_s: surface temperature $[K]$
- T_∞: fluid temperature $[K]$

Radiation

There is thermal radiation when heat is transferred through space or a medium by electromagnetic waves without the need for direct contact. Thermal radiation is emitted by matter at a nonzero temperature, including solid surfaces, liquids and gases. This emission results from changes in the electron configurations of atoms or molecules and is transported by electromagnetic waves or photons. Unlike conduction or convection, radiation transfer does not require a material medium and is most efficient in a vacuum [7][17].
The rate at which energy is released per unit area from a surface, termed surface emissive power E ($\left[\frac{W}{m^2}\right]$), follows the Stefan–Boltzmann law, with an upper limit determined by [7][17]:

$$E_b = \sigma T_s^4$$

where

- E_b: upper limit of emissive power $\left[\frac{W}{m^2}\right]$
- T_s: absolute temperature of the surface $[K]$
- $\sigma = 5.67 \cdot 10^{-8} \frac{W}{m^2 K^4}$: Stefan Boltzmann constant

A surface that reaches this upper limit is called an ideal radiator or blackbody. However, real surfaces emit less heat flux than blackbodies due to their radiative

property called emissivity ϵ, which measures their efficiency relative to a blackbody [7][17].

$$E = \epsilon E_b$$

Absorptivity α, another surface radiative property, determines the rate at which radiant energy is absorbed per unit surface area [7][17]:

$$G_{abs} = \alpha G$$

where

- G_{abs}: absorbed radiation $\left[\frac{W}{m^2}\right]$

Radiation may also be incident on a surface from its surroundings, such as sunlight or nearby surfaces. The rate at which this radiation is incident on a unit area of the surface is termed irradiation G ($\left[\frac{W}{m^2}\right]$). A portion or all of this irradiation may be absorbed by the surface, increasing its thermal energy. Absorbed and emitted radiation affect the thermal energy of matter, while reflected and transmitted radiation do not [7][17].

4.3 Data preprocessing

4.3.1 Approximation of the temperature inside the chamber

On the Figures 4.2, 4.3 and 4.4, for each experiment, the mean value of the temperatures measured by the five sensors inside the chamber is represented.

$$T_{mean} = \frac{T_1 + T_2 + T_4 + T_5 + T_6}{5} \tag{4.1}$$

with:

- T_{mean} the mean value of the temperatures measured by the five sensors inside the chamber
- T_1 the temperature measured by the sensor s01
- T_2 the temperature measured by the sensor s02
- T_4 the temperature measured by the sensor s04
- T_5 the temperature measured by the sensor s05
- T_6 the temperature measured by the sensor s06

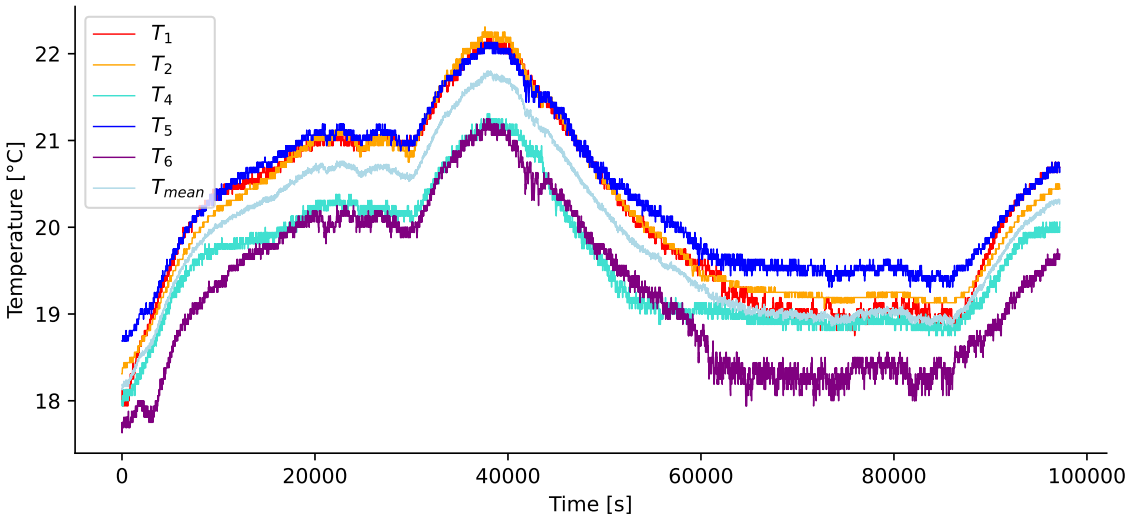

Figure 4.2: Temperatures measured by the five sensors inside the chamber and the mean value of them during experiment 1

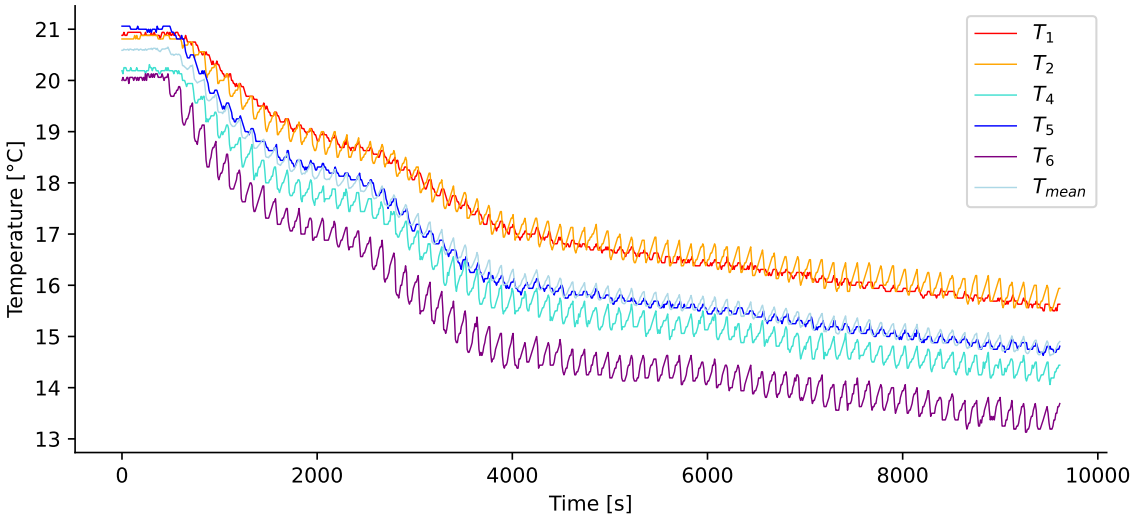

Figure 4.3: Temperatures measured by the five sensors inside the chamber and the mean value of them during experiment 2

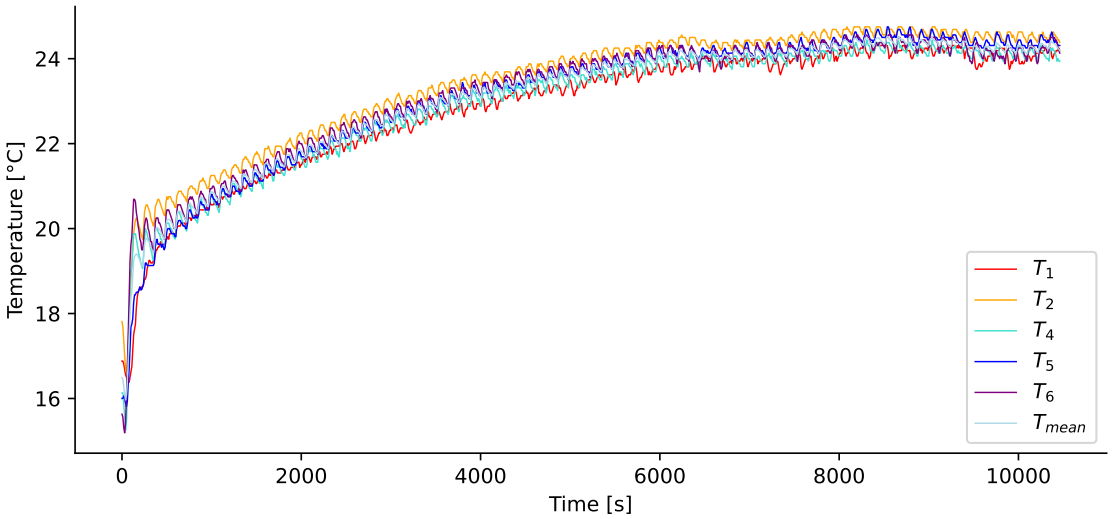

Figure 4.4: Temperatures measured by the five sensors inside the chamber and the mean value of them during experiment 3

In view of Figures 4.2, 4.3 and 4.4, the mean value of the temperatures is a good approximation of the temperature inside the chamber. The temperature can be assumed homogeneous in the chamber and the further computations are made on the mean temperature.

4.3.2 Sampling

A first step in data preprocessing is sampling it. The measurements were done on irregular intervals, but it needs to have a steady step to use it. In fact, concerning the sensors, the measurements seemed to be done every 10 seconds but irregularities in measuring have led to some steps being 11 seconds. Concerning the temperature of the greenhouse measured by the probe of the "ARIA" supervision system, it also needs to be sampled to respect the same time steps. The data is up-sampled to have a step of 1 second between each value. A linear interpolation is done to determine the missing values [26].
Basically, a linear interpolation is given by [36]:

$$y = y_0 + (x - x_0)\frac{y_1 - y_0}{x_1 - x_0}$$

for values x and y in the intervals (x_0, x_1) and (y_0, y_1) respectively, as can be seen on Figure 4.5. (x_0, y_0) and (x_1, y_1) are the two red points that are known. The

value of y is found for a certain x along the straight blue line between the two known points. This line is called the interpolant. The equation of the slope is [36]:

$$\frac{y - y_0}{x - x_0} = \frac{y_1 - y_0}{x_1 - x_0}$$

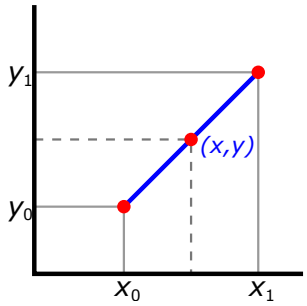

Figure 4.5: Linear interpolation [36]

The sampled values of the temperature of the greenhouse, of the temperature of the misting and of the mean of the temperatures inside the chamber are seen on Figures 4.6, 4.7 and 4.8.

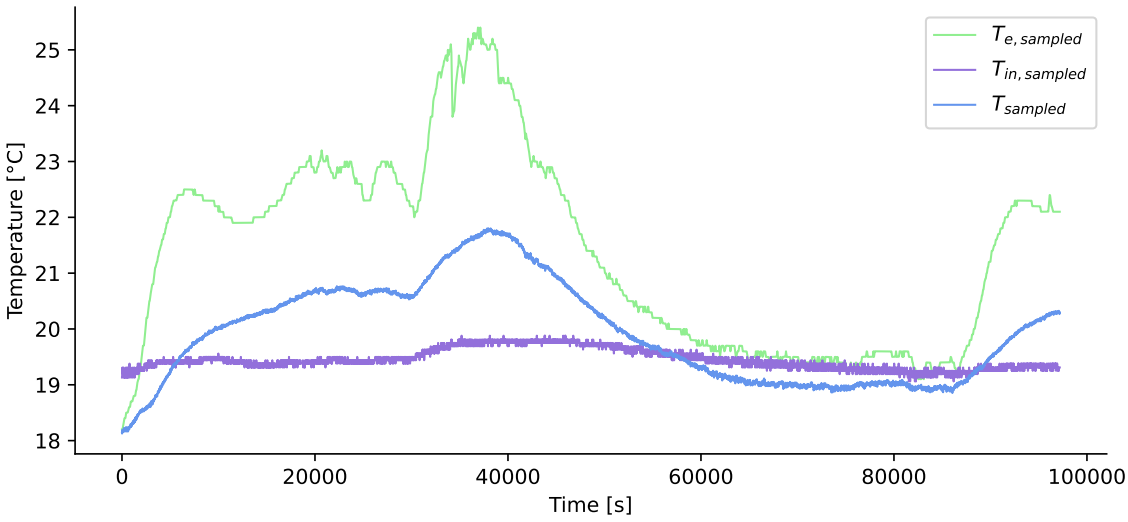

Figure 4.6: Sampled temperatures during experiment 1

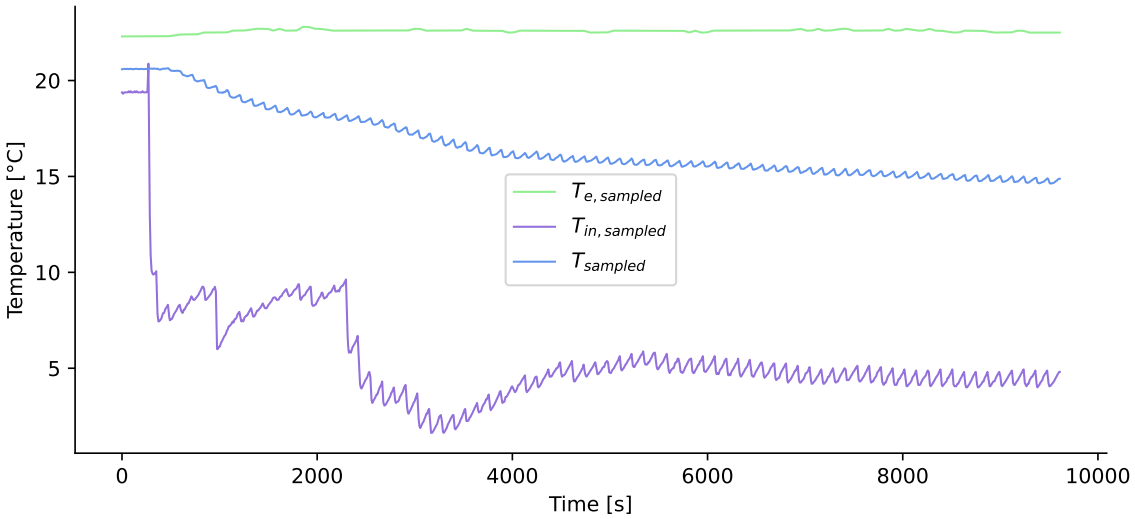

Figure 4.7: Sampled temperatures during experiment 2

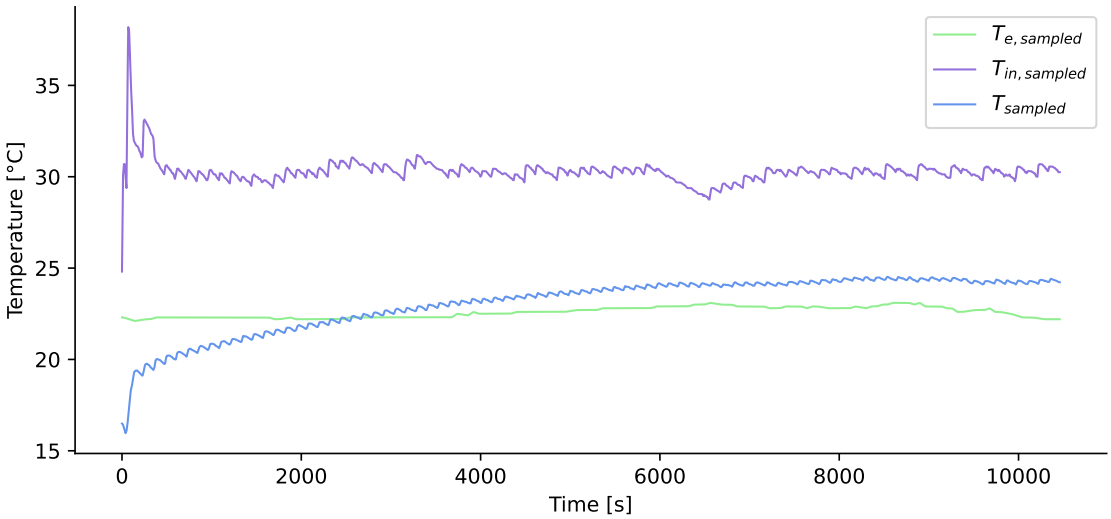

Figure 4.8: Sampled temperatures during experiment 3

4.3.3 Filtering

It can be seen, on the Figures 4.6, 4.7 and 4.8, that the signal of temperature contains noise. A solution to avoid this is to filter the signal before using it. In

this case, a low-pass filter is used. Its goal is to allow the transmission of signals with lower frequencies while inhibiting signals with higher frequencies.
The intended range of low frequencies is termed the passband or bandwidth of the filter, while the range of higher frequencies is known as the stopband.
The frequency at which the passband transitions into the stopband is denoted as the cutoff frequency. It determines the frequency below which the signal will pass with minimal attenuation and above which it will be attenuated [16][34].
For the first experiment, the cutoff frequency is:

$$f_{c,1} = 0.000333\ Hz$$

For the second and third experiments, the cutoff frequency is:

$$f_{c,2;3} = 0.004\ Hz$$

The filter order determines the steepness of the roll-off beyond the cutoff frequency. Higher filter orders provide sharper roll-off characteristics but may introduce more phase distortion and require more computational resources. Lower filter orders offer smoother frequency response but may not adequately suppress high-frequency noise [34].

In this case, a low-pass filter of first order is designed using the Butterworth method. Butterworth filters are one of the most used low-pass filters. [28].

When designing the Butterworth filter, the cutoff frequency must be normalized to the Nyquist frequency which is half the sampling frequency:

$$F_N = \frac{f_s}{2}$$

There is 1 measurement every second. The sampling frequency is then:

$$f_s = 1\ Hz$$

The Nyquist sampling rate, or frequency, is the minimum rate required to sample a finite bandwidth signal in order to preserve all of its information [18].

The designed low-pass filter is applied to the original signal, effectively attenuating frequencies above the cutoff frequency while preserving those below it.
An inverse Fourier transform is applied to the filtered signal to convert it back to the time domain. This yields the final filtered signal. This can be seen on Figures 4.9, 4.10 and 4.11.

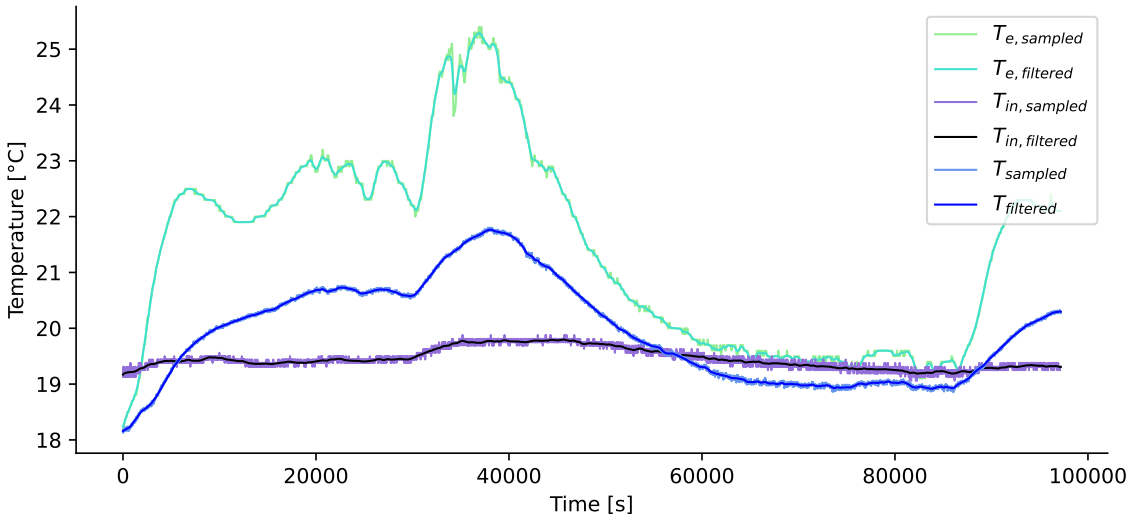

Figure 4.9: Filtering of the temperatures of the experiment 1

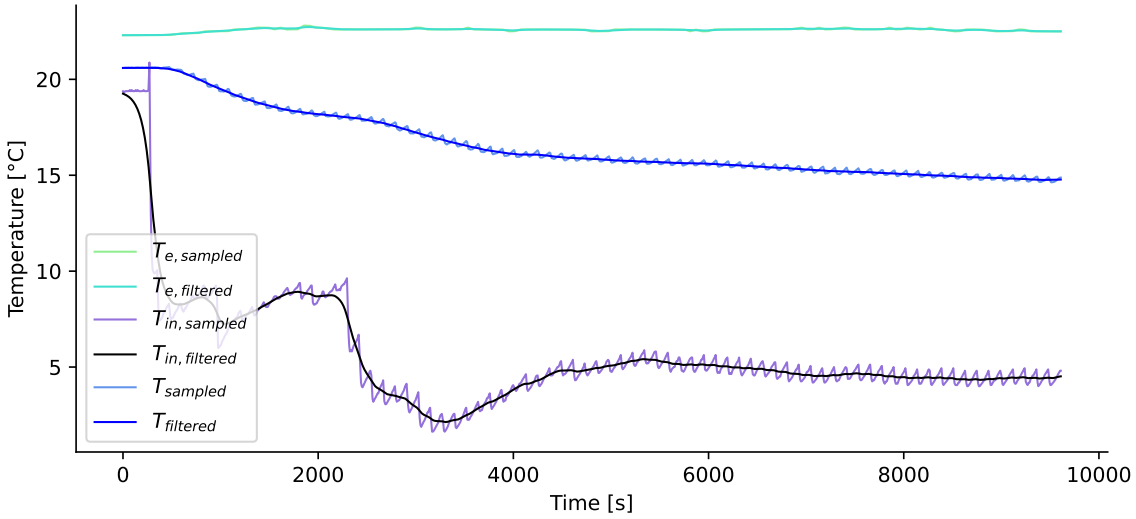

Figure 4.10: Filtering of the temperatures of the experiment 2

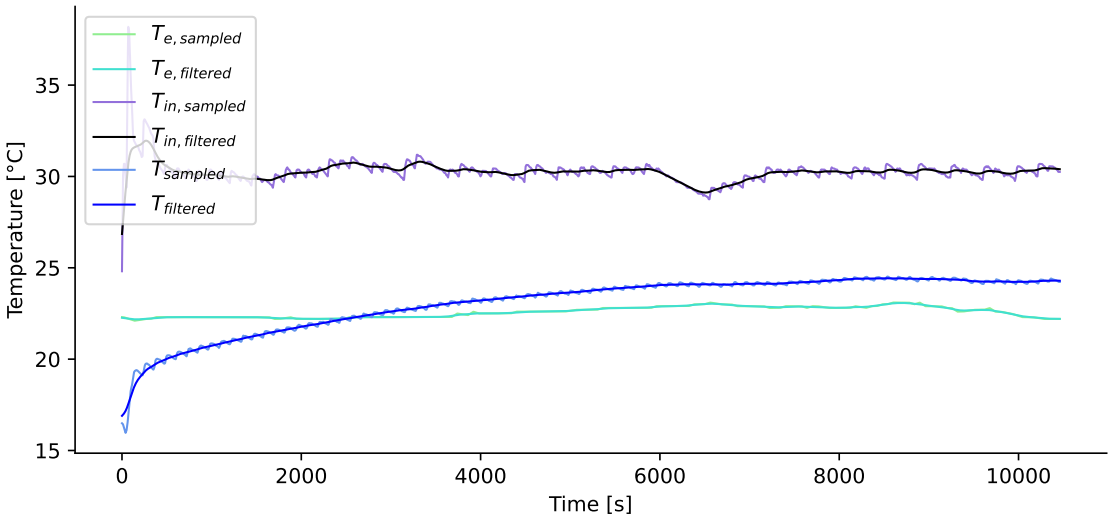

Figure 4.11: Filtering of the temperatures of the experiment 3

Now that the data is effectively preprocessed, the rest of the computations in this chapter are made on the filtered sampled temperatures. When talking about $T_{measured}$, $T_{in,measured}$ and $T_{e,measured}$, it signified that it is about the data measured that have been passed through the preprocessing of sampling and filtering.

4.4 Heat balance equation

The equation of heat balance in the chamber is the following:

$$\rho_w c_{p,w} V \dot{T} = \dot{m} c_{p,w} (T_{in} - \beta T) + \alpha (T_e - T) \tag{4.2}$$

The parameters are:

- $\rho_w = 1000 \frac{kg}{m^3}$ is the density of water.
- $c_{p,w} = 4.185 \frac{kJ}{kgK}$ is the mass heat capacity of liquid water at 20°C.
- $V = 5200mm \cdot \frac{1148}{2} mm \cdot 1573mm = 4.6951m^3$ is the active volume which is the upper half of the chamber where the roots are located. It is derived from the measurements of the chamber that can be found in the Appendix A.

The unknown parameters are:

- β [-] is the factor of exchange between T_{in} and T, with $0 \leq \beta \leq 1$.

- $\dot{m}\left[\frac{kg}{s}\right]$ is the mass flow of the misted water.
- $\alpha\left[\frac{kJ}{sK}\right]$ is the thermal conductance.

The variables are:

- T_{in} is the temperature of the misting.
- T_e is the temperature of the greenhouse.
- T is the temperature inside the chamber.
- $\dot{T}$ is the time derivative of T.

4.5 Model testing

To determine with which parameters the model (4.2) simulates the best the reality that happens in the chamber, the model is tested on the temperatures measured during the three experiments (described in Section 3.3.2).

Concerning experiment 1, the temperature T_{in} is approximated to be constant at a value of 19.5°C. The simulation of T is done by applying the model with the approximation of T_{in} and the measurement of T_e.

Concerning experiment 2, it is split in experiment 2a and 2b because T_{in} is cooled in two steps as can be seen on Figure 4.12. The separation in 2a and 2b is represented by the red line. The temperature T_{in} is approximated by a step function:

$$T_{in,exp2a} = \begin{cases} 19 & \text{if } 0 \leq t < 314\ s \\ 8 & \text{if } 314\ s \leq t \end{cases}$$

$$T_{in,exp2b} = \begin{cases} 8 & \text{if } 0 \leq t < 992\ s \\ 4 & \text{if } 992\ s \leq t \end{cases}$$

The temperature T_e is approximated to be constant at a value of 22.5°C. The simulation of T is found by applying the model with the approximations of T_{in} and T_e.

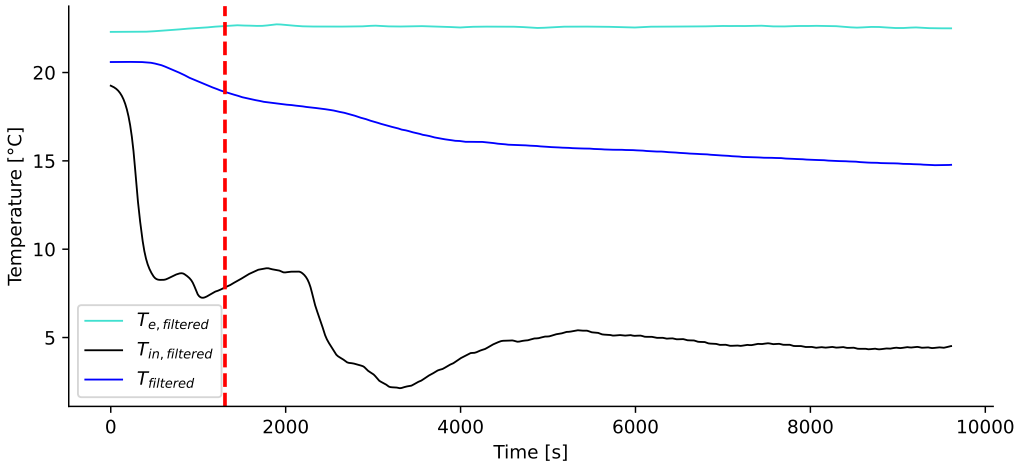

Figure 4.12: Split of experiment 2 in experiments 2a and 2b

Concerning experiment 3, T_{in} is heated in a step as can be seen on Figure 4.13. The temperature T_{in} is also approximated by a step function:

$$T_{in,exp3} = \begin{cases} 24.8 & \text{if } 0 \leq t < 10\ s \\ 30 & \text{if } 10\ s \leq t \end{cases}$$

The temperature T_e is approximated to be constant at a value of 22.5°C. The simulation of T is found by applying the model with the approximations of T_{in} and T_e.

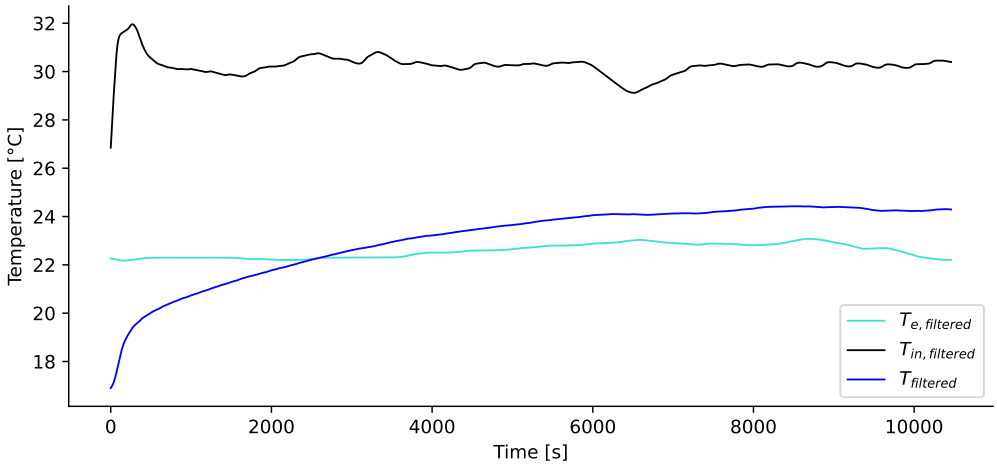

Figure 4.13: Experiment 3 that has been preprocessed

4.6 Dynamic process modeling

A method to determine two unknown parameters, in this case $\dot{m}$ and α, is analyzing the system's dynamic response, especially the step response.
The parameter β is varied during the tests to find the best value between 0 and 1.

4.6.1 Transfer functions

Firstly, the expressions of the time constant τ and gains K_{in} and K_e need to be formulated to deduce α and $\dot{m}$ from it. In order to achieve this, the differential equation (4.2) is expressed through transfer functions. Both representations are equivalent representations for linear models [11].
In (4.2), the temporal derivative term $\frac{d}{dt}$ is replaced by a variable denoted as "s":

$$\begin{aligned}
\rho_w c_{p,w} V sT &= \dot{m} c_{p,w}(T_{in} - \beta T) + \alpha(T_e - T) \\
sT &= \frac{\dot{m} c_{p,w}}{\rho_w c_{p,w} V}(T_{in} - \beta T) + \frac{\alpha}{\rho_w c_{p,w} V}(T_e - T) \\
\left(s + \frac{\dot{m} c_{p,w}\beta}{\rho_w c_{p,w} V} + \frac{\alpha}{\rho_w c_{p,w} V}\right) T &= \frac{\dot{m} c_{p,w}}{\rho_w c_{p,w} V} T_{in} + \frac{\alpha}{\rho_w c_{p,w} V} T_e
\end{aligned}$$

$$\begin{aligned}
T(t) &= \frac{\frac{\dot{m} c_{p,w}}{\rho_w c_{p,w} V}}{s + \frac{\dot{m} c_{p,w}\beta + \alpha}{\rho_w c_{p,w} V}} T_{in}(t) + \frac{\frac{\alpha}{\rho_w c_{p,w} V}}{s + \frac{\dot{m} c_{p,w}\beta + \alpha}{\rho_w c_{p,w} V}} T_e(t) \\
&= \frac{\dot{m} c_{p,w}}{s\rho_w c_{p,w} V + \dot{m} c_{p,w}\beta + \alpha} T_{in}(t) + \frac{\alpha}{s\rho_w c_{p,w} V + \dot{m} c_{p,w}\beta + \alpha} T_e(t) \\
&= \frac{\frac{\dot{m} c_{p,w}}{\dot{m} c_{p,w}\beta + \alpha}}{s\frac{\rho_w c_{p,w} V}{\dot{m} c_{p,w}\beta + \alpha} + 1} T_{in}(t) + \frac{\frac{\alpha}{\dot{m} c_{p,w}\beta + \alpha}}{s\frac{\rho_w c_{p,w} V}{\dot{m} c_{p,w}\beta + \alpha} + 1} T_e(t) \\
&= H_1(s) T_{in}(t) + H_2(s) T_e(t)
\end{aligned}$$

The transfer functions, respectively between T and T_{in}, and between T and T_e can be rewritten as [11]:

$$\begin{aligned}
H_1(s) &= \frac{K_{in}}{s\tau + 1} \\
H_2(s) &= \frac{K_e}{s\tau + 1}
\end{aligned} \tag{4.3}$$

The gain K_{in} between T and T_{in}, the gain K_e between T and T_e and the time

constant τ are deduced:

$$K_{in} = \frac{\dot{m}c_{p,w}}{\dot{m}c_{p,w}\beta + \alpha} \tag{4.4}$$

$$K_e = \frac{\alpha}{\dot{m}c_{p,w}\beta + \alpha}$$

$$\tau = \frac{\rho_w c_{p,w} V}{\dot{m}c_{p,w}\beta + \alpha} \tag{4.5}$$

4.6.2 Dynamic response of the system

Step responses are the responses to a step input signal. In other words, the form taken by the output variable $T(t)$ is considered when applying a step input signal $T_{in}(t)$ to the dynamic system [11].
This configuration is what was done during experiments 2 and 3 (explained in Section 3.3.2). T_e is constant and the response of T is observed when applying a step input of T_{in}. This method is thus applied on the temperatures measured during these two experiments.

In what follows, the system is assumed to be stable (or at the stability limit) and to be initially at equilibrium. It permits to focus specifically on studying the system's response to a step input independently of the effect of initial conditions [11].

Isolating the time derivative in the heat balance equation (4.2) gives:

$$\frac{dT}{dt} = \frac{\dot{m}c_{p,w}}{\rho_w c_{p,w} V}(T_{in}(t) - \beta T(t)) + \frac{\alpha}{\rho_w c_{p,w} V}(T_e(t) - T(t))$$

In the experiments 2 and 3, the variation of T_e is neglected:

$$\frac{dT}{dt} = \frac{\dot{m}c_{p,w}}{\rho_w c_{p,w} V} T_{in}(t) - \left(\frac{\dot{m}c_{p,w}\beta}{\rho_w c_{p,w} V} + \frac{\alpha}{\rho_w c_{p,w} V}\right) T(t)$$

Two parameters uniquely characterize the dynamic response of the system: the magnitude of the variation in the output variable $T(t)$ and the response time.

The magnitude of the variation is given by the final value of $T(t)$ which is:

$$K_{in}\Delta T_{in} + K_e \Delta T_e = \frac{\dot{m}c_{p,w}}{\dot{m}c_{p,w}\beta + \alpha}\Delta T_{in} + \frac{\alpha}{\dot{m}c_{p,w}\beta + \alpha}\Delta T_e$$

As said before, the variation of T_e is neglected so $\Delta T_e = 0$. The magnitude of the variation is then:

$$K_{in}\Delta T_{in} = \frac{\dot{m}c_{p,w}}{\dot{m}c_{p,w}\beta + \alpha}\Delta T_{in}$$

The response time τ_r is defined as the time to reach 95% of the final response.

From the value of $K_{in}\Delta T_{in}$, K_{in} is deduced knowing the value of ΔT_{in}.
From the value of τ_r, τ is determined using:

$$\tau_r = 3\tau$$

Finally, from K_{in} and τ, the values of α and $\dot{m}$ are determined using (4.4) and (4.5).

Application

The step responses during experiments 2a, 2b and 3 are represented on Figures 4.14, 4.15 and 4.16. The magnitude of the variation of T when applying a ΔT_{in}, the 95% of it and the response time are indicated on it.

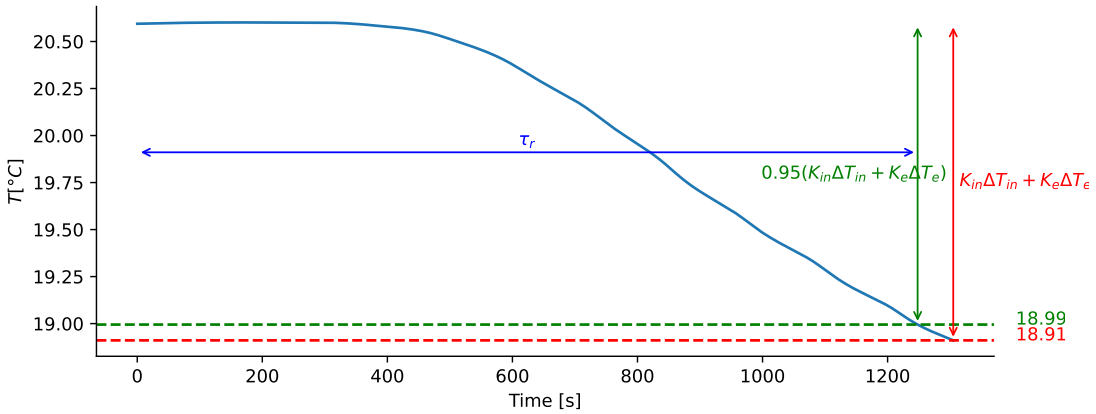

Figure 4.14: Step response of experiment 2a

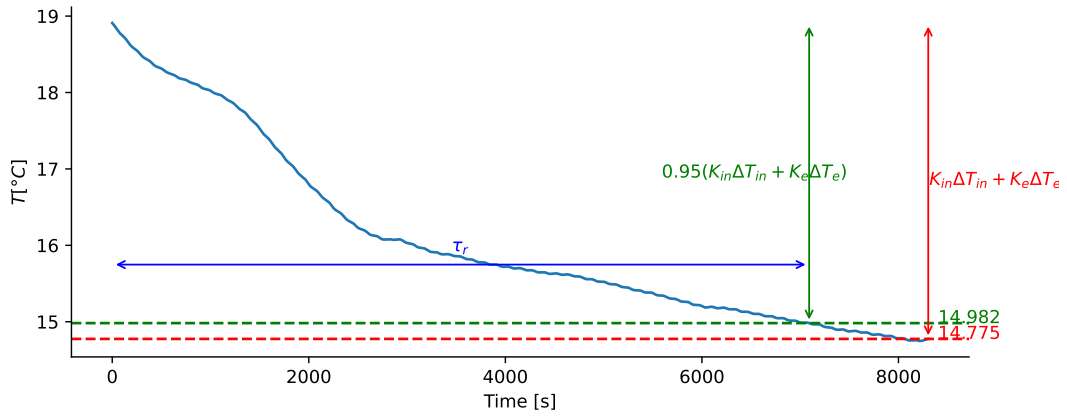

Figure 4.15: Step response of experiment 2b

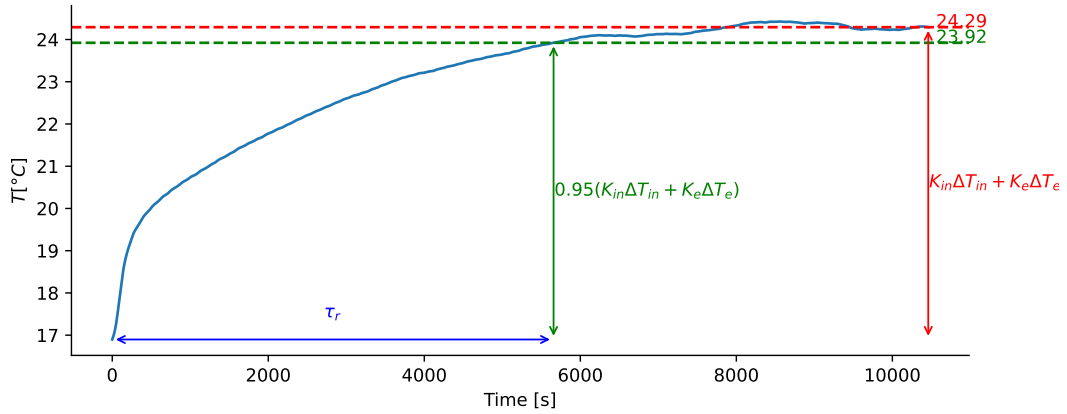

Figure 4.16: Step response of experiment 3

The intermediate values for the computations of α and $\dot{m}$ explained before are found from these Figures 4.14, 4.15 and 4.16 and listed in Table 4.1.

	Experiment 2a	Experiment 2b	Experiment 3
ΔT_{in} $[°C]$	-11.411	-3.331	3.545
ΔT_e $[°C]$	0	0	0
$K_{in}\Delta T_{in} + K_e\Delta T_e$ $[°C]$	-1.684	-4.134	7.025
K_{in} $[-]$	0.148	1.241	2.086
$0.95(K_{in}\Delta T_{in} + K_e\Delta T_e)$ $[°C]$	-1.6	-3.927	7.025
τ_r $[s]$	1248	7091	5657
τ $[s]$	416	2363.667	1885.667

Table 4.1: Intermediate values for the determination of α and $\dot{m}$ for each step response of experiments 2a, 2b and 3

From the curve on Figure 4.14, the 2a part can be eliminated because there is no plateau. So it is better to keep only the step responses of experiments 2b and 3. In fact, the values (see Table 4.1) are not too far apart, whereas there are big differences between 2a and 2b-3.

Then, the equations (4.4) and (4.5) are applied with different values of β between 0 and 1. The procedure to test the parameters (explained in Section 4.5) is applied with the different values of β and the values of α and $\dot{m}$ associated. The results obtained for some values of β are reported in Appendix B. Two relevant values of β are retained: 0.47 and 1.

The best fitting of the real temperature is obtained with $\beta = 1$. The values of α and $\dot{m}$ found for the step responses of experiments 2b and 3 are reported in Table 4.2. The problem with this determination is that $\alpha_{exp2b} < 0$ and $\alpha_{exp3} < 0$, which is not possible.

	Experiment 2b	Experiment 3
α $\left[\frac{kJ}{sK}\right]$	-2.004	-11.314
$\dot{m}$ $\left[\frac{kg}{s}\right]$	2.465	5.194

Table 4.2: Values of α and $\dot{m}$ from the step responses of experiments 2b and 3 with $\beta = 1$

The higher the value of β, the best the fitting so the objective was to find the highest value of β that gives positive α_{exp2b} and α_{exp3}. This value is $\beta = 0.47$. The values of α and $\dot{m}$ for each experiment are reported in Table 4.3. It is observed that the values of the mass flow rate are the same regardless of the value of β. However, it changes from one experiment to another.

	Experiment 2b	Experiment 3
α $\left[\frac{kJ}{sK}\right]$	3.464	0.204
$\dot{m}$ $\left[\frac{kg}{s}\right]$	2.465	5.194

Table 4.3: Values of α and $\dot{m}$ from the step responses of experiments 2b and 3 with $\beta = 0.47$

An estimation of the parameters α and $\dot{m}$ could be their mean values:

$$\begin{aligned} \alpha_{mean} &= \frac{\alpha_{exp2b} + \alpha_{exp3}}{2} \\ &= 1.834 \ \frac{kJ}{sK} \\ \dot{m}_{mean} &= \frac{\dot{m}_{exp2b} + \dot{m}_{exp3}}{2} \\ &= 3.83 \ \frac{kg}{s} \end{aligned} \tag{4.6}$$

The different sets of parameters (of experiment 2b, experiment 3 and the mean) are tested (see Section 3.3.2) to see which one represents most likely the reality.
The simulations using α_{exp2b} and $\dot{m}_{exp2b}$ are on Figure 4.17.
The simulations using α_{exp3} and $\dot{m}_{exp3}$ are on Figure 4.18.
The simulations using α_{mean} and $\dot{m}_{mean}$ are on Figure 4.19.

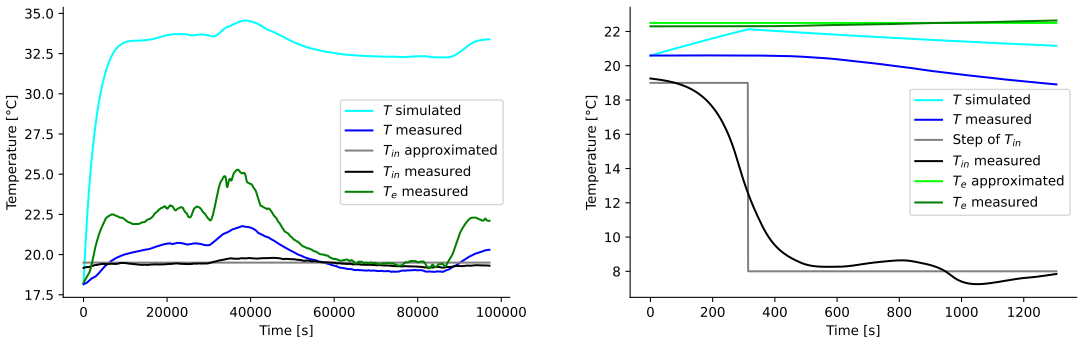

(a) (b)

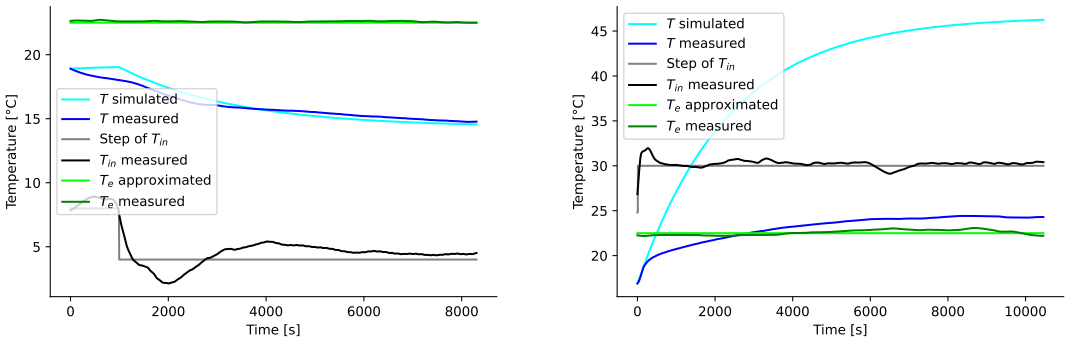

(c) (d)

Figure 4.17: Simulation of T during experiments (a) 1, (b) 2a, (c) 2b and (d) 3, using α_{exp2b} and $\dot{m}_{exp2b}$ from the step response of experiment 2b with $\beta = 0.47$

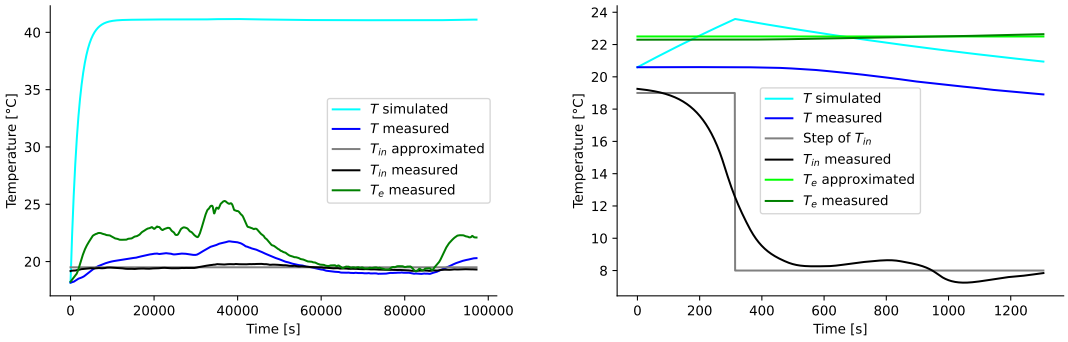

(a) (b)

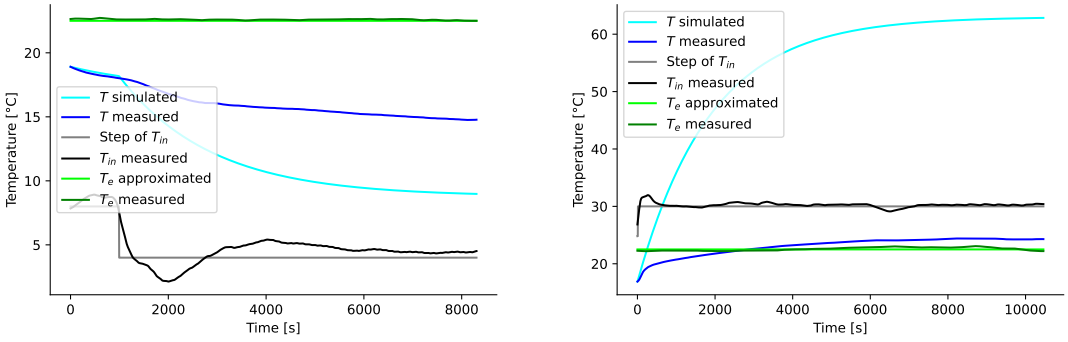

(c) (d)

Figure 4.18: Simulation of T during experiments (a) 1, (b) 2a, (c) 2b and (d) 3, using α_{exp3} and $\dot{m}_{exp3}$ from the step response of experiment 3 with $\beta = 0.47$

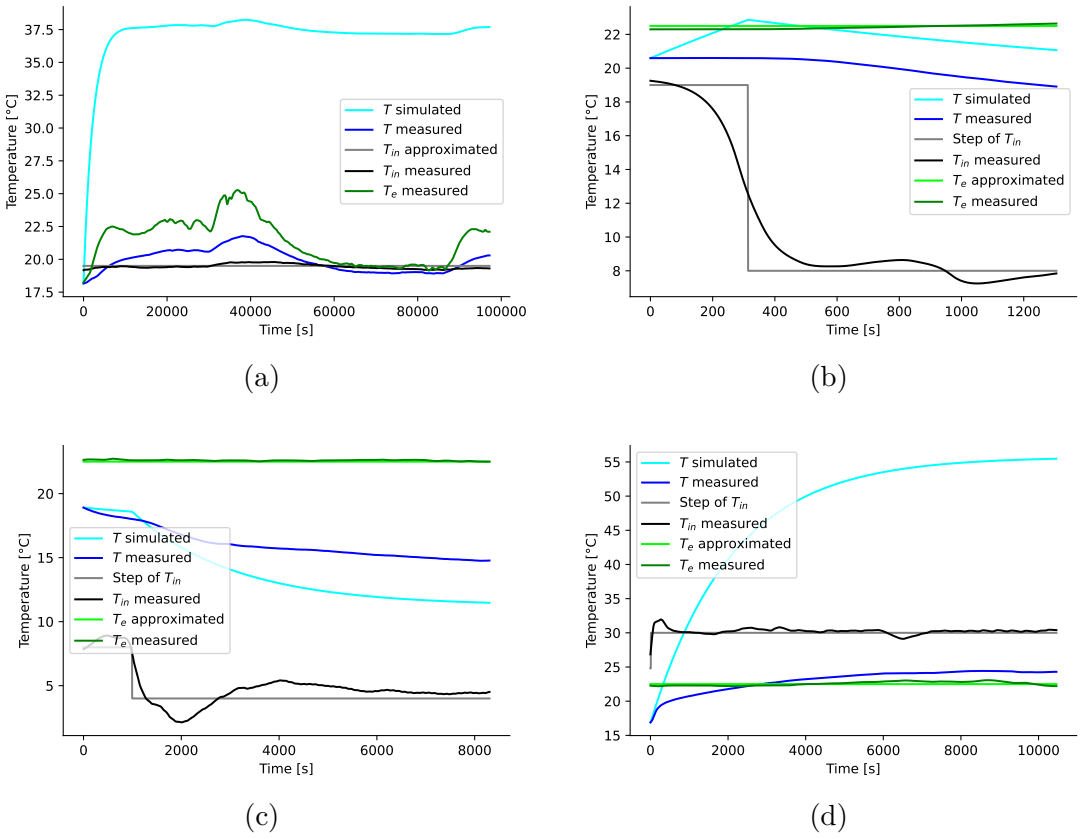

Figure 4.19: Simulation of T during experiments (a) 1, (b) 2a, (c) 2b and (d) 3, using α_{mean} and $\dot{m}_{mean}$ from the step responses with $\beta = 0.47$

No set of parameters give adequate results. Therefore, another method is used to determine the unknown parameters: linear regression.

4.7 Linear regression

This method is used to determine the value of one parameter, α.
As was observed in Section 4.6.2, the values of the mass flow rate determined with the method of step response's analysis are the same for each experiment (2a, 2b and 3) regardless of the value of β. For this reason, it is admitted that the mean value (see (4.6)), can be taken to be the value of $\dot{m}$ for the model determined by linear regression:

$$\dot{m} = 3.83 \frac{kg}{s}$$

The parameter β is varied during the tests to find the best value between 0 and 1.

4.7.1 Time derivative of temperature

To use this method, the values of the variables in the equation (4.2) are the temperatures measured during experiments 1, 2 and 3 (Section 3.3.2). The time derivative of the temperature of the chamber $\dot{T}$ has to be computed from the measurements of the temperature of the chamber T.
$\dot{T}$ can be calculated using the explicit Euler method:

$$\dot{T}_n = \frac{T_{n+1} - T_n}{t_{n+1} - t_n}$$

with T_n being the temperature at time t_n and T_{n+1} the temperature at time t_{n+1} [35].

Such as the temperature signals, the derivatives of the filtered mean of the temperatures inside the chamber contain some noise. They need to be filtered as well. A low pass filter as in Section 4.3.3 is used. The derivatives and their filtering for each experiment can be seen on Figures 4.20, 4.21 and 4.22.

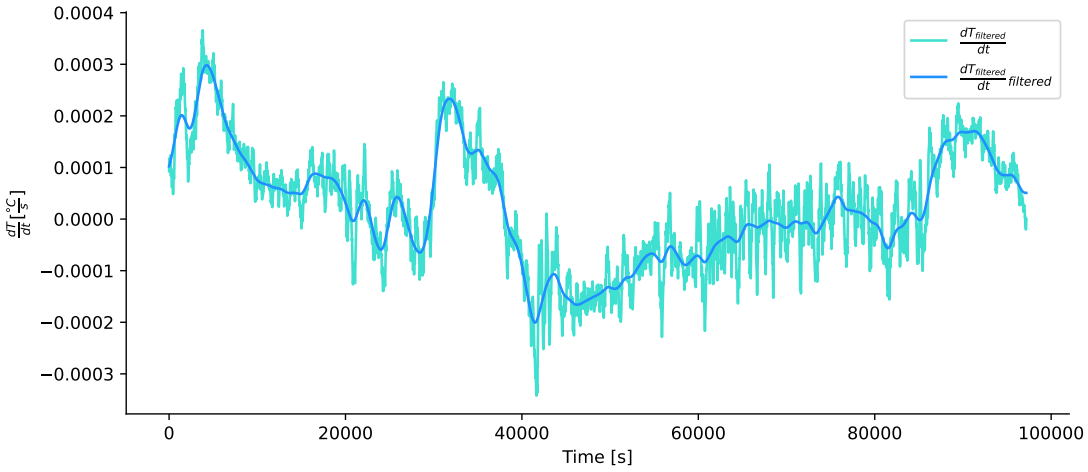

Figure 4.20: Filtered temporal derivative of the filtered mean of the temperatures inside the chamber during experiment 1

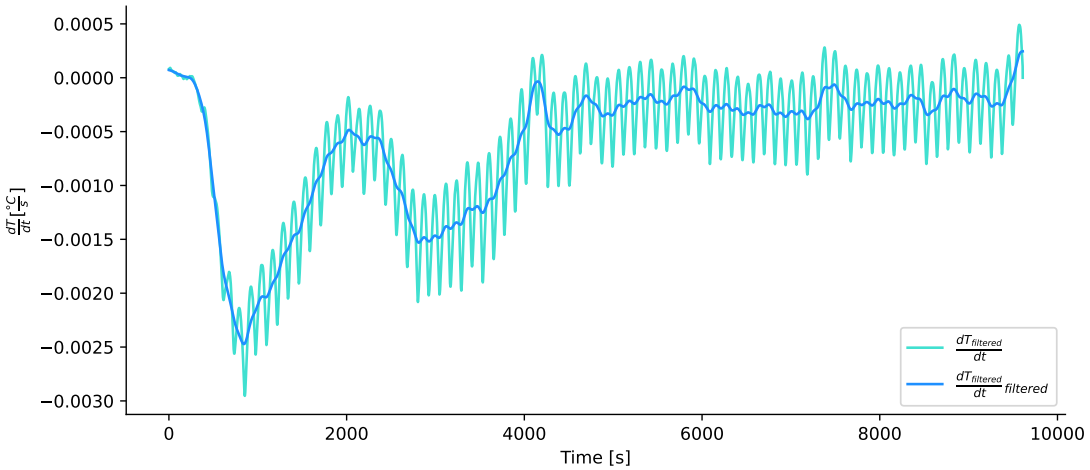

Figure 4.21: Filtered temporal derivative of the filtered mean of the temperatures inside the chamber during experiment 2

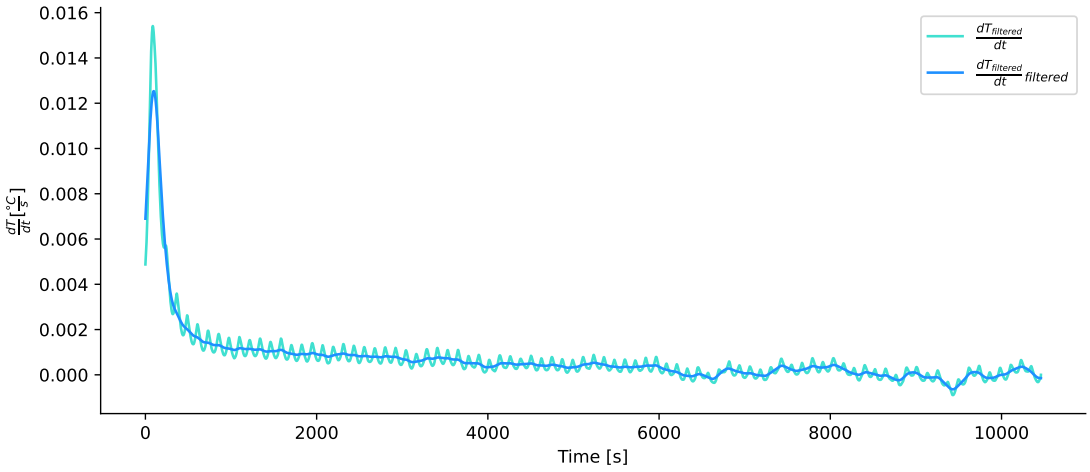

Figure 4.22: Filtered temporal derivative of the filtered mean of the temperatures inside the chamber during experiment 3

Calculating $\dot{T}$ when the signal of T is not filtered can be seen in Appendix C.

4.7.2 Simple linear regression

If n realizations y_i are observed that are related to n realizations x_i by a factor α, the following linear relation is postulated [13]:

$$\begin{aligned} y_i &= \gamma + \alpha x_i + \epsilon_i \\ \mathbf{y} &= \gamma + \alpha \mathbf{x} + \epsilon \end{aligned} \tag{4.7}$$

$$\mathbf{y} = \begin{pmatrix} y_1 \\ \vdots \\ y_n \end{pmatrix} \qquad \mathbf{x} = \begin{pmatrix} x_1 \\ \vdots \\ x_n \end{pmatrix} \qquad \epsilon = \begin{pmatrix} \epsilon_1 \\ \vdots \\ \epsilon_n \end{pmatrix}$$

As defined in the Least Squares Minimization, the estimate minimizes the sum of squared errors (SSE) [13]:

$$\{\hat{\alpha}, \hat{\gamma}\} = arg_{\alpha,\gamma} min \sum_{i=1}^{n} (y_i - \gamma - \alpha x_i)^2$$

The slope $\hat{\alpha}$ and the intercept $\hat{\gamma}$ are:

$$\begin{aligned} \hat{\alpha} &= \frac{\sum_{i=1}^{n}(x_i - \bar{x})(y_i - \bar{y})}{\sum_{i=1}^{n}(x_i - \bar{x})^2} \\ \hat{\gamma} &= \bar{y} - \hat{\alpha}\bar{x} \end{aligned}$$

In the case of the model of energy transfer in the experimental set-up, the equation (4.2) can be reorganized to find a linear relation similar to (4.7):

$$\dot{m} c_{p,w} (\mathbf{T_{in}} - \beta \mathbf{T}) - \rho_w c_{p,w} V \dot{\mathbf{T}} = \alpha (\mathbf{T} - \mathbf{T_e})$$

This means that in (4.7):

$$\mathbf{y} = \dot{m} c_{p,w} (\mathbf{T_{in}} - \beta \mathbf{T}) - \rho_w c_{p,w} V \dot{\mathbf{T}} \tag{4.8}$$

$$\mathbf{x} = \mathbf{T} - \mathbf{T_e} \tag{4.9}$$

$$\gamma = 0$$

$$\epsilon = 0$$

Linear regression on all data

The temperatures measured during the three experiments (Section 3.3.2) and the derivatives computed in Section 4.7.1 are set in equations (4.8) and (4.9). The linear regression is made on the data of each experiment and can be seen on Figures 4.23, 4.24 and 4.25. The value of α is found being the slope of the red straight line [6].

As was seen in Section 4.6.2, the higher the value of β, the best the fitting so the objective was to find the highest value of β that gives positive α_{exp1}, α_{exp2} and α_{exp3}. This value is $\beta = 0.91$.

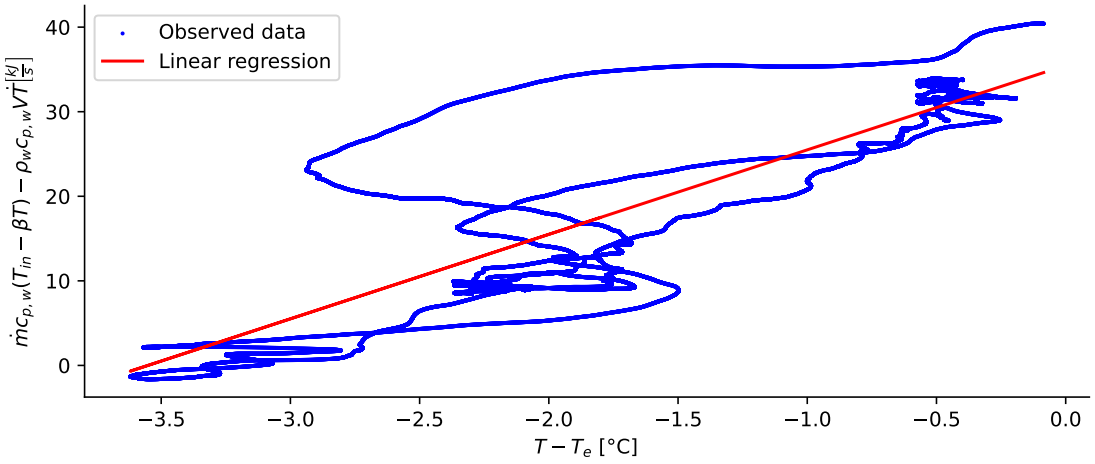

Figure 4.23: Linear regression on experiment 1 with $\beta = 0.91$ and $\dot{m} = 3.83 \frac{kg}{s}$

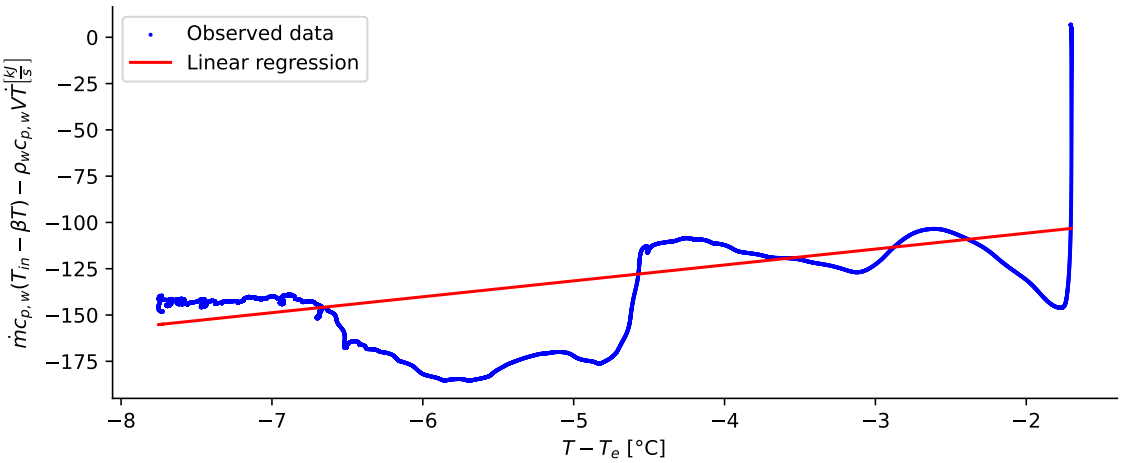

Figure 4.24: Linear regression on experiment 2 with $\beta = 0.91$ and $\dot{m} = 3.83 \frac{kg}{s}$

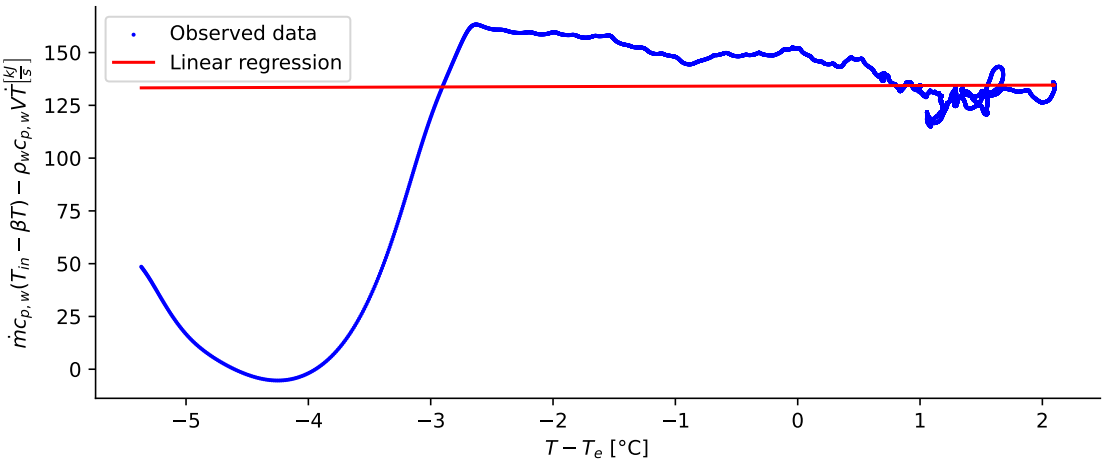

Figure 4.25: Linear regression on experiment 3 with $\beta = 0.91$ and $\dot{m} = 3.83\frac{kg}{s}$

The different values of α and their mean are reported in Table 4.4.

α_{exp1} $\left[\frac{kJ}{sK}\right]$	α_{exp2} $\left[\frac{kJ}{sK}\right]$	α_{exp3} $\left[\frac{kJ}{sK}\right]$	α_{mean} $\left[\frac{kJ}{sK}\right]$
9.98	8.586	0.176	6.251

Table 4.4: Values of α determined by linear regression on all data with $\beta = 0.91$ and $\dot{m} = 3.83\frac{kg}{s}$

The test of the model with these values, as explained in Section 4.5, give the following results. Figures 4.26, 4.27, 4.28 and 4.29 show respectively with α_{exp1}, α_{exp2}, α_{exp3} and α_{mean} on each experiment.

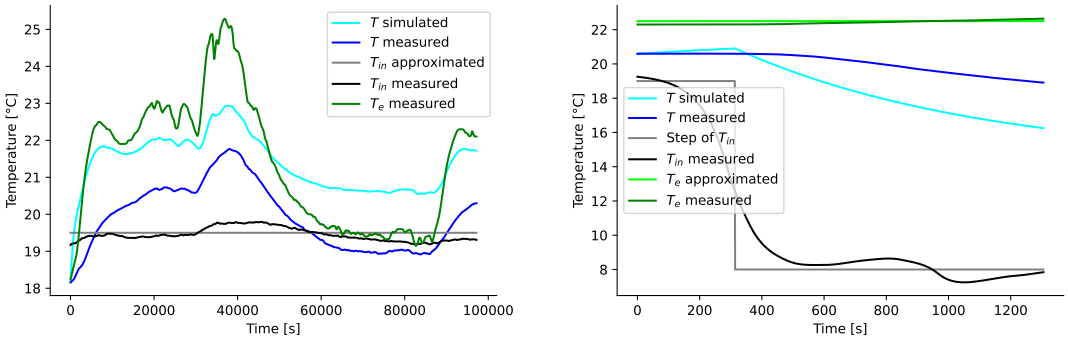

(a) (b)

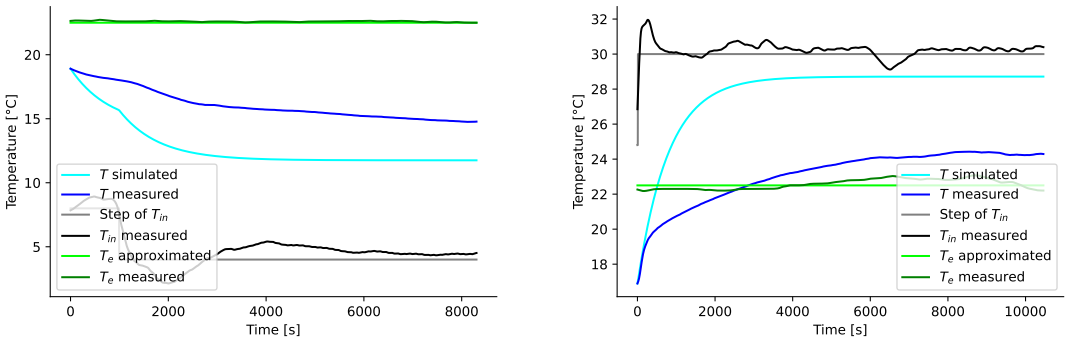

(c) (d)

Figure 4.26: Simulation of T during experiments (a) 1, (b) 2a, (c) 2b and (d) 3, using α_{exp1} from linear regression on experiment 1 with $\beta = 0.91$ and $\dot{m} = 3.83\frac{kg}{s}$

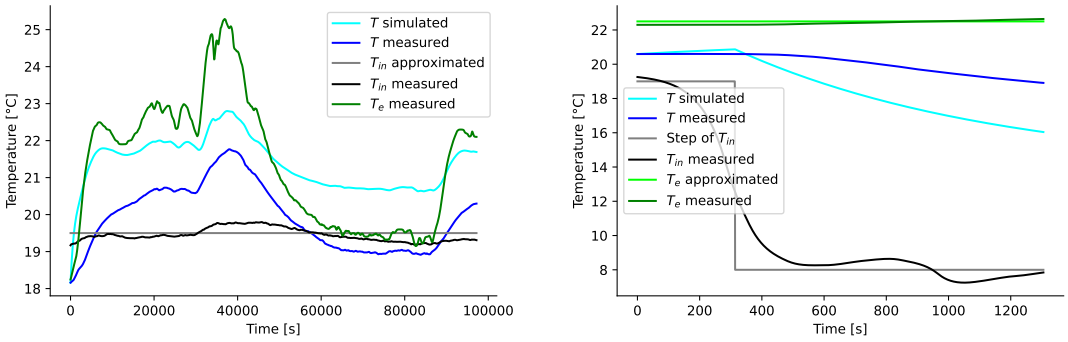

(a) (b)

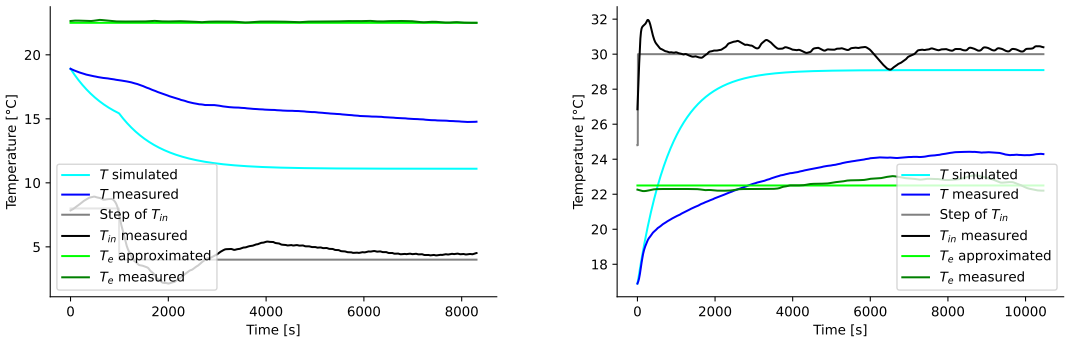

(c) (d)

Figure 4.27: Simulation of T during experiments (a) 1, (b) 2a, (c) 2b and (d) 3, using α_{exp2} from linear regression on experiment 2 with $\beta = 0.91$ and $\dot{m} = 3.83\frac{kg}{s}$

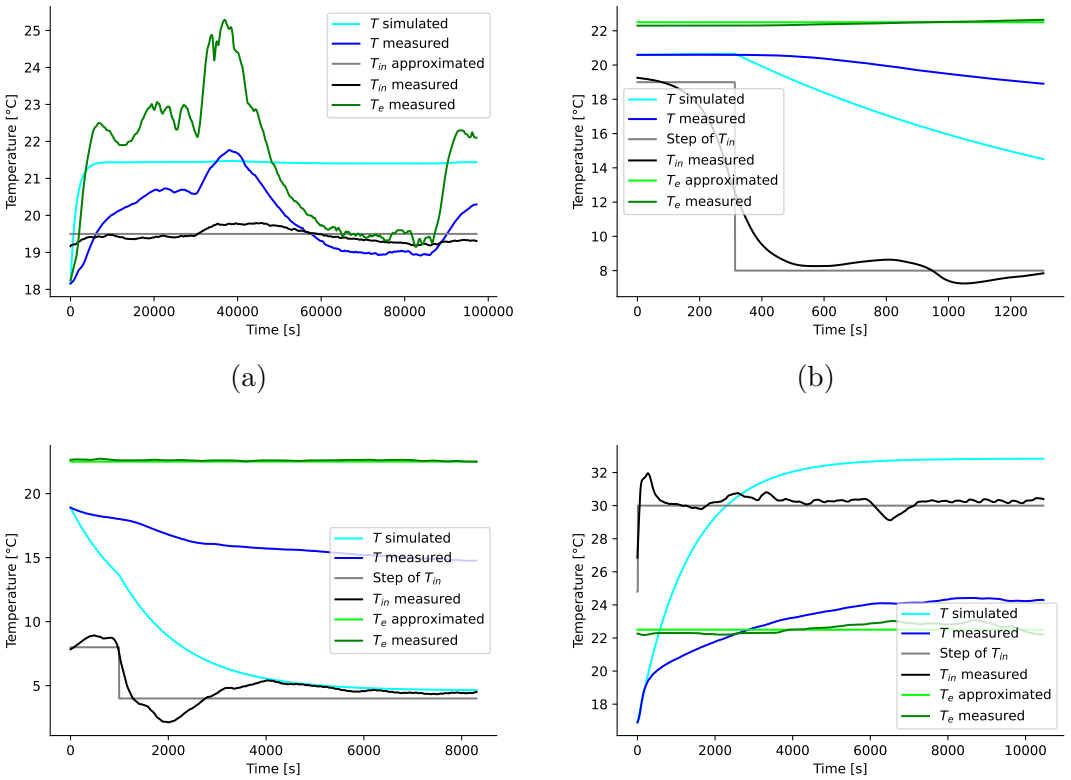

Figure 4.28: Simulation of T during experiments (a) 1, (b) 2a, (c) 2b and (d) 3, using α_{exp3} from linear regression on experiment 3 with $\beta = 0.91$ and $\dot{m} = 3.83\frac{kg}{s}$

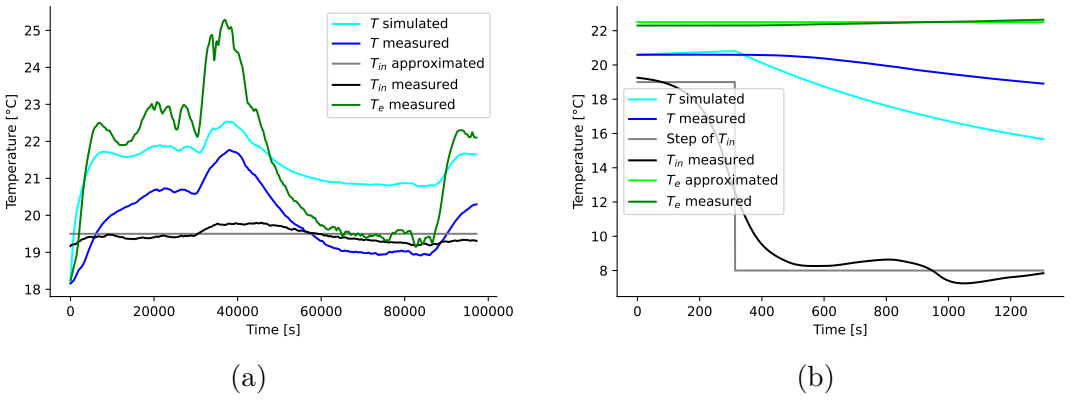

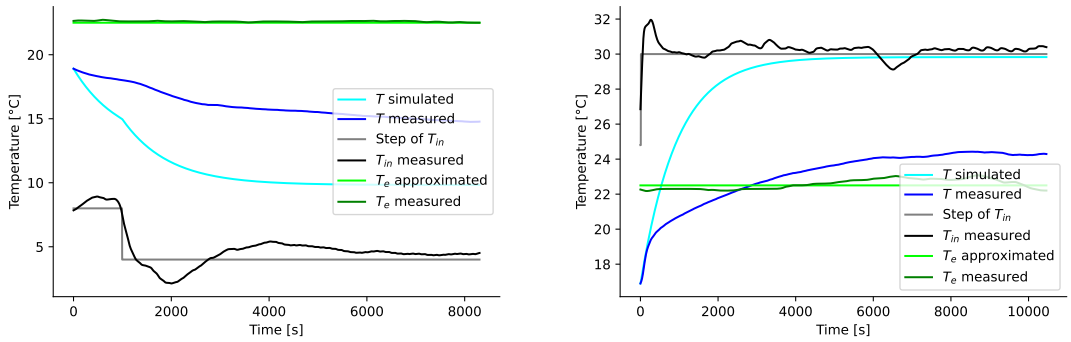

(c) (d)

Figure 4.29: Simulation of T during experiments (a) 1, (b) 2a, (c) 2b and (d) 3, using α_{mean} from the linear regressions with $\beta = 0.91$ and $\dot{m} = 3.83\frac{kg}{s}$

Linear regression on points of regime

An alternative to the method used above is to proceed a linear regression on only the points of regime of the experiments. These are points where the variation of T is zero. (4.2) becomes:

$$\dot{\mathbf{T}} = 0$$
$$0 = \dot{m}c_{p,w}(\mathbf{T_{in}} - \beta\mathbf{T}) + \alpha(\mathbf{T_e} - \mathbf{T})$$

(4.8) and (4.9) become:

$$\mathbf{y} = \dot{m}c_{p,w}(\mathbf{T_{in}} - \beta\mathbf{T}) \tag{4.10}$$
$$\mathbf{x} = \mathbf{T} - \mathbf{T_e} \tag{4.11}$$

The points of regime can be found in the Table 4.5.

	Experiment 1			Experiment 2	Experiment 3
T [°C]	20.68	18.95	20.29	14.88	24.23
T_e [°C]	22.8	19.5	22.1	22.5	22.2
T_{in} [°C]	19.44	19.26	19.31	4.81	30.25

Table 4.5: Temperatures of regime of each experiment

The temperatures of regime are set in equations (4.10) and (4.11). The linear regression is made on these points and can be seen on Figure 4.30. The value of α is found being the slope of the red straight line and is reported in Table 4.6. As can be observed, $\beta = 1$ gives a positive α.

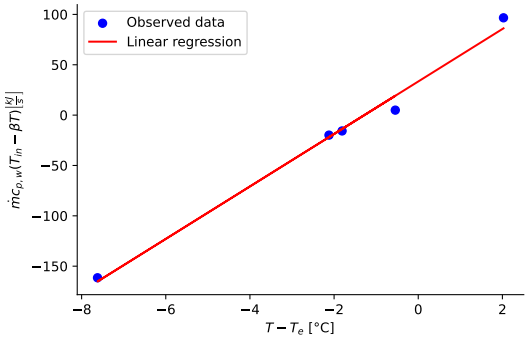

Figure 4.30: Linear regression on the points of regime of all experiments with $\beta = 1$ and $\dot{m} = 3.83\frac{kg}{s}$

α $\left[\frac{kJ}{sK}\right]$
26.054

Table 4.6: Value of α determined by linear regression on points of regime of experiments 1, 2 and 3 with $\beta = 1$ and $\dot{m} = 3.83\frac{kg}{s}$

The test of the model with this value of α, as explained in Section 4.5, give the Figure 4.31.

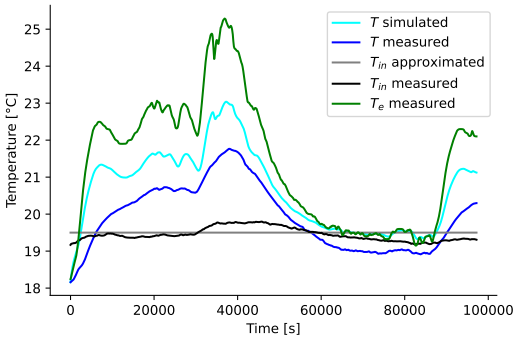

(a)

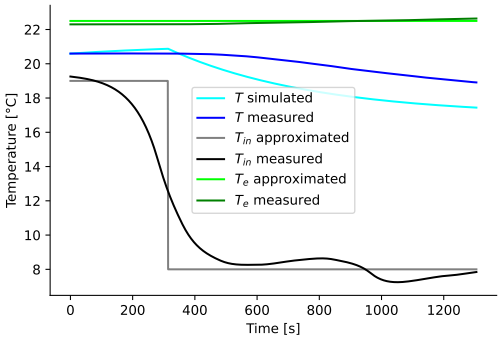

(b)

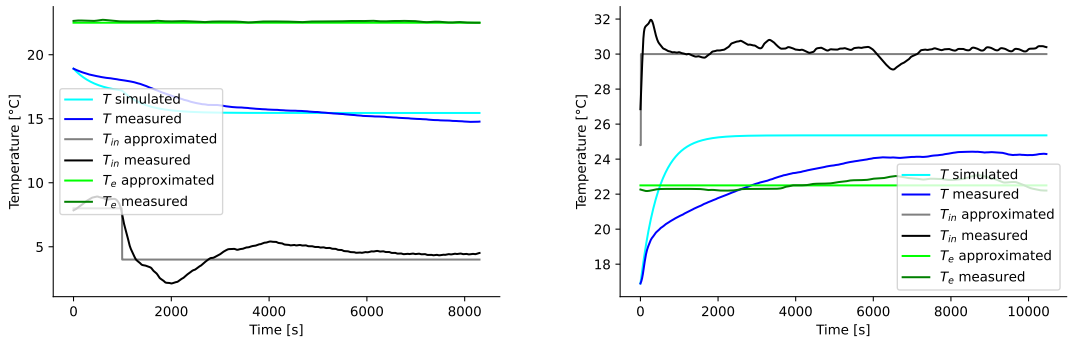

(c) (d)

Figure 4.31: Simulation of T during experiments (a) 1, (b) 2a, (c) 2b and (d) 3, using α from the linear regression on the points of regime of all experiments with $\beta = 1$ and $\dot{m} = 3.83 \frac{kg}{s}$

Linear regression on points of regime of experiment 1

Another alternative is to proceed a linear regression only on the points of regime of experiment 1 which are listed in Table 4.5. This can be seen on Figure 4.32. The value of α is found being the slope of the red straight line and is reported in Table 4.7.

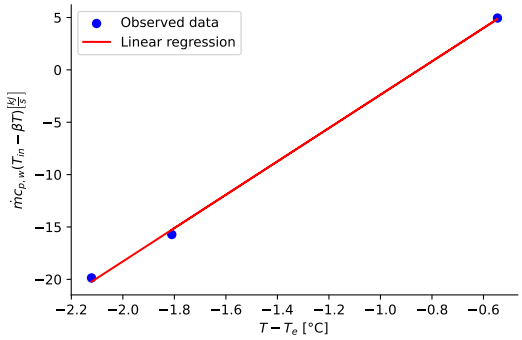

Figure 4.32: Linear regression on the points of regime of experiment 1 with $\beta = 1$ and $\dot{m} = 3.83 \frac{kg}{s}$

α $\left[\frac{kJ}{sK}\right]$
15.919

Table 4.7: Value of α determined by linear regression on points of regime of experiment 1 with $\beta = 1$ and $\dot{m} = 3.83 \frac{kg}{s}$

The test of the model with this value of α, as explained in Section 4.5, give the Figure 4.33.

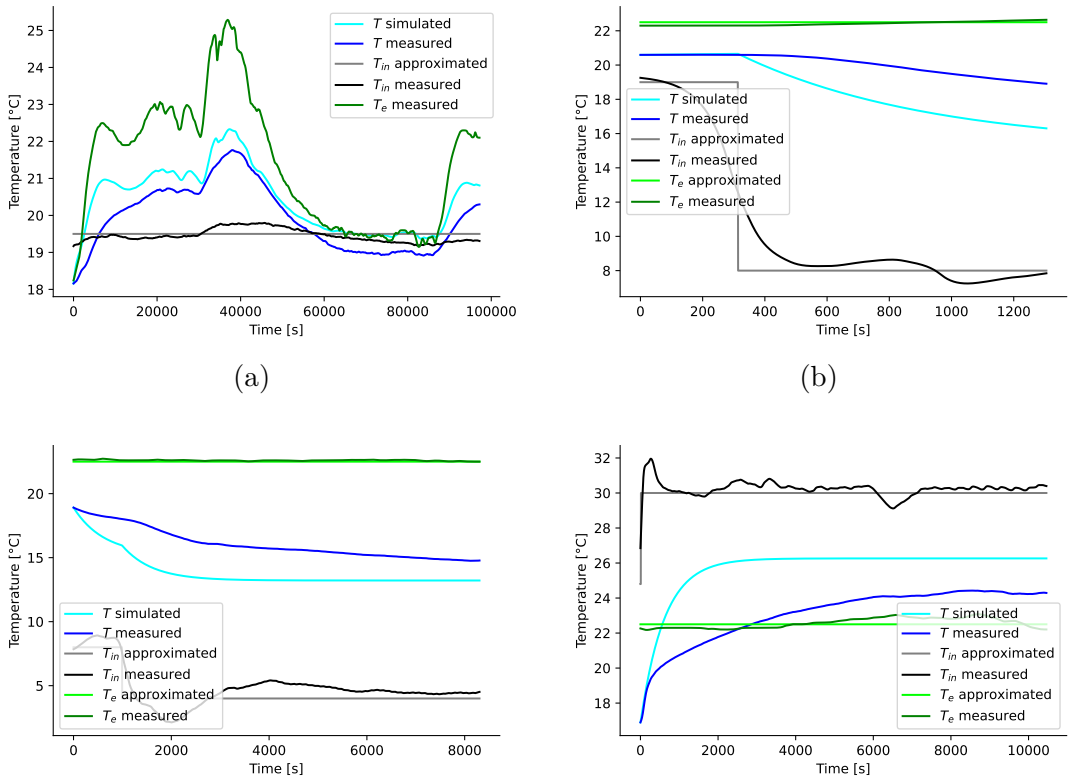

Figure 4.33: Simulation of T during experiments (a) 1, (b) 2a, (c) 2b and (d) 3, using α from the linear regression on the points of regime of experiment 1 with $\beta = 1$ and $\dot{m} = 3.83\frac{kg}{s}$

Linear regression on points of regime of experiments 2 and 3

Another alternative is to proceed a linear regression only on the points of regime of experiment 2 and 3 which are listed in Table 4.5. This can be seen on Figure 4.34. The value of α is found being the slope of the red straight line and is reported in Table 4.8.

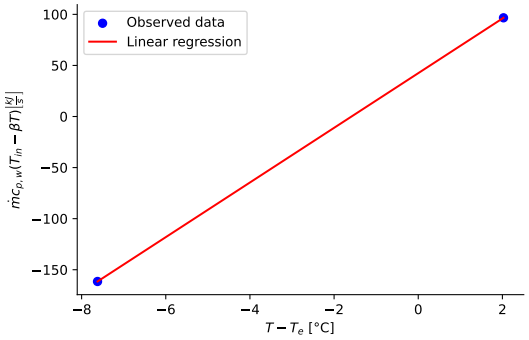

Figure 4.34: Linear regression on the points of regime of experiments 2 and 3 with $\beta = 1$ and $\dot{m} = 3.83\frac{kg}{s}$

α $\left[\frac{kJ}{sK}\right]$
26.754

Table 4.8: Value of α determined by linear regression on points of regime of experiments 2 and 3 with $\beta = 1$ and $\dot{m} = 3.83\frac{kg}{s}$

The test of the model with this value of α, as explained in Section 4.5, gives the Figure 4.35.

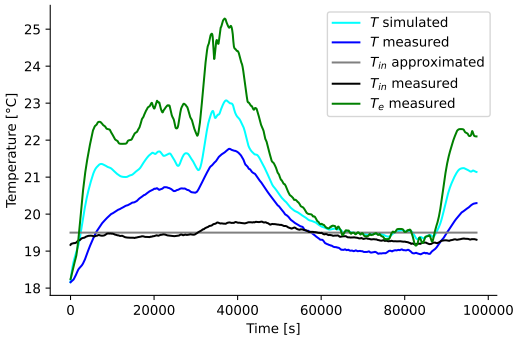

(a)

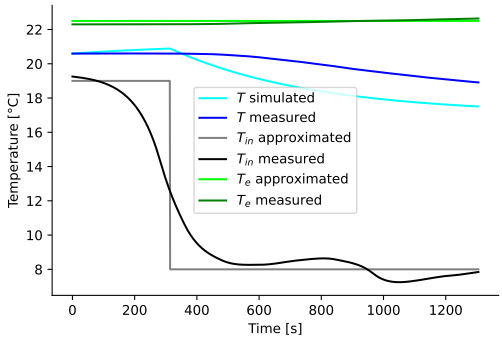

(b)

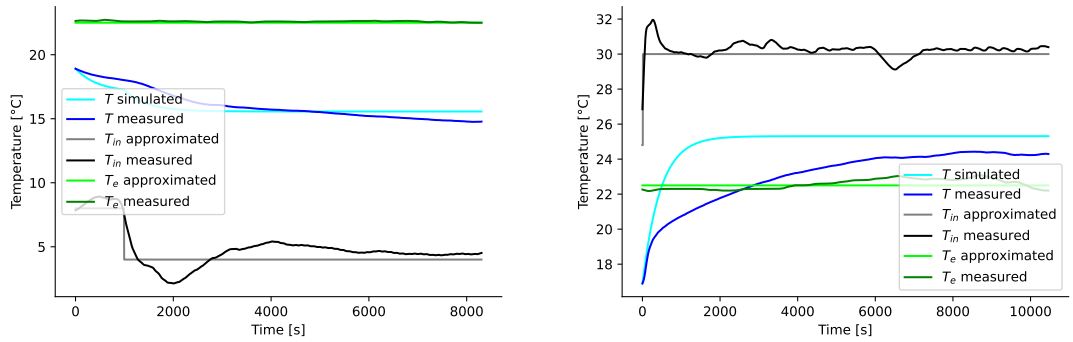

(c) (d)

Figure 4.35: Simulation of T during experiments (a) 1, (b) 2a, (c) 2b and (d) 3, using α from the linear regression on the points of regime of experiments 2 and 3 with $\beta = 1$ and $\dot{m} = 3.83\frac{kg}{s}$

With $\beta = 1$ and $\dot{m} = 3.83\frac{kg}{s}$, the higher the value of α, the better the simulation of T with the model (4.2). The selected value is:

$$\alpha = 26.754\frac{kJ}{sK}$$

4.8 Measured mass flow rate of misting solution

The real value of the mass flow rate of the misting solution is measured between the exit of the reservoir tank and the entrance of the filter F1 (see Figure 3.2). At this location, the circuit is cut so that the source of water could become another tank containing 10 liters of water instead of the reservoir tank. Indeed, the part of the circuit from the pump until the misting nozzles is linked by a pipe to this new water. This other tank is set on a scale. When the pump operates, the water from the tank is pumped. The mass loss measured by the scale during a certain time gives the mass flow rate of the misting solution.
During 10 seconds, $0.807kg$ is pumped, giving a mass flow of $0.0807\frac{kg}{s}$. While during 60 seconds, $5.731kg$ is pumped, giving a mass flow of $0.0955\frac{kg}{s}$. The real value of the mass flow rate of misting solution is supposed to be the mean value between the two measurements:

$$\dot{m} = 0.0881\frac{kg}{s}$$

The four methods of linear regression (see Section 4.7.2) are applied once again but with this new value of $\dot{m}$ and $0 \leq \beta \leq 1$. The values that were found by linear

regression on all the data measured during the three experiments, on the points of regime of the three experiments, on the points of regime of only experiment 1 and on the points of regime of only experiments 2 and 3 are respectively reported in the Tables 4.9, 4.10, 4.11 and 4.12 for different values of β.

β [−]	α_{exp1} $\left[\frac{kJ}{sK}\right]$	α_{exp2} $\left[\frac{kJ}{sK}\right]$	α_{exp3} $\left[\frac{kJ}{sK}\right]$	α_{mean} $\left[\frac{kJ}{sK}\right]$
0	0.879	4.384	17.775	7.679
0.25	0.944	4.294	17.67	7.636
0.5	1.01	4.204	17.566	7.593
0.75	1.075	4.114	17.461	7.55
1	1.14	4.024	17.356	7.507

Table 4.9: Values of α determined by linear regression on all the data with $\dot{m} = 0.0881\frac{kg}{s}$

β [−]	α $\left[\frac{kJ}{sK}\right]$
0	0.925
0.25	0.844
0.5	0.762
0.75	0.68
1	0.599

Table 4.10: Values of α determined by linear regression on the points of regime of experiments 1, 2 and 3 with $\dot{m} = 0.0881\frac{kg}{s}$

β [−]	α $\left[\frac{kJ}{sK}\right]$
0	- 0.0334
0.25	0.0664
0.5	0.166
0.75	0.266
1	0.366

Table 4.11: Values of α determined by linear regression on the points of regime of experiment 1 with $\dot{m} = 0.0881\frac{kg}{s}$

β [−]	α $\left[\frac{kJ}{sK}\right]$
0	0.972
0.25	0.883
0.5	0.794
0.75	0.704
1	0.615

Table 4.12: Values of α determined by linear regression on the points of regime of experiments 2 and 3 with $\dot{m} = 0.0881\frac{kg}{s}$

Simulating T with all these different values of α and β, quite good approximations are only obtained in the cases of linear regression on the points of regime with $\beta = 1$ (marked in orange in the Tables 4.10, 4.11 and 4.12). It can be seen on Figures 4.37, 4.39 and 4.41. For the sake of clarity, the simulations with the other possible parameters are not reported here.

The linear regression on the points of regime of experiments 1, 2 and 3 with $\beta = 1$ is seen on Figure 4.36 and the value of α is highlighted in Table 4.13.

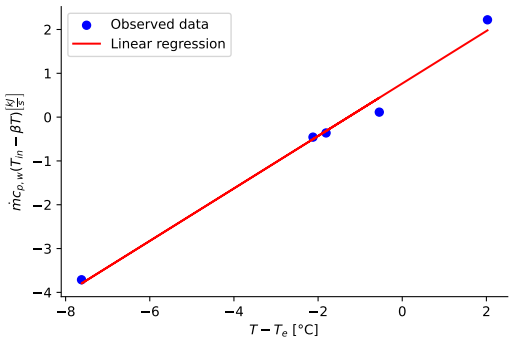

Figure 4.36: Linear regression on the points of regime of all experiments with $\beta = 1$ and $\dot{m} = 0.0881\frac{kg}{s}$

β [−]	α $\left[\frac{kJ}{sK}\right]$
1	0.599

Table 4.13: Values of α determined with linear regression on the points of regime of experiments 1, 2 and 3 with $\beta = 1$ and $\dot{m} = 0.0881\frac{kg}{s}$

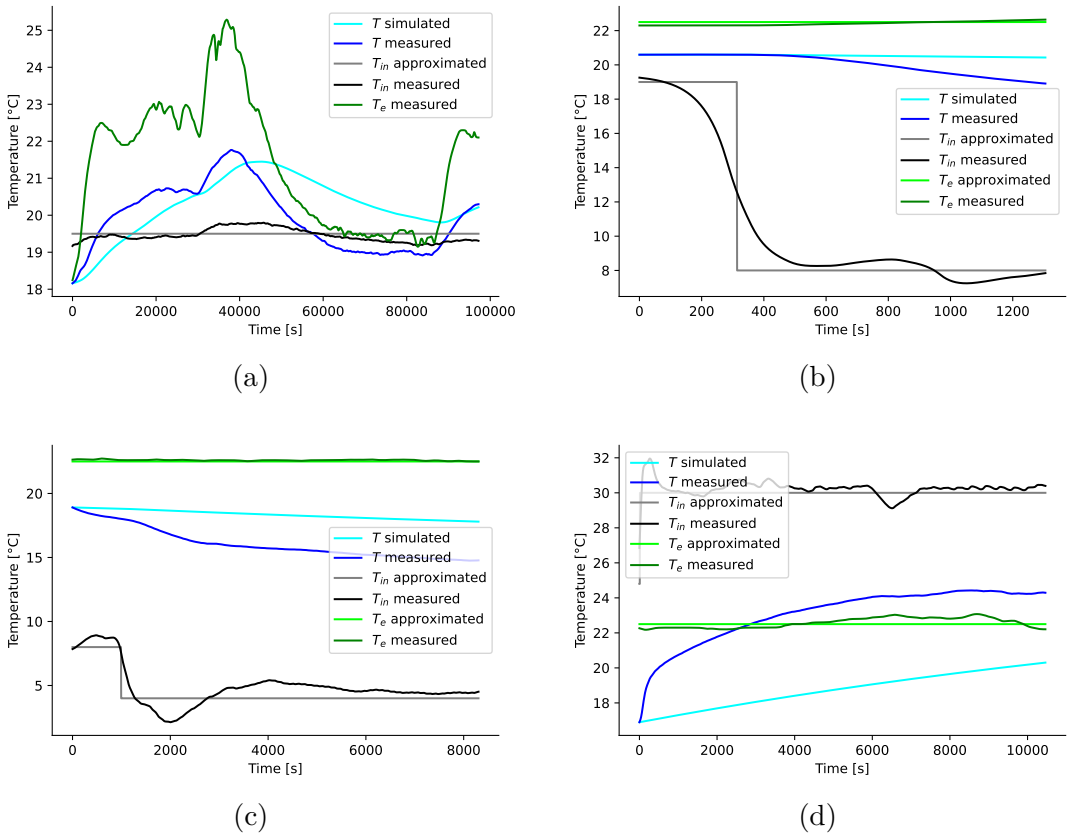

Figure 4.37: Simulation of T during experiments (a) 1, (b) 2a, (c) 2b and (d) 3, using α from the linear regression on the points of regime of all experiments with $\beta = 1$ and $\dot{m} = 0.0881\frac{kg}{s}$

The linear regression on the points of regime of experiment 1 with $\beta = 1$ is seen on Figure 4.38 and the value of α is highlighted in Table 4.14.

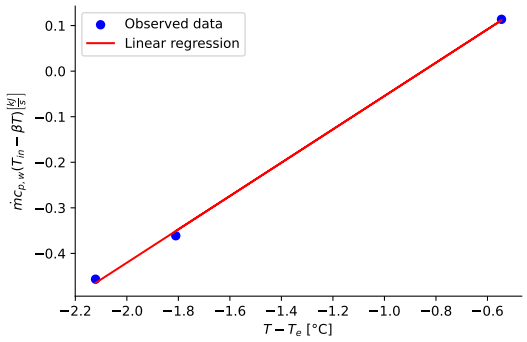

Figure 4.38: Linear regression on the points of regime of experiment 1 with $\beta = 1$ and $\dot{m} = 0.0881\frac{kg}{s}$

β [−]	α $\left[\frac{kJ}{sK}\right]$
1	0.366

Table 4.14: Values of α determined with linear regression on the points of regime of experiment 1 with $\beta = 1$ and $\dot{m} = 0.0881\frac{kg}{s}$

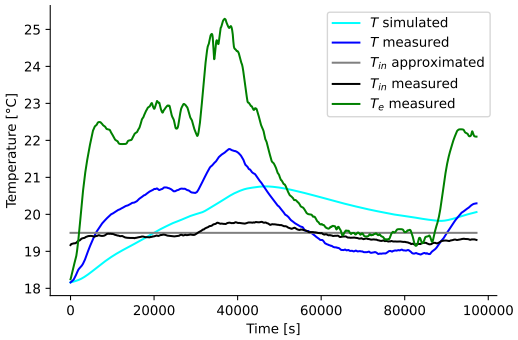

(a)

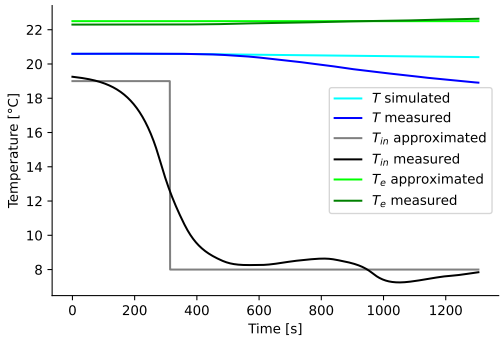

(b)

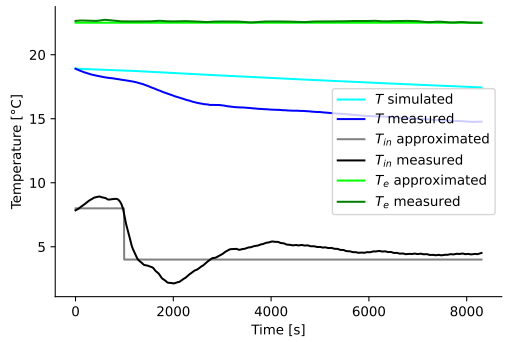

(c)

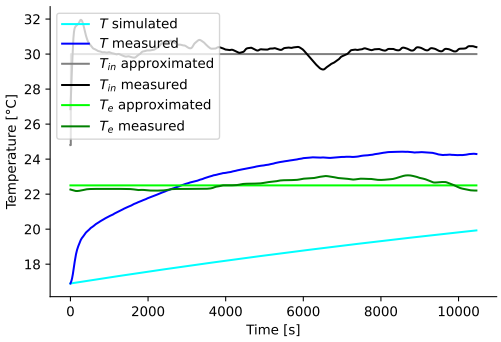

(d)

Figure 4.39: Simulation of T during experiments (a) 1, (b) 2a, (c) 2b and (d) 3, using α from the linear regression on the points of regime of experiment 1 with $\beta = 1$ and $\dot{m} = 0.0881 \frac{kg}{s}$

The linear regression on the points of regime of experiments 2 and 3 with $\beta = 1$ is seen on Figure 4.40 and the value of α is highlighted in Table 4.15.

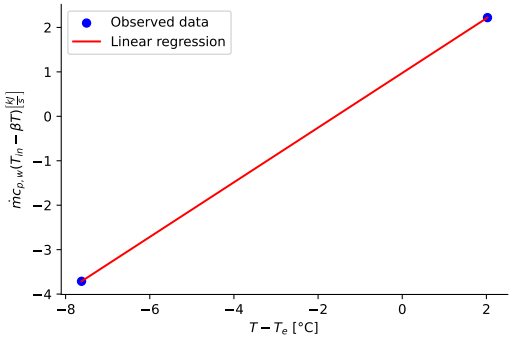

Figure 4.40: Linear regression on the points of regime of experiments 2 and 3 with $\beta = 1$ and $\dot{m} = 0.0881 \frac{kg}{s}$

β [−]	α $\left[\frac{kJ}{sK}\right]$
1	0.615

Table 4.15: Values of α determined with linear regression on the points of regime of experiments 2 and 3 with $\beta = 1$ and $\dot{m} = 0.0881 \frac{kg}{s}$

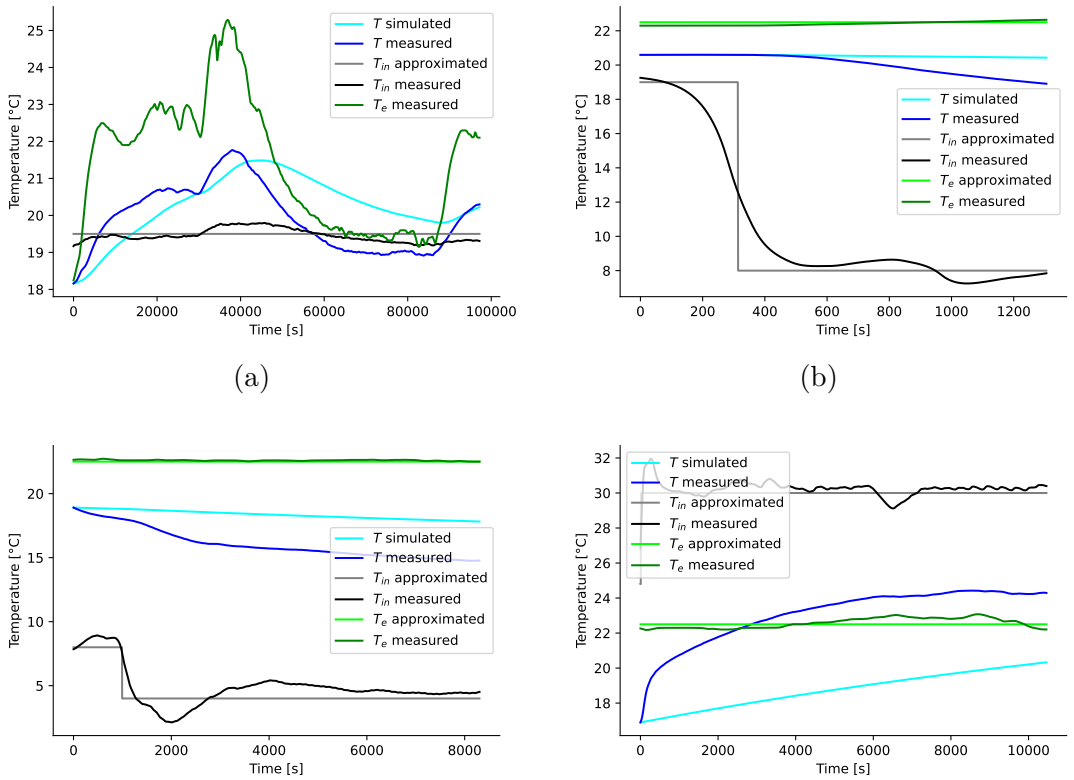

Figure 4.41: Simulation of T during experiments (a) 1, (b) 2a, (c) 2b and (d) 3, using α from the linear regression on the points of regime of experiment 2 and 3 with $\beta = 1$ and $\dot{m} = 0.0881 \frac{kg}{s}$

With $\beta = 1$ and $\dot{m} = 0.0881 \frac{kg}{s}$, the higher the value of α, the better the simulation of T with the model (4.2). The selected value is:

$$\alpha = 0.615 \frac{kJ}{sK}$$

Chapter 5

Design and implementation of control strategy

5.1 Overview

In the previous chapter, the model governing the heat exchanges in the experimental set-up was established.
From it, it is possible to predict how the temperature inside the chamber will behave in function of the temperatures of the greenhouse and of the misted solution.

The objective of this chapter is to design and implement a control strategy based on this model in order to control the temperature inside the chamber T in spite of variations of the greenhouse temperature T_e, by varying the misting temperature T_{in}.

Firstly, an introduction to the control strategy that is going to be implemented, namely a proportional-integral (PI) controller, is given.
Then, the direct synthesis of the system is made to find the parameters needed to implement the PI controller.
After, the PI controller is tested in simulation with new measurements of the greenhouse temperature.
Finally, a simulation of misting at a constant temperature is tested.

5.2 PI controller

In the language of system dynamics, the differential equation that describes the dynamics of temperature (4.2) is called state equation.
The output or controlled variables are those that are either accessible for real-time measurement or those that are intended to be influenced. In this case, this variable

is the temperature of the chamber T.
Additionally, the input variables are the variables that can be externally manipulated or whose external variations can induce a dynamic evolution of the process. Among the input variables, a distinction is made between control variables and disturbance variables. The control variables allow influencing the process behavior via a control system. In this case, this variable is the temperature of the misted solution T_{in}.
The disturbance variables have a potentially negative effect on the nominal behavior of the process and their action primarily justifies the use of control to mitigate their effect. In this case, this variable is the temperature of the greenhouse T_e [11].

The PI controller, as can be seen on Figure 5.1, permits to control T_{in} in function of the set-point T^* and the controlled variable T.

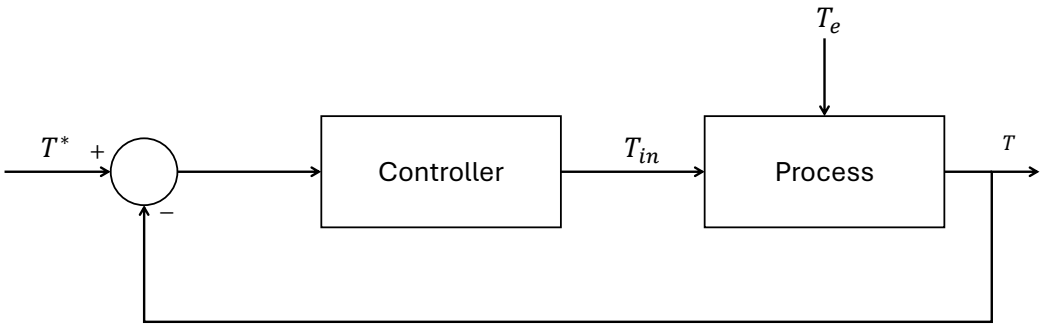

Figure 5.1: Closed-loop system diagram [11]

The PI controller is a type of feedback controller. It combines two control modes. The proportional (P) control mode produces a control output that is proportional to the current error value $(T^* - T)$. The integral (I) control mode produces a control output based on the accumulation of past errors [11].
The equation of the PI controller is:

$$T_{in}(t) = K_p(T^* - T) + \frac{K_p}{\tau_i}\int_0^t [T^*(\tau) - T(\tau)]d\tau \tag{5.1}$$

The proportional action is $K_p(T^* - T)$ and the integral action is $\frac{K_p}{\tau_i}\int_0^t [T^*(\tau) - T(\tau)]d\tau$. The form (5.1) of the PI controller is its variational form. In fact, the actual control action is found by adding a reference term T^*_{in} [11].

5.3 Direct synthesis with delay

The parameters of the PI controller are the proportional gain K_p and the integral time constant τ_i as can be seen in (5.1). A procedure to determine these parameters is the direct synthesis.

In direct synthesis, the objective is to impose a dynamic on the closed-loop system and to determine the control structure to achieve it [11].

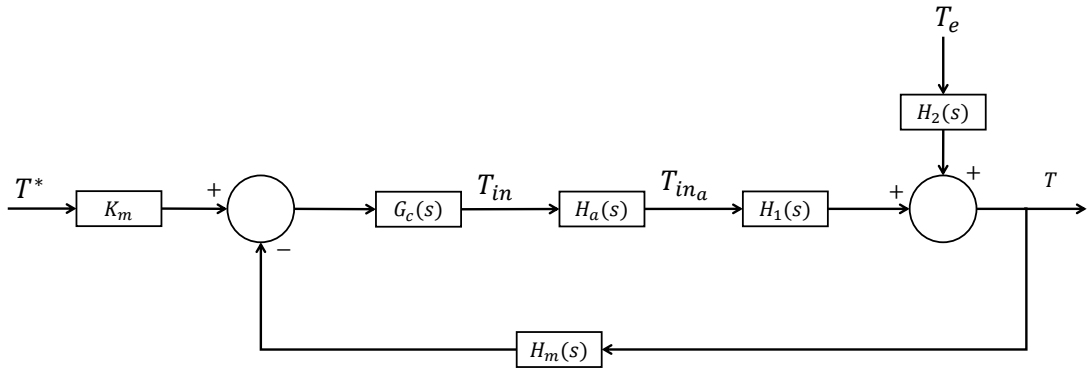

Figure 5.2: Closed-loop system diagram as transfer functions [11]

On Figure 5.2, $G_c(s)$ denotes the transfer function of the controller and $H_a(s)$ and $H_m(s)$ are respectively the transfer functions of the actuator and the measurement system of the controlled variable. The output signal from the sensor ($H_m(s)$) is transmitted to the control system and has dimensions of an electrical or pneumatic signal, not those of T. Thus, a transfer function K_m ($= H_m(0)$) is added between the set-point T^* and its entry point in the block diagram. The transfer functions between the controlled variable T and the two external inputs of the closed-loop system T^* and T_e neglecting sensor ($H_m(s)$) and actuator ($H_a(s)$) dynamics are [11]:

$$T(t) = G_1(s)T^*(t) + G_2(s)T_e(t)$$

$$G_1(s) = \frac{H_1(s)G_c(s)}{1 + H_1(s)G_c(s)} \tag{5.2}$$

$$G_2(s) = \frac{H_2(s)}{1 + H_1(s)G_c(s)} \tag{5.3}$$

The transfer function of the PI controller is [11]:

$$G_c(s) = K_p \frac{1 + s\tau_i}{s\tau_i} \tag{5.4}$$

With (5.2) and (5.3), it is obtained that:

$$G_c(s) = \frac{1}{H_1(s)} \frac{G_{dy}(s)}{1 - G_{dy}(s)} \tag{5.5}$$

The reaction of T when T_e varies is delayed. The transfer function of the process dynamics is therefore (4.3) multiplied by a term for delay [11]:

$$H_1(s) = e^{-s\theta} \frac{K_{in}}{1 + s\tau} \tag{5.6}$$

The aim is to achieve the desired dynamic behavior between the controlled variable and the setpoint [11]:

$$T(t) = G_{dy}(s)T^*(t)$$

The desired closed-loop dynamics is [11]:

$$G_{dy}(s) = \frac{e^{-s\theta}}{1 + s\tau_d} \tag{5.7}$$

Replacing (5.6) and (5.7) in (5.5), the transfer function of the controller is expressed as:

$$G_c(s) = \frac{1 + s\tau}{K_{in}(1 + s\tau_d - e^{-s\theta})} \tag{5.8}$$

The delay is approximated by a Taylor approximation [11]:

$$e^{-s\theta} \approx 1 + s\theta$$

(5.8) becomes:

$$G_c(s) = \frac{1 + s\tau}{K_{in}(\tau_d + \theta)s} \tag{5.9}$$

Comparing (5.4) and (5.9), the parameters of the Pi controller are found with:

$$\tau_i = \tau$$
$$K_p = \frac{\tau}{K_{in}(\tau_d + \theta)}$$

The delay is found by observation on the temperature measurements on Figures 4.9, 4.10 and 4.11. It is supposed to be:

$$\theta = 300s$$

The closed-loop time constant τ_d represents the speed with which the system reacts after the initial delay. It is chosen to be:

$$\tau_d = \frac{\tau}{2}$$

5.4 Simulation of the PI controller

To simulate the PI controller, data is used from a previous experiment that took place in 2021. The temperature of the greenhouse measured by the probe of the "ARIA" supervision system of the greenhouses between 1 p.m. on May 25, 2021 and 9:50 a.m. on June 30, 2021 can be seen on Figure 5.3. This set of temperatures can be considered as the worst case scenario.

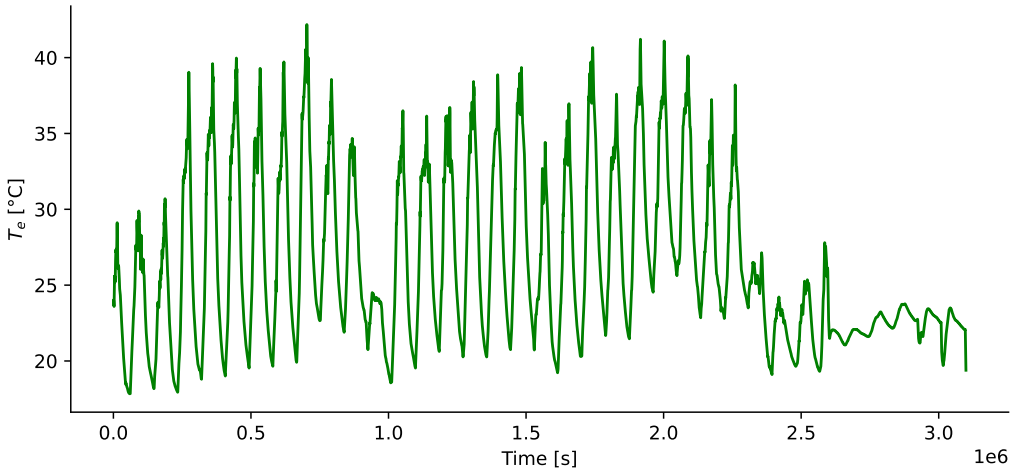

Figure 5.3: Temperature of the greenhouse measured by the probe of the "ARIA" supervision system of the greenhouses between 1 p.m. on May 25, 2021 and 9:50 a.m. on June 30, 2021

The simulation of the temperature T when considering there is no control system can be seen on Figures 5.4 and 5.5. The temperature of the misted water is then by default 19.5 °C as was seen in experiments in 3.3.2.
For the case with $\dot{m} = 3.83\frac{kg}{s}$, T fluctuates between 18.46 °C and 33.91 °C. For the case with $\dot{m} = 0.0881\frac{kg}{s}$, T fluctuates between 19.5 °C and 29.51 °C. Whatever the case, the temperature of the chamber reaches non-recommended values for the plant roots. Indeed, according to a researcher, the plants need to grow in aeroponics in a temperature range between 15 °C and 25 °C.

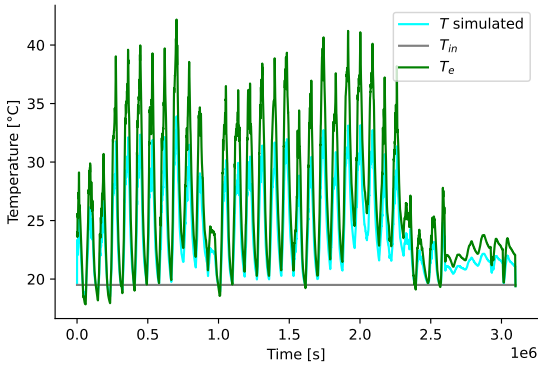

Figure 5.4: Simulation of T when T_{in} is not regulated with $\dot{m} = 3.83\frac{kg}{s}$ and $\alpha = 26.754\frac{kJ}{sK}$

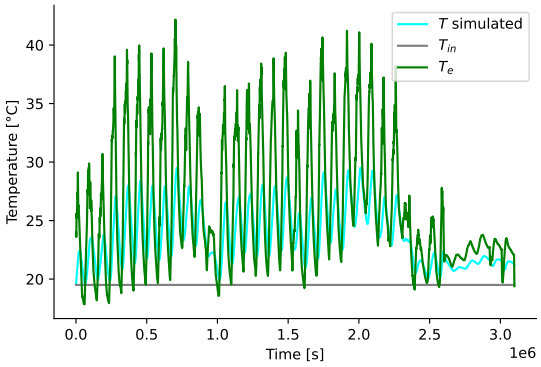

Figure 5.5: Simulation of T when T_{in} is not regulated with $\dot{m} = 0.0881\frac{kg}{s}$ and $\alpha = 0.615\frac{kJ}{sK}$

The set-point temperature T^* is set arbitrarily to 18°C to simulate the PI controller with the values selected in Chapter 4. The simulation for a mass flow rate of $\dot{m} = 3.83\frac{kg}{s}$ ($\alpha = 26.754\frac{kJ}{sK}$) is seen on Figure 5.6. The temperatures vary between 15.83 °C and 18.94 °C, so the required range is respected.

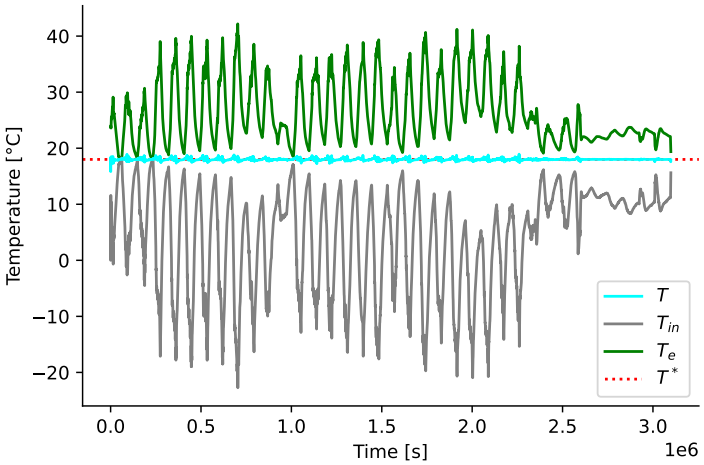

$$min(T) = 15.83°C$$
$$mean(T) = 18°C$$
$$max(T) = 18.94°C$$

Figure 5.6: Simulation of the PI regulation with $\dot{m} = 3.83\frac{kg}{s}$ and $\alpha = 26.754\frac{kJ}{sK}$

The simulation for a mass flow rate of $\dot{m} = 0.0881\frac{kg}{s}$ ($\alpha = 0.615\frac{kJ}{sK}$) is seen on Figure 5.7. The temperatures vary between 16.31 °C and 20.29 °C, so the required range is also respected.

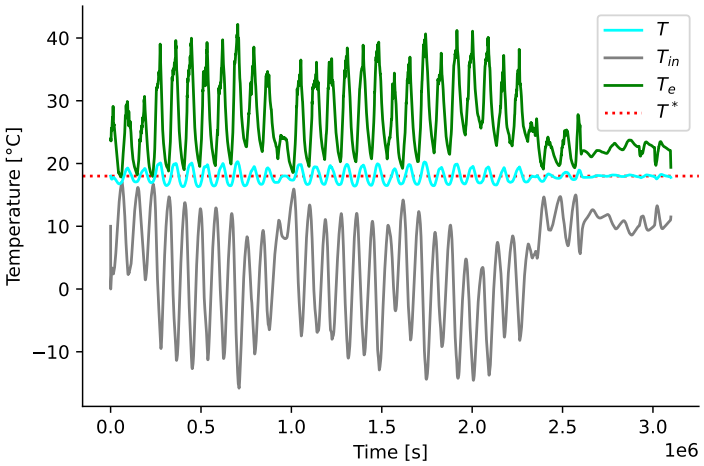

$$min(T) = 16.31°C$$
$$mean(T) = 17.99°C$$
$$max(T) = 20.29°C$$

Figure 5.7: Simulation of PI regulation with $\dot{m} = 0.0881\frac{kg}{s}$ and $\alpha = 0.615\frac{kJ}{sK}$

According to a researcher, misting water colder than 10°C can cause root damage. So a lower bound for the temperature of the misting water is set to 10°C. The simulation for a mass flow rate of $\dot{m} = 3.83\frac{kg}{s}$ ($\alpha = 26.754\frac{kJ}{sK}$) is seen on Figure 5.8. The temperatures vary between 14.97 °C and 29.81 °C, so the required range is not respected. In fact, if the equation of the model (4.2) is considered at steady state ($\dot{T} = 0$) with misted water at $T_{in} = 10°C$, which is the lowest temperature permitted:

$$T_e = \rho_w c_{p,w} V\dot{T} + \frac{\dot{m}c_{p,w}}{\alpha}(\beta T - T_{in}) + T$$
$$\text{if } T \leq 25°C \Rightarrow T_e \leq 34°C$$

When T_e is above 34 °C, the misting water is not enough cold to decrease T below 25 °C.

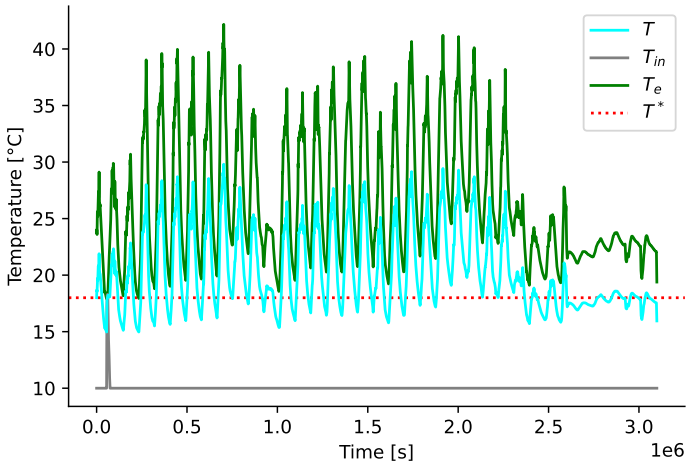

$$min(T) = 14.97°C$$
$$mean(T) = 20.2°C$$
$$max(T) = 29.81°C$$

Figure 5.8: Simulation of the PI regulation with $T_{in} \geq 10°C$, $\dot{m} = 3.83\frac{kg}{s}$ and $\alpha = 26.754\frac{kJ}{sK}$

The simulation for a mass flow rate of $\dot{m} = 0.0881\frac{kg}{s}$ ($\alpha = 0.615\frac{kJ}{sK}$) is seen on Figure 5.9. The temperatures vary between 16.09 °C and 25.92 °C, so the required range can be considered to be respected. The reasoning made for the case with $\dot{m} = 3.83\frac{kg}{s}$ is not satisfied here because the mass flow rate and α are smaller. The variation $\dot{T}$ in (4.2) is much smaller at each step. T is thus less influenced by the variations in T_{in} and T_e.

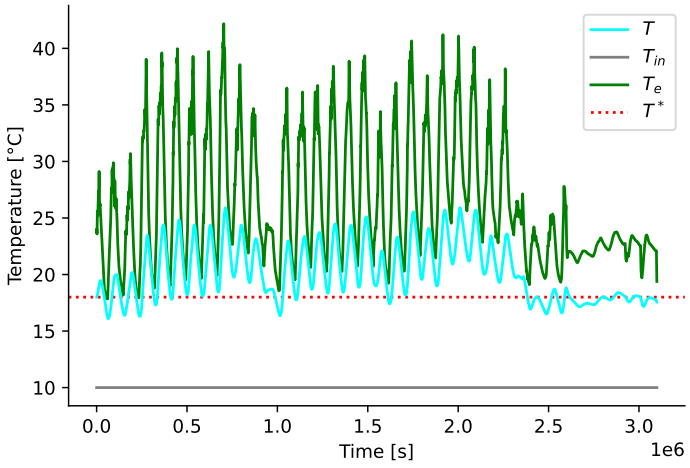

$$min(T) = 16.09°C$$
$$mean(T) = 20.19°C$$
$$max(T) = 25.92°C$$

Figure 5.9: Simulation of PI regulation with $T_{in} \geq 10°C$, $\dot{m} = 0.0881\frac{kg}{s}$ and $\alpha = 0.615\frac{kJ}{sK}$

5.5 Constant misting

As can be seen on Figures 5.8 and 5.9, a misting at constant temperature could be feasible because of the lower bound constraint. The simulation for a mass flow rate of $\dot{m} = 3.83\frac{kg}{s}$ ($\alpha = 26.754\frac{kJ}{sK}$) and of $\dot{m} = 0.0881\frac{kg}{s}$ ($\alpha = 0.615\frac{kJ}{sK}$) can be seen on respectively Figure 5.10 and Figure 5.11.

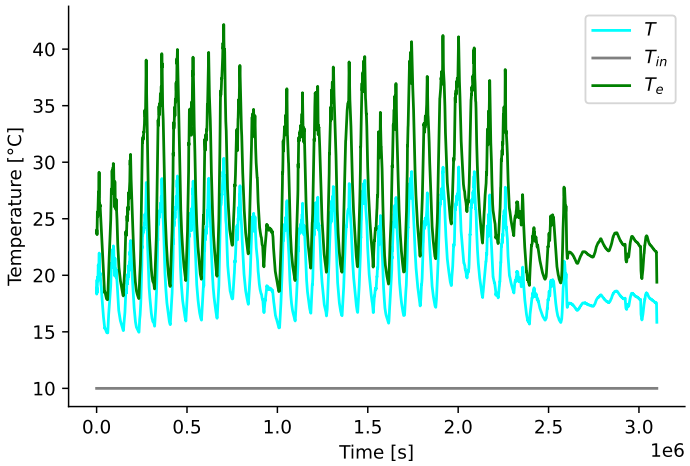

$$min(T) = 14.9°C$$
$$mean(T) = 20.19°C$$
$$max(T) = 30.35°C$$

Figure 5.10: Simulation of a misting at 10°C with $\dot{m} = 3.83\frac{kg}{s}$ and $\alpha = 26.754\frac{kJ}{sK}$

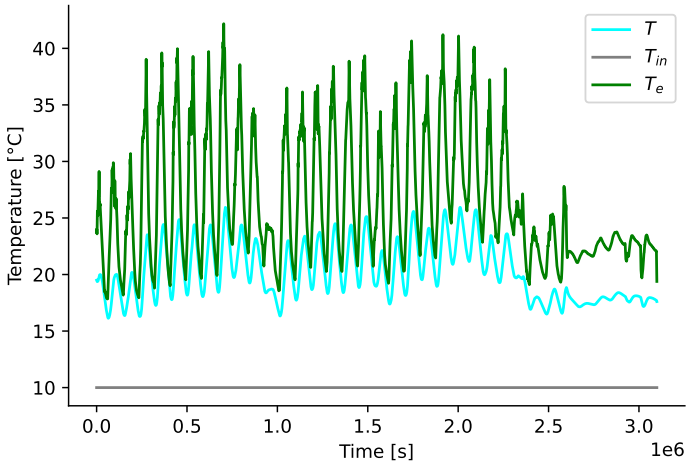

$$min(T) = 16.13°C$$
$$mean(T) = 20.2°C$$
$$max(T) = 25.95°C$$

Figure 5.11: Simulation of a misting at 10°C with $\dot{m} = 0.0881\frac{kg}{s}$ and $\alpha = 0.615\frac{kJ}{sK}$

Chapter 6

Practical implementation

6.1 Overview

In the previous chapter, it was observed that misting water at a constant temperature T_{in} can regulate the temperature inside the chamber T.

In this chapter, the implementation of this solution in practice is described and the regulation of T is verified.

Firstly, a new circuit must be built to modify the temperature of the misting solution. The description of it is made.
Subsequent to this, measurements are made in this evolved setup to verify if the objective of regulation is reached and if there is a significant improvement compared to the initial setup.

6.2 Cooling circuit of the misting solution

The misting and cooling circuits are represented on Figure 6.1. A vertical beer-cooler of 60 liters (model "TR – 60") of the Antoine brand is used. Its specifications can be found in Appendix D. The agitator pump has been removed for this application.

It operates following a refrigeration cycle (illustrated in orange) with R134a as the refrigerant fluid. The gaseous refrigerant enters the compressor (C) where it is compressed, increasing its pressure and temperature. At this stage, the fluid is a hot gas at high pressure. The refrigerant then flows to the condenser (Cond) where it releases heat to the outside of the cooler and condenses into a high-pressure liquid. The refrigerant then passes through the expansion valve (V) where the

pressure of the fluid drops sharply, which also lowers its temperature. The fluid is now a mixture of liquid and gas at low temperature and low pressure. The refrigerant enters the evaporator (Evap), which is in the form of a coil in contact with the cold source that cools the misting solution. In the evaporator, the fluid absorbs heat from this cold source, causing it to evaporate. The refrigerant then returns to its gaseous state, ready to be recompressed by the compressor, and the cycle begins again [8].

The cold source inside the cooler is a 30 liters mixture of water and glycol (illustrated in blue). A regulator controls the cooler to maintain this liquid at a set temperature which is determined using a potentiometer.

The circuit of the misting is illustrated in black. The solution is pumped from the reservoir tanks (illustrated in grey) by a pump (P) and passes through filters (F1 and F2) to evacuate some impurities. Then, the solution can go in 2 different pipes. The circulation is determined by an electrovalve in each pipe.

The first circuit, almost the same as in the initial setup (Figure 3.2), deliver the solution to the misting nozzles. The circuit is divided in two for a better distribution in the pipes inside the chamber (illustrated in green). There are 28 misting nozzles spread all over the soil of the chamber. When the first electrovalve (EV1) is opened (10 seconds every 3 minutes), the pressure rises in the misting bars and the water comes out through the nozzles. This is a misting episode.
The misting water that percolates down the walls and the roots falls to the bottom of the chamber. The floor slopes slightly towards the two water tanks and has two collectors at its lowest point, which in turn are connected to the tanks. Excess water therefore ends up in the water tanks.

The second circuit permits to cool the misting water. When the second electrovalve (EV2) is opened (20 seconds every 60 seconds), the pressure drops (since the pump simply sends the water through a circuit of 20 diameter tubes, open at the end) below a threshold below which the nozzles no longer let any water through. The circuit is then simply a cooling circuit for the whole system (pipes, pump body and tanks).

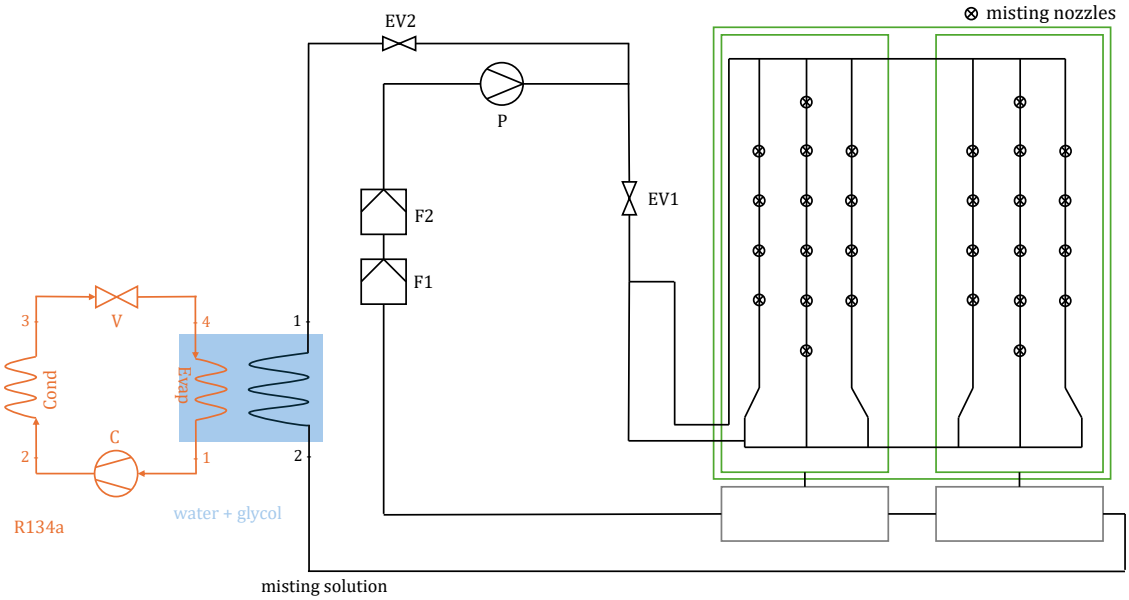

Figure 6.1: Scheme of the misting and cooling circuits

6.3 Measurements

The sensors are placed at the same positions as in Figure 3.4, except for the sensor s08 which is moved inside the cooler where it measures the temperature of the glycol-water mixture. The sensor s07 takes the previous place of sensor s08 measuring the temperature of the misting water. Measurements are taken between 4 p.m. on June 13, 2024 and 3:49 a.m. on June 15, 2024 and are reported on Figure 6.2.

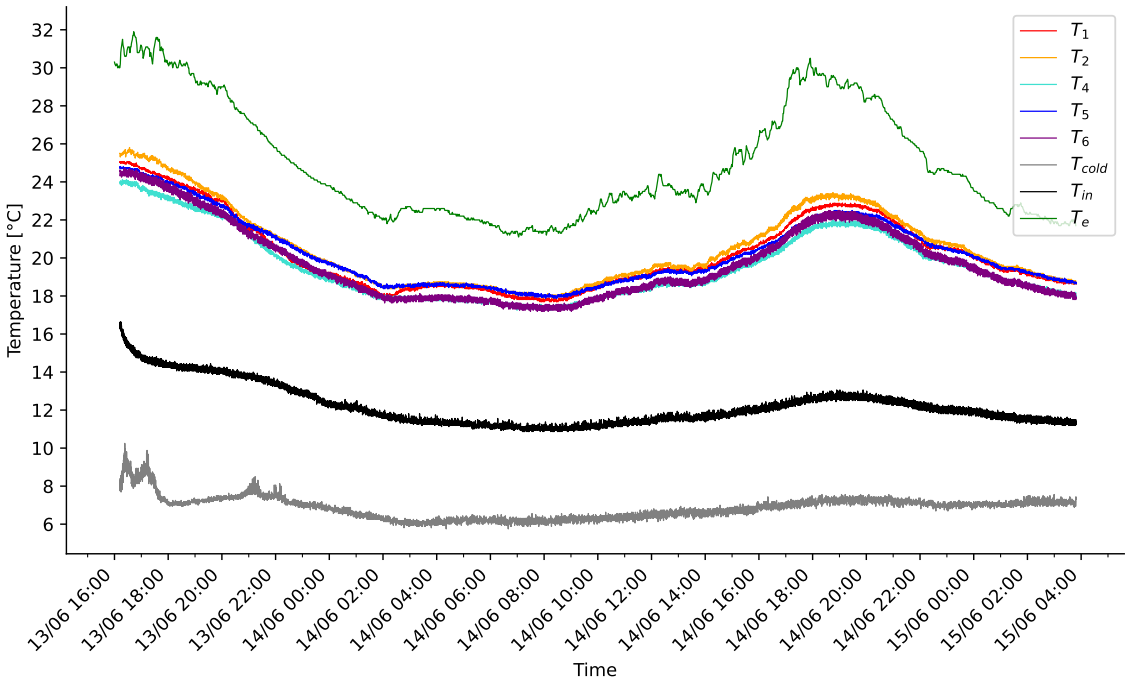

Figure 6.2: Temperatures measured during the cooling test

The temperature inside the chamber is still approximated by the mean of the temperatures measured by the five sensors inside the chamber with (4.1) and can be seen on Figure 6.3. When talking about T, it signifies T_{mean}.

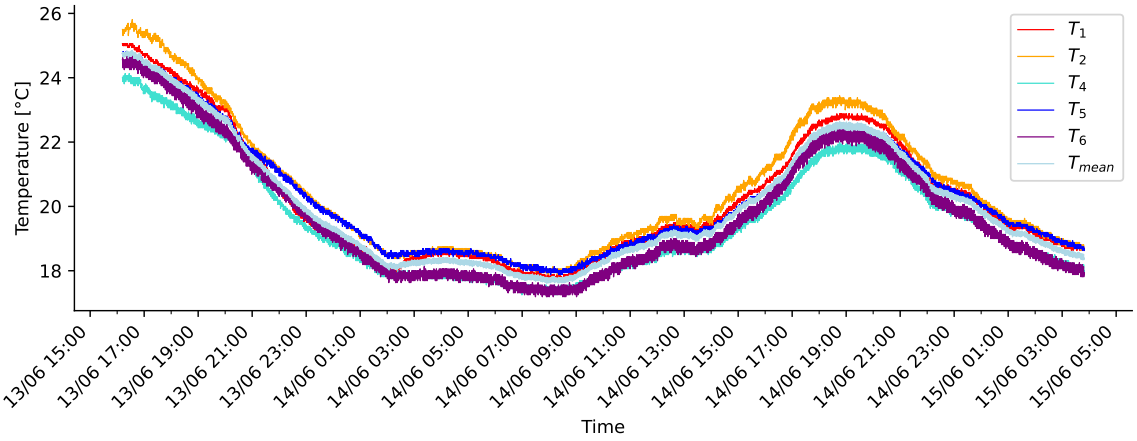

Figure 6.3: Temperatures measured by the five sensors inside the chamber and the mean of them during the cooling test

On Figure 6.4, it can be observed that the temperature of the mixture of glycol and water T_{cold} becomes nearly constant from 6 p.m on June 13. All the further analysis of the experiment with cooled misting is done from this time.

The temperature of the glycol-water mixture varies between 5.75 °C and 8.5 °C with a mean value of 6.78 °C, making the misting water varies between 10.87°C and 14.56°C with a mean value of 12.08°C.
The temperature inside the chamber varies between 17.61°C and 24.01°C with a mean value of 19.85°C, while the temperature of the greenhouse varies between 21.1°C and 30.5°C with a mean value of 24.59°C.

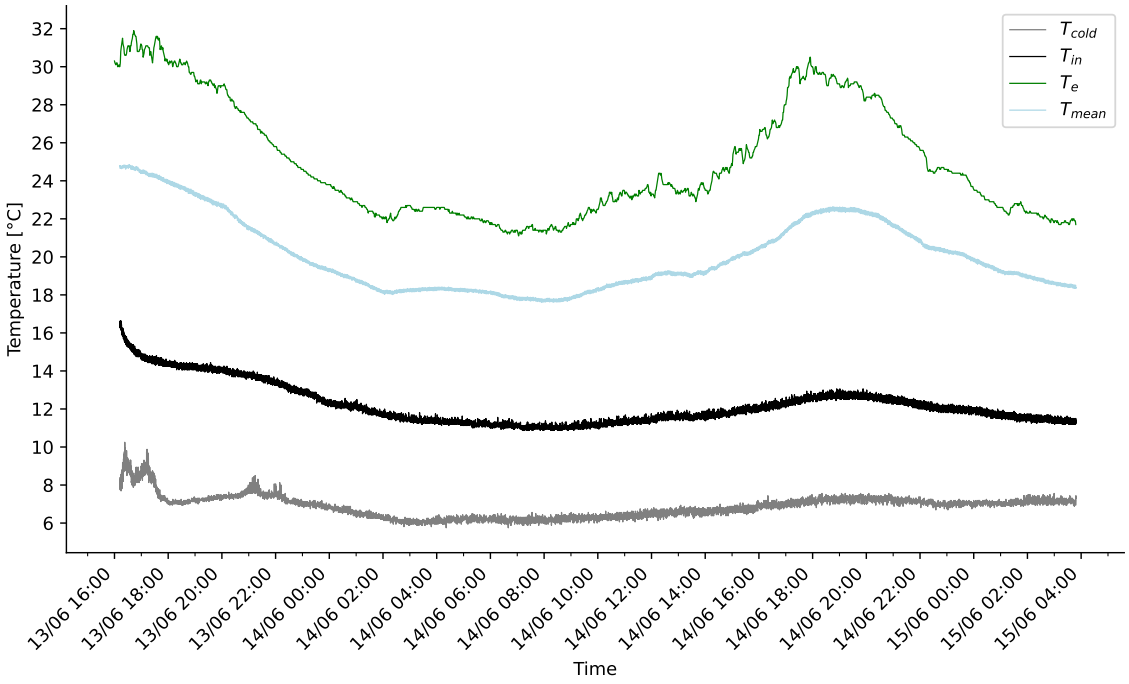

Figure 6.4: Temperatures measured during the cooling test with the mean of the temperatures inside the chamber

The situation with and without the cooling system can be compared on Figures 6.5 and 6.6. The temperature of the misted water when there is no cooling ($T_{in,simulated}$ without cooling) is approximated to be at a constant temperature of 19.5 °C (as was seen in Section 3.3.2). From this curve and the temperature of the greenhouse measured during the cooling test ($T_{e,measured}$), the temperature of the chamber without cooling ($T_{simulated}$ without cooling) is simulated by the model (4.2).
To compare equivalent curves, the temperature of the chamber during the cooling test ($T_{simulated}$ with cooling) is also simulated by the model from the temperature

of the misted water measured during the cooling test ($T_{in,measured}$ with cooling) and $T_{e,measured}$.
This also allows to see how well $T_{simulated}$ with cooling approximate the temperature of the chamber measured during the cooling test ($T_{measured}$ with cooling).
It can be concluded that the cooler permits indeed to cool the misting water which permits to regulate the temperature of the chamber.

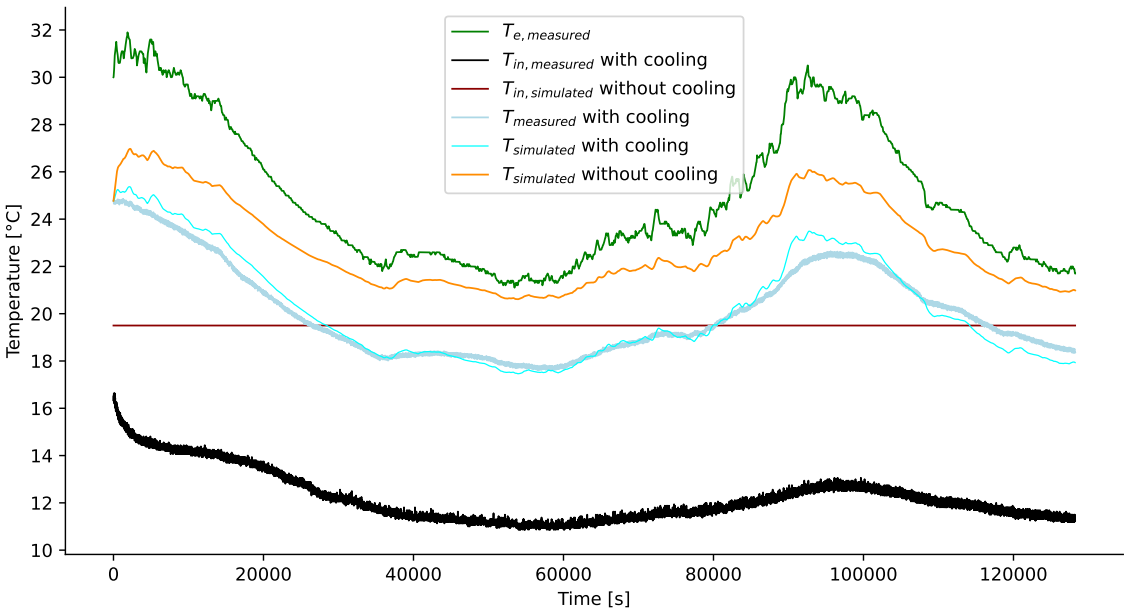

Figure 6.5: Comparison between temperatures measured during the cooling test and temperatures simulated if there is no cooling with $\dot{m} = 3.83\frac{kg}{s}$ and $\alpha = 26.754\frac{kJ}{sK}$

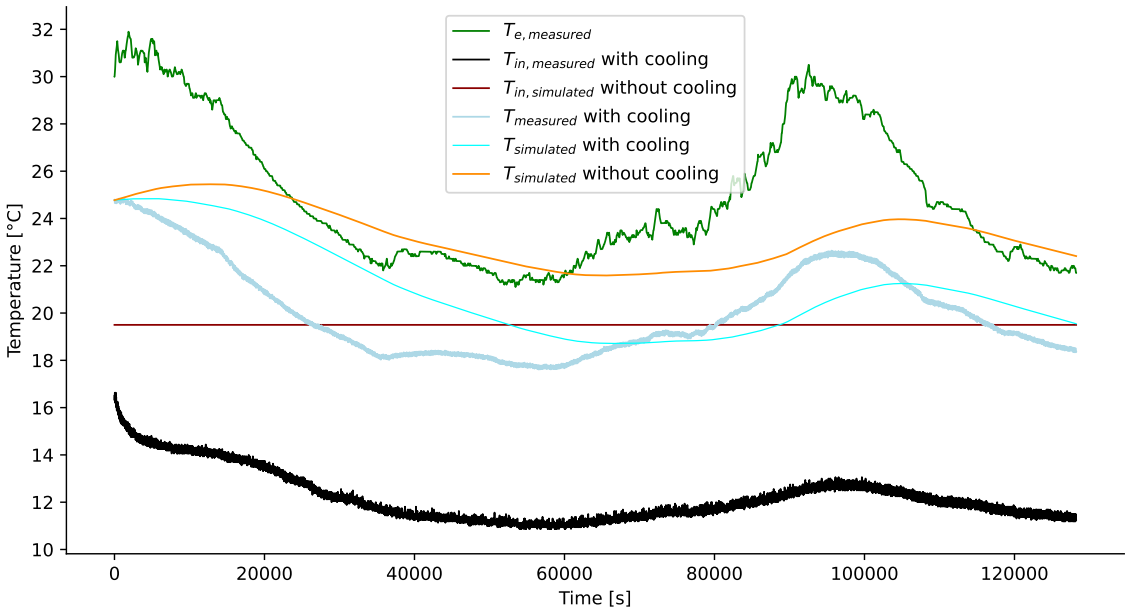

Figure 6.6: Comparison between temperatures measured during the cooling test and temperatures simulated if there is no cooling with $\dot{m} = 0.0881\frac{kg}{s}$ and $\alpha = 0.615\frac{kJ}{sK}$

An improvement of the solution could be to start and stop the cooling system at certain times. It is not necessary to use the cooler continuously. A device could open or close the electrovalve EV2 to allow or not the circulation towards the cooler. It is noticed that the cooler is only useful when the temperature of the greenhouse is above a certain limit.

As was said in Section 5.4, the temperature of the chamber has to be $15°C \leq T \leq 25°C$ to avoid the risk of damaging the plant roots. From the measurements during the test cooling (6.3), it is known that when the glycol-water mixture has a mean temperature of 6.78 °C in the cooler, the misted water has a mean temperature of $T_{in} = 12.08°C$.
To respect the lower bound of T, from (4.2) with $\dot{T} = 0$:

$$\begin{aligned} T_e &\geq \rho_w c_{p,w} V\dot{T} + \frac{\dot{m}c_{p,w}}{\alpha}(\beta T - T_{in}) + T \\ &\geq 16.75°C \end{aligned}$$

When T_e is below 16.75°C, the cooler needs to be stopped or the greenhouse has to be warmed.

To respect the upper bound of T, from (4.2) with $\dot{T} = 0$:

$$\begin{aligned} T_e &\leq \rho_w c_{p,w} V\dot{T} + \frac{\dot{m}c_{p,w}}{\alpha}(\beta T - T_{in}) + T \\ &\leq 32.75°C \end{aligned}$$

When T_e is above 32.75°C, the cooler is not sufficient.

When the misting solution is not cooled, its temperature is around $T_{in} = 19.5°C$ (see Section 3.3.2).
To respect the lower bound of T ($T \geq 15°C$), also from (4.2) with $\dot{T} = 0$:

$$\begin{aligned} T_e &\geq \rho_w c_{p,w} V\dot{T} + \frac{\dot{m}c_{p,w}}{\alpha}(\beta T - T_{in}) + T \\ &\geq 12.12°C \end{aligned}$$

When T_e is below 12.12 °C, the greenhouse or the misting solution has to be warmed to increase respectively T_e or T_{in}, so that T stays above the limit of $15°C$. The greenhouse can be warmed with the system already integrated in the greenhouse as was used in experiment 1 (3.3.2). Controlling this temperature can make it not necessary to use the cooler.
To respect the upper bound of T ($T \leq 25°C$):

$$\begin{aligned} T_e &\leq \rho_w c_{p,w} V\dot{T} + \frac{\dot{m}c_{p,w}}{\alpha}(\beta T - T_{in}) + T \\ &\leq 28.12°C \end{aligned}$$

When T_e is above 28.12 °C, the misting solution has to be cooled because the greenhouse is hardly cooled.
In conlusion, when $12.12°C \leq T_e \leq 28.12°C$, the electrolve EV2 can be closed and the temperature of the chamber fluctuates between 15°C and 25°C.

The results are independent of the choice of $\dot{m}$ and α because their ratio $\frac{\dot{m}}{\alpha}$ is equivalent:

$$\frac{3.83}{26.754} = 0.143 = \frac{0.0881}{0.615}$$

All the possible scenarios and the way of reacting to them to keep $15°C \leq T \leq 25°C$ are summarized in Table 6.1 and explained here:

- If $T_e < 12.12°C \Rightarrow$ The greenhouse or the misted solution has to be warmed to increase respectively T_e or T_{in}: $T_e > 12.12°C$ or $T_{in} > 19.5°C$.

- If $12.12°C \leq T_e < 16.75°C \Rightarrow$ The misted solution has to be kept at its default temperature: $T_{in} = 19.5°C$.
- If $16.75°C \leq T_e \leq 28.12°C \Rightarrow$ The misted solution can be either at its default temperature or be cooled: $T_{in} = 19.5°C$ or $T_{in} = 12.08°C$.
- If $28.12°C < T_e \leq 32.75°C \Rightarrow$ The misted solution has to be cooled: $T_{in} = 12.08°C$.
- $T_e > 32.75°C \Rightarrow$ Neither the temperature of the misted solution or of the greenhouse can be controlled so the temperature of the chamber exceeds the recommended value: $T > 25°C$.

	T_e	T_{in}	$15°C < T < 25°C$
$T_e < 12.12°C$	$> 12.12°C$	$> 19.5°C$	✓
$12.12°C \leq T_e < 16.75°C$		$19.5°C$	✓
$16.75°C \leq T_e \leq 28.12°C$		$19.5°C$ or $12.08°C$	✓
$28.12°C < T_e \leq 32.75°C$		$12.08°C$	✓
$T_e > 32.75°C$			✗

Table 6.1: Scenarios and the way of reacting to them to keep $15°C \leq T \leq 25°C$

Chapter 7

Conclusion

The initial problematic of this master thesis was to develop a dynamical model based on energy balance in the RootPhAir platform, and to design and implement a control strategy based on this model in order to control the temperature inside the chamber in spite of variations of the greenhouse temperature.

Temperature measurements of the greenhouse, of the misted solution and of the chamber have been done. These were preprocessed to render them in a noise-free form with a constant time step. They were then used to elaborate the equation governing the heat balance in the experimental set-up. In fact, the unknown parameters of the model were determined by analyzing of the dynamic response of the system and by performing linear regressions. Afterwards, the mass flow rate, that was considered unknown so far, was measured and the identification of the other unknown parameters was done by performing linear regressions again. Through all these developments, multiple sets of parameters were found and the best for each of the two mass flow rates was selected. Next, the design of the PI controller was made and it was simulated for the two values of mass flow rate. Instead of this regulation, it was decided to mist the solution at a constant temperature. The approach was implemented in practice with a cooler. Measurements were made in this evolved setup to verify if the objective of regulation was reached.

Despite the fact that the initial idea of using a PI controller could not be used, the final installation of the cooling circuit permits indeed to regulate the misting water. Nevertheless, it is not efficient in all situations.

As introduced in Section 6.3, a probable improvement could be to add a system that controls different devices in function of temperature of the greenhouse. The cooling of the misting water could be activated or deactivated. A system to warm up the misting water could be implemented. For the case where the temperature

exceeds 32.75 °C, a completely new solution could be thought up.

Moreover, the utility of the cooling system could be verified with measurements in practice and not only with a simulation as done in Section 6.3. In fact, there are two aeroponic boxes in the greenhouse. As was done, one is equipped with the cooling system and one not. Sensors to measure the temperature inside each chamber and of the misted solution could be placed at the same locations in both. This would able to compare precisely the use of a cooling system or not because the two installations would be subject to the same temperature of the greenhouse.

Finally, the performance of the cooling system could be analyzed but this would necessitate the placement of more sensors.
Sensors measuring the temperature of the refrigerant at the entrance and the exit of the evaporator and sensors measuring the temperature of the misting solution at the entrance and the exit of the cooler could permit to compute the coefficient of performance of the refrigerant cycle and the efficiencies of the heat exchanges between the glycol-water mixture and misting solution and between the refrigerant and air of the greenhouse. The developments are introduced in Appendix E.

Appendix A

Plan of the chamber

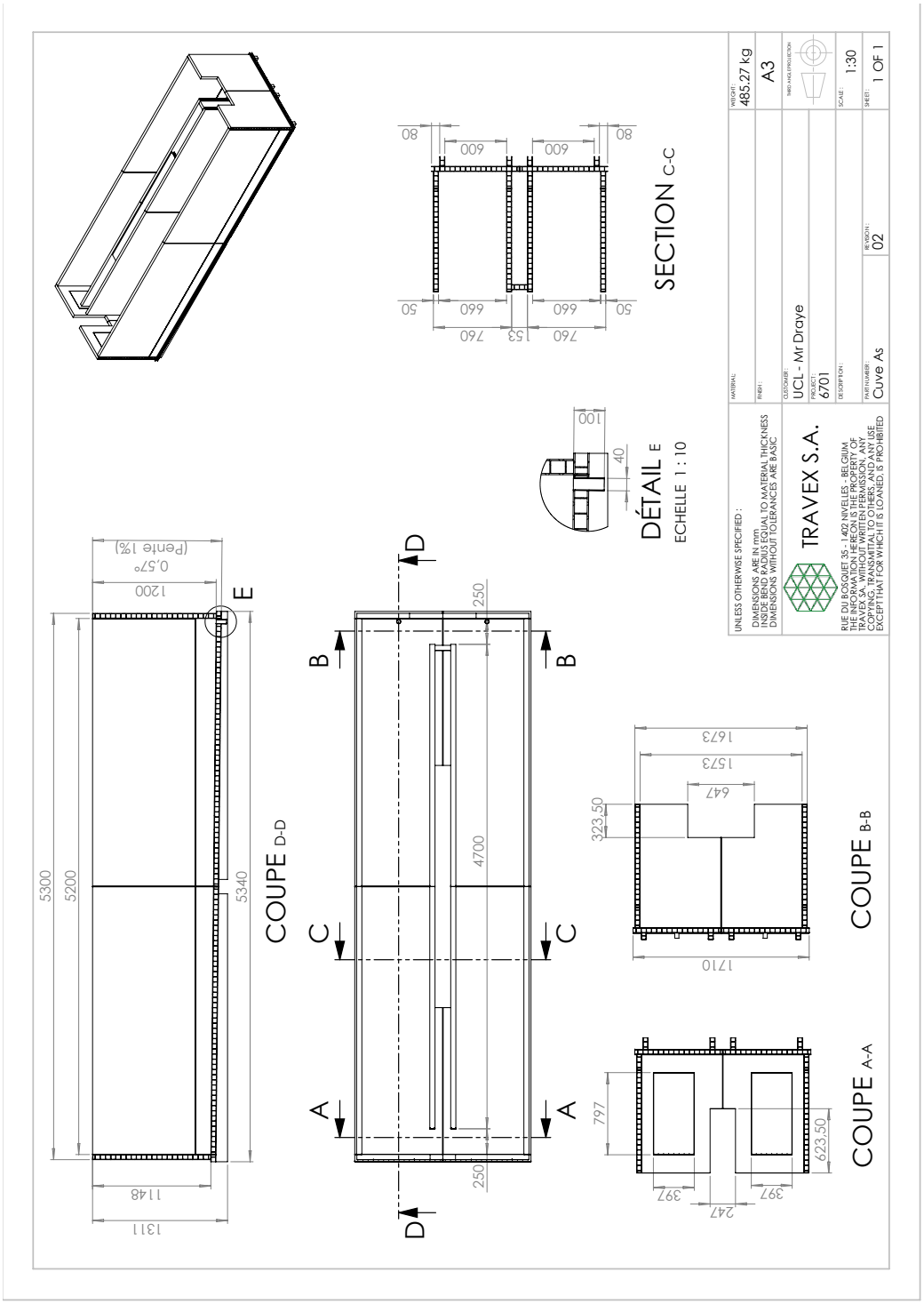

Figure A.1: Plan of the chamber

Appendix B

Results obtained from the step responses

For different values of β varying between 0 and 1, the values of α obtained from each step response of experiments 2b and 3 and their mean are reported in Table B.1, knowing that:

$$\alpha_{mean} = \frac{\alpha_{exp2b} + \alpha_{exp3}}{3}$$
$$\dot{m}_{mean} = \frac{\dot{m}_{exp2b} + \dot{m}_{exp3}}{3}$$

β [−]	α_{exp2b} $\left[\frac{kJ}{sK}\right]$	α_{exp3} $\left[\frac{kJ}{sK}\right]$	α_{mean} $\left[\frac{kJ}{sK}\right]$
0	8.313	10.42	9.367
0.25	5.734	4.986	5.36
0.47	3.464	0.204	1.223
0.5	3.154	-0.448	1.353
0.75	0.575	-5.882	-2.653
1	-2.004	-11.316	-6.66

Table B.1: Values of α for the step responses of experiments 2b and 3 and β between 0 and 1

The values of the mass flow rate $\dot{m}$ are the same regardless of the value of β and are reported in Table B.2.

$\dot{m}_{exp2b}$ $\left[\frac{kg}{s}\right]$	$\dot{m}_{exp3}$ $\left[\frac{kg}{s}\right]$	$\dot{m}_{mean}$ $\left[\frac{kg}{s}\right]$
2.465	5.194	3.83

Table B.2: Values of $\dot{m}$ for the step responses of experiments 2b and 3 and their mean

Each set of values is tested (see Section 3.3.2) for each value of β.

B.1 With $\beta = 0$

The simulations using α_{exp2b} and $\dot{m}_{exp2b}$ are on Figure B.1.
The simulations using α_{exp3} and $\dot{m}_{exp3}$ are on Figure B.2.
The simulations using α_{mean} and $\dot{m}_{mean}$ are on Figure B.3.

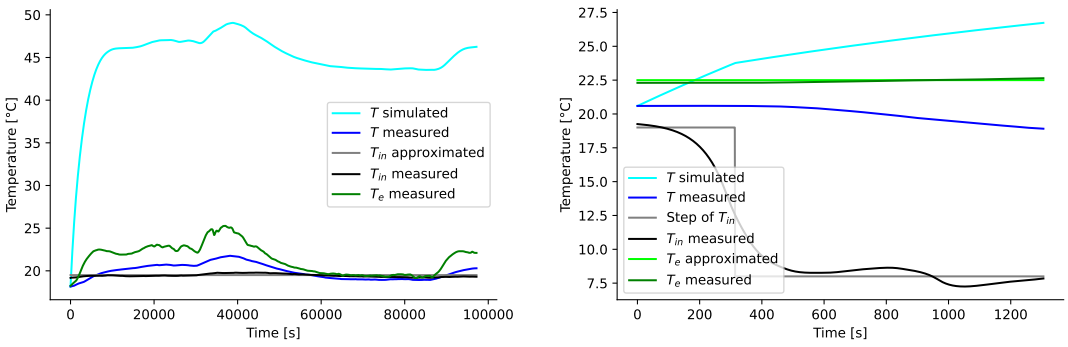

(a) (b)

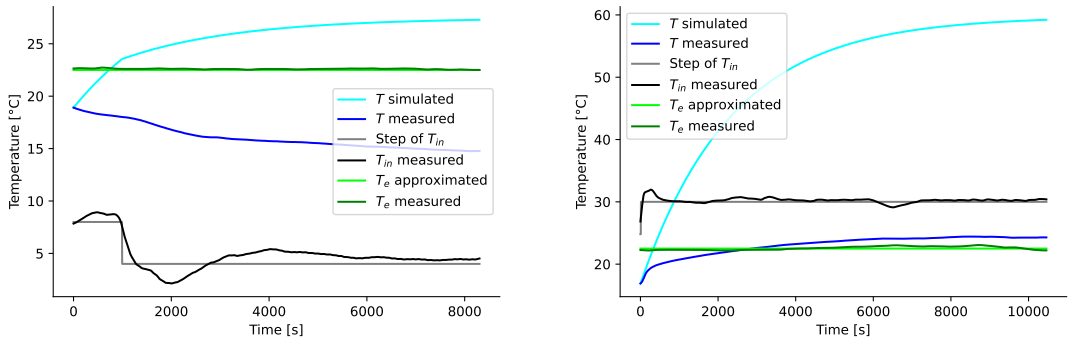

(c) (d)

Figure B.1: Simulation of T during experiments (a) 1, (b) 2a, (c) 2b and (d) 3, using α_{exp2b} and $\dot{m}_{exp2b}$ from the step response of experiment 2a with $\beta = 0$

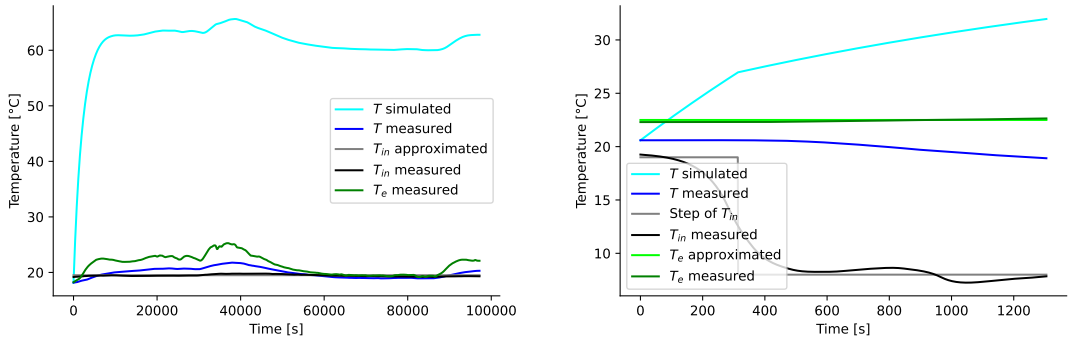

(a) (b)

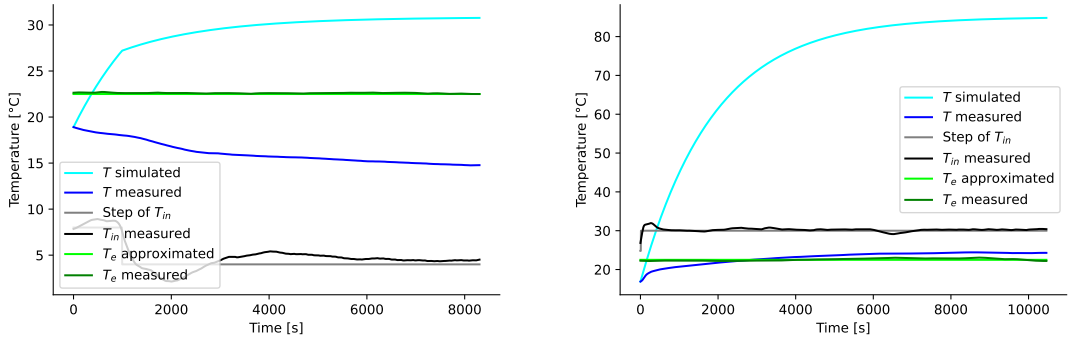

(c) (d)

Figure B.2: Simulation of T during experiments (a) 1, (b) 2a, (c) 2b and (d) 3, using α_{exp3} and $\dot{m}_{exp3}$ from the step response of experiment 2a with $\beta = 0$

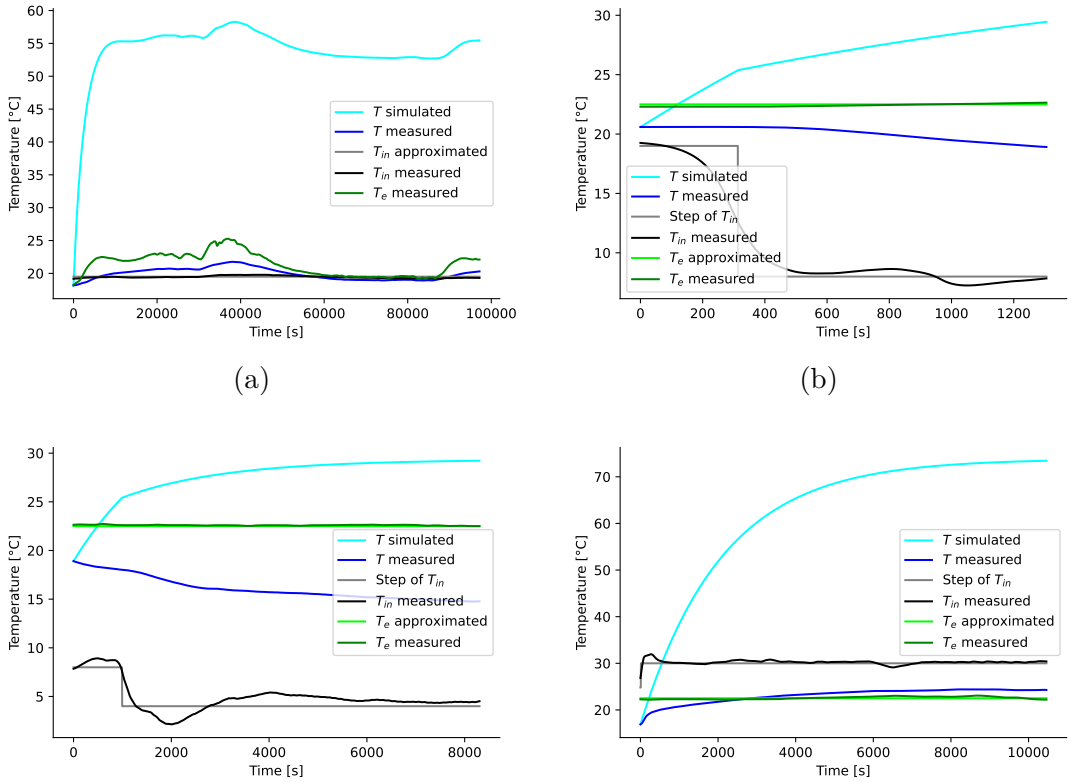

Figure B.3: Simulation of T during experiments (a) 1, (b) 2a, (c) 2b and (d) 3, using α_{mean} and $\dot{m}_{mean}$ from the step responses with $\beta = 0$

B.2 With $\beta = 0.25$

The simulations using α_{exp2b} and $\dot{m}_{exp2b}$ are on Figure B.4.
The simulations using α_{exp3} and $\dot{m}_{exp3}$ are on Figure B.5.
The simulations using α_{mean} and $\dot{m}_{mean}$ are on Figure B.6.

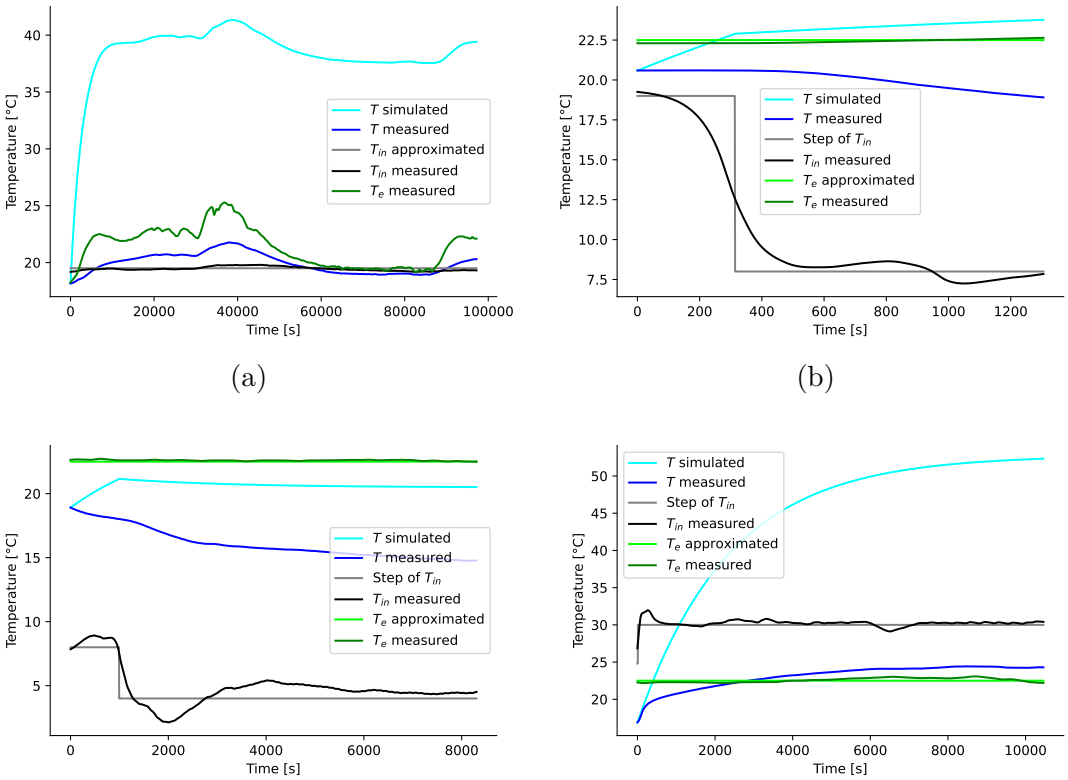

Figure B.4: Simulation of T during experiments (a) 1, (b) 2a, (c) 2b and (d) 3, using α_{exp2a} and $\dot{m}_{exp2a}$ from the step response of experiment 2b with $\beta = 0.25$

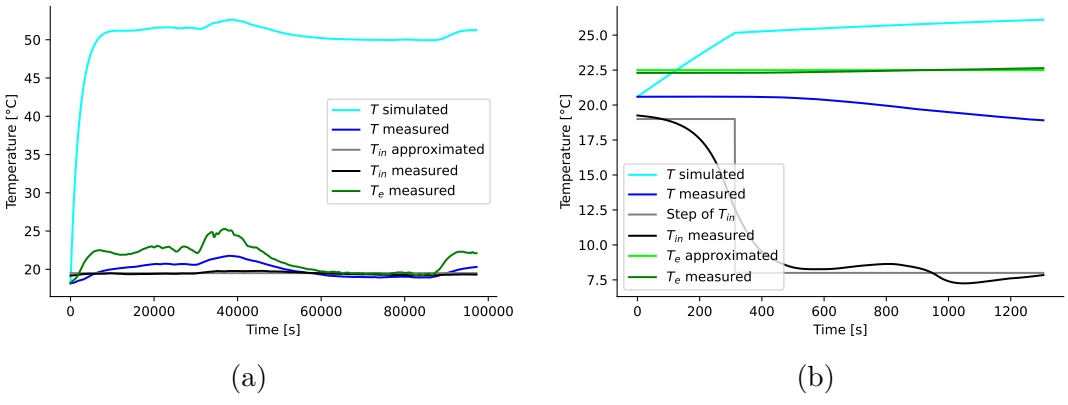

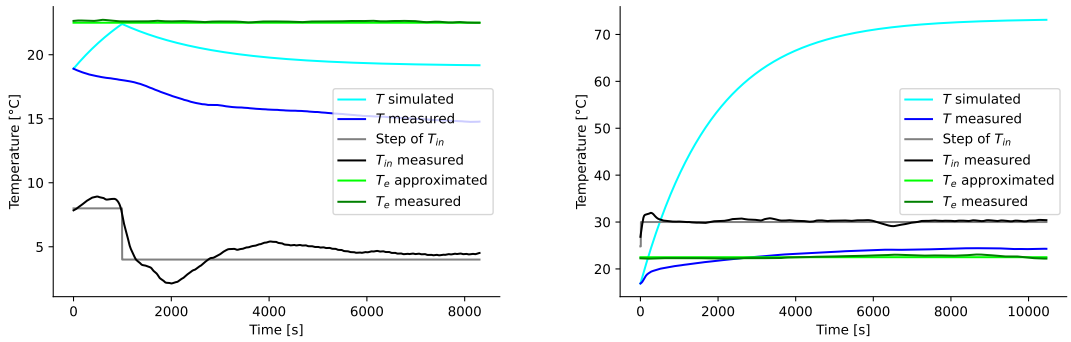

(c) (d)

Figure B.5: Simulation of T during experiments (a) 1, (b) 2a, (c) 2b and (d) 3, using α_{exp3} and $\dot{m}_{exp3}$ from the step response of experiment 2a with $\beta = 0.25$

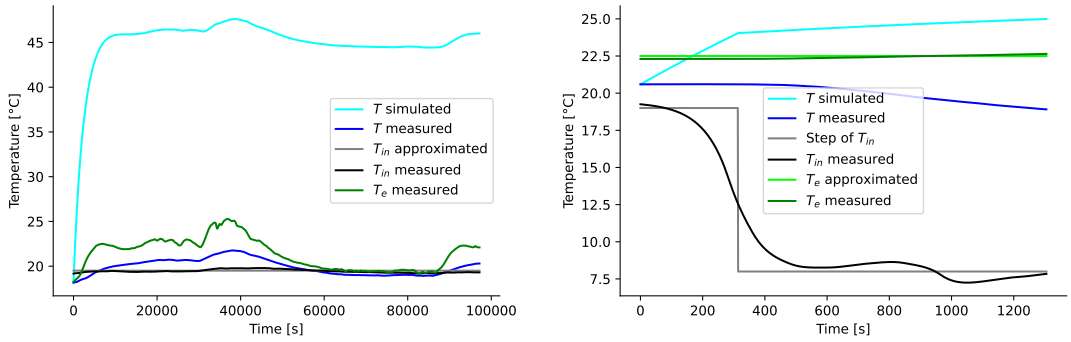

(a) (b)

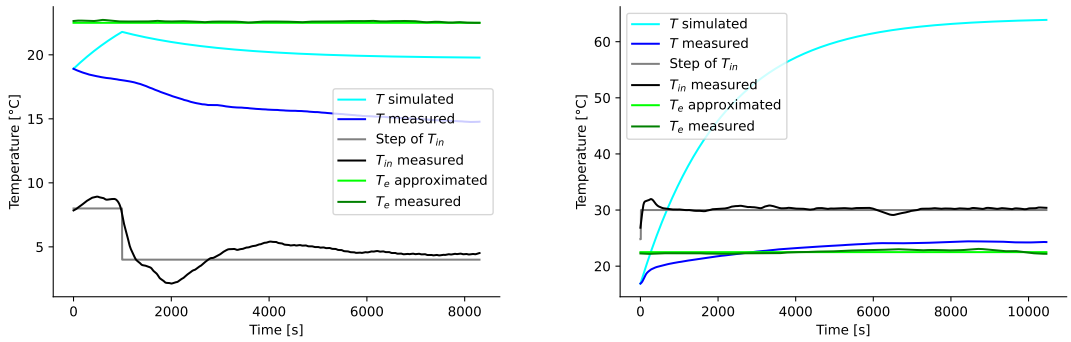

(c) (d)

Figure B.6: Simulation of T during experiments (a) 1, (b) 2a, (c) 2b and (d) 3, using α_{mean} and $\dot{m}_{mean}$ from the step responses with $\beta = 0.25$

B.3 With $\beta = 0.5$

The simulations using α_{exp2b} and $\dot{m}_{exp2b}$ are on Figure B.7.
The simulations using α_{exp3} and $\dot{m}_{exp3}$ are on Figure B.8.
The simulations using α_{mean} and $\dot{m}_{mean}$ are on Figure B.9.

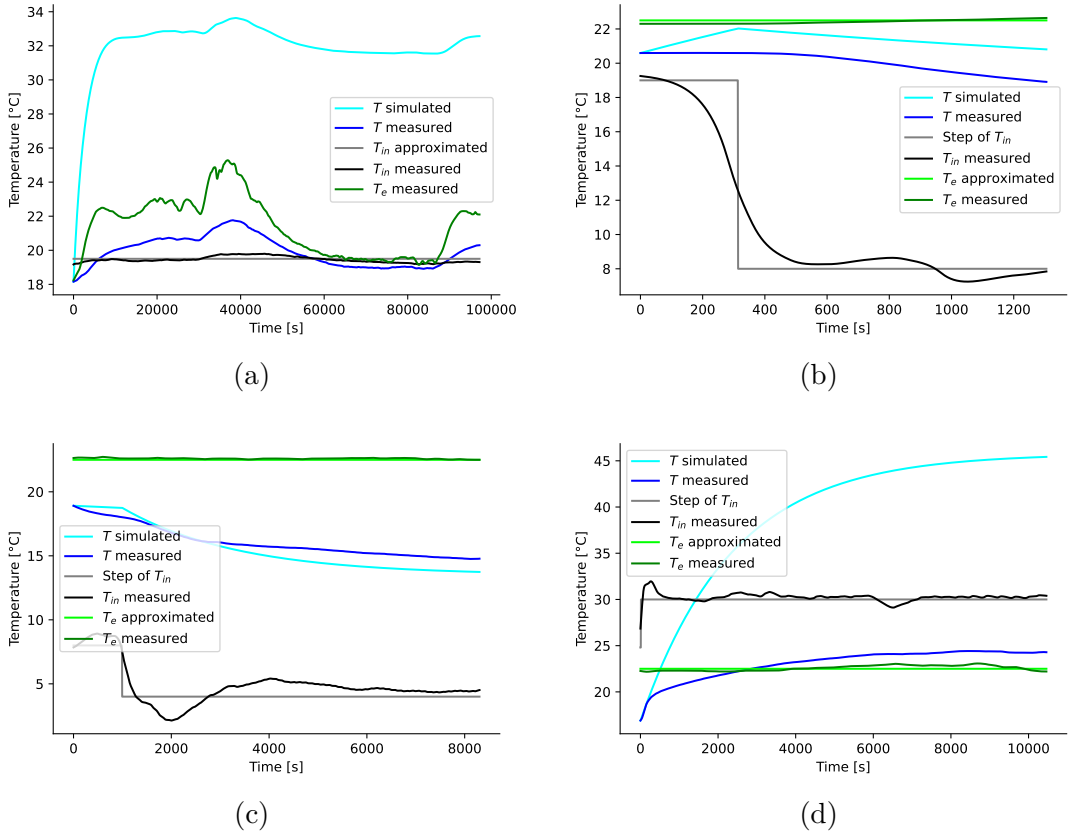

Figure B.7: Simulation of T during experiments (a) 1, (b) 2a, (c) 2b and (d) 3, using α_{exp2b} and $\dot{m}_{exp2b}$ from the step response of experiment 2b with $\beta = 0.5$

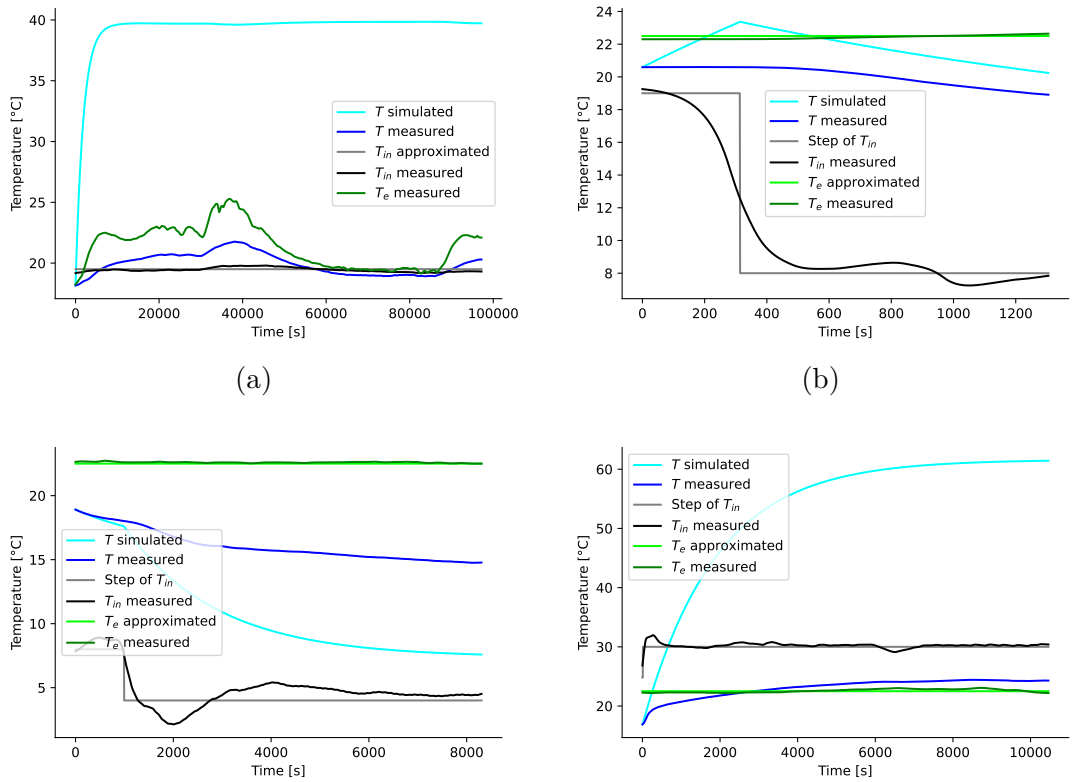

Figure B.8: Simulation of T during experiments (a) 1, (b) 2a, (c) 2b and (d) 3, using α_{exp3} and $\dot{m}_{exp3}$ from the step response of experiment 3 with $\beta = 0.5$

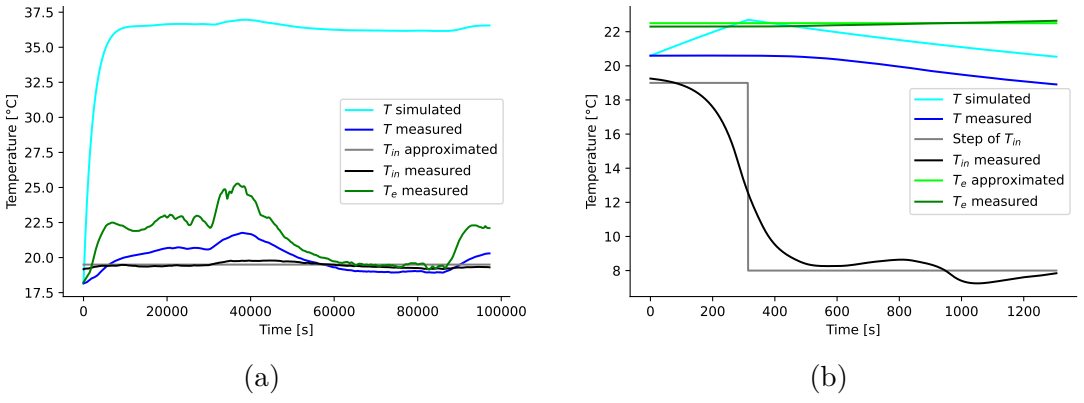

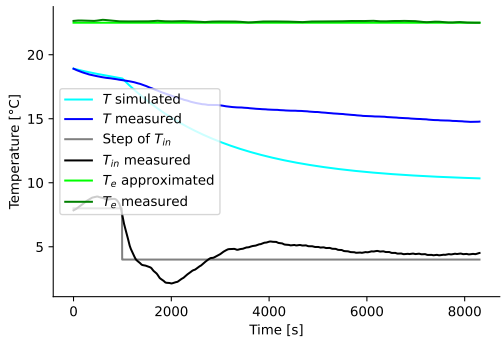

(c)

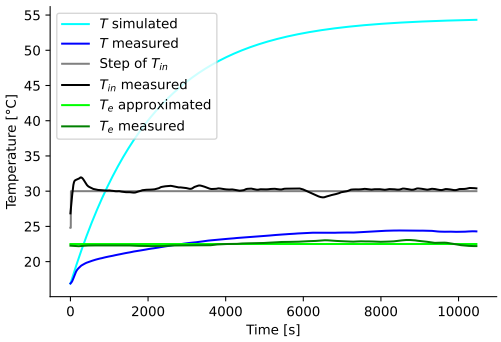

(d)

Figure B.9: Simulation of T during experiments (a) 1, (b) 2a, (c) 2b and (d) 3, using α_{mean} and $\dot{m}_{mean}$ from the step responses with $\beta = 0.5$

B.4 With $\beta = 0.75$

The simulations using α_{exp2b} and $\dot{m}_{exp2b}$ are on Figure B.10.
The simulations using α_{exp3} and $\dot{m}_{exp3}$ are on Figure B.11.
The simulations using α_{mean} and $\dot{m}_{mean}$ are on Figure B.12.

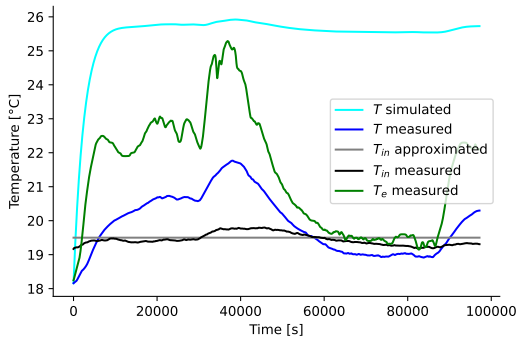

(a)

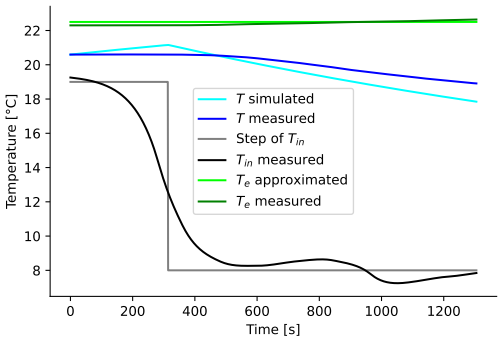

(b)

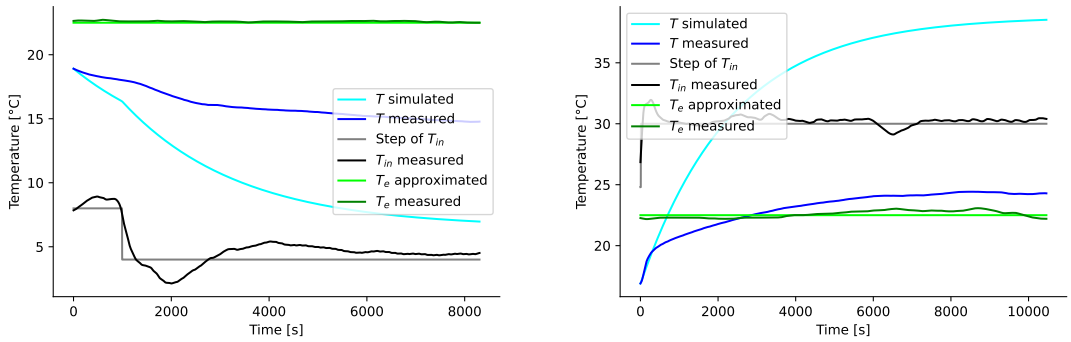

(c) (d)

Figure B.10: Simulation of T during experiments (a) 1, (b) 2a, (c) 2b and (d) 3, using α_{exp2b} and $\dot{m}_{exp2b}$ from the step response of experiment 2b with $\beta = 0.75$

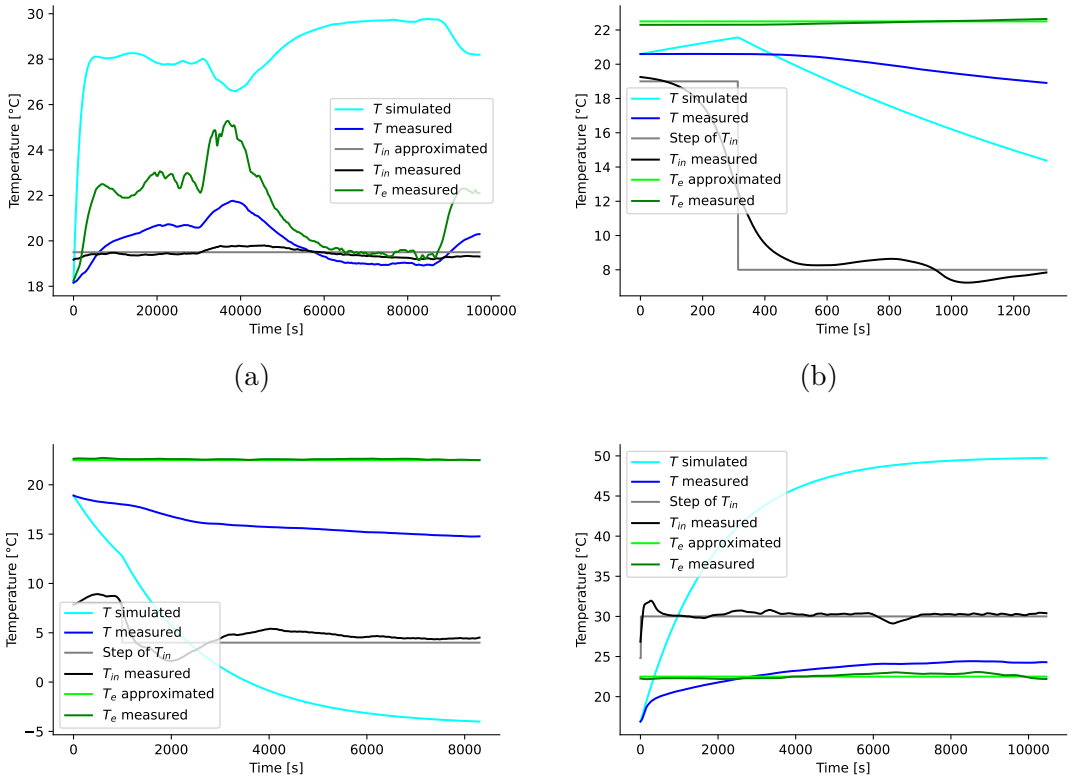

(a) (b)

(c) (d)

Figure B.11: Simulation of T during experiments (a) 1, (b) 2a, (c) 2b and (d) 3, using α_{exp3} and $\dot{m}_{exp3}$ from the step response of experiment 3 with $\beta = 0.75$

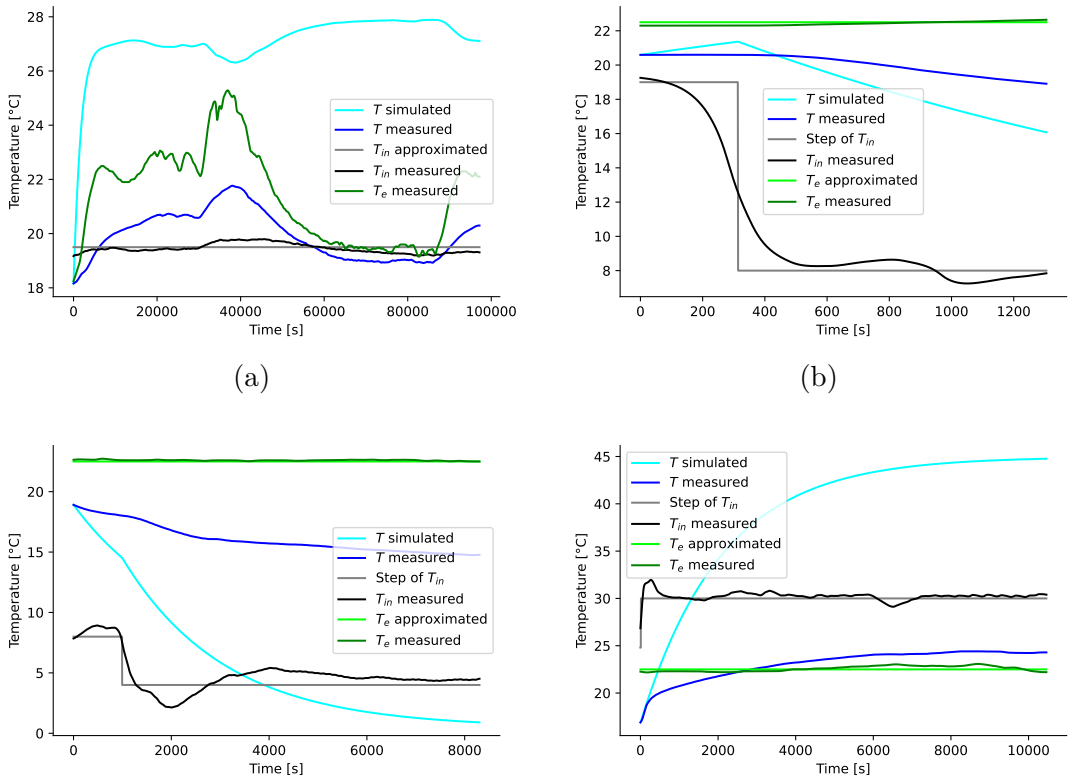

Figure B.12: Simulation of T during experiments (a) 1, (b) 2a, (c) 2b and (d) 3, using α_{mean} and $\dot{m}_{mean}$ from the step responses with $\beta = 0.75$

B.5 With $\beta = 1$

The simulations using α_{exp2b} and $\dot{m}_{exp2b}$ are on Figure B.13.
The simulations using α_{exp3} and $\dot{m}_{exp3}$ are on Figure B.14.
The simulations using α_{mean} and $\dot{m}_{mean}$ are on Figure B.15.

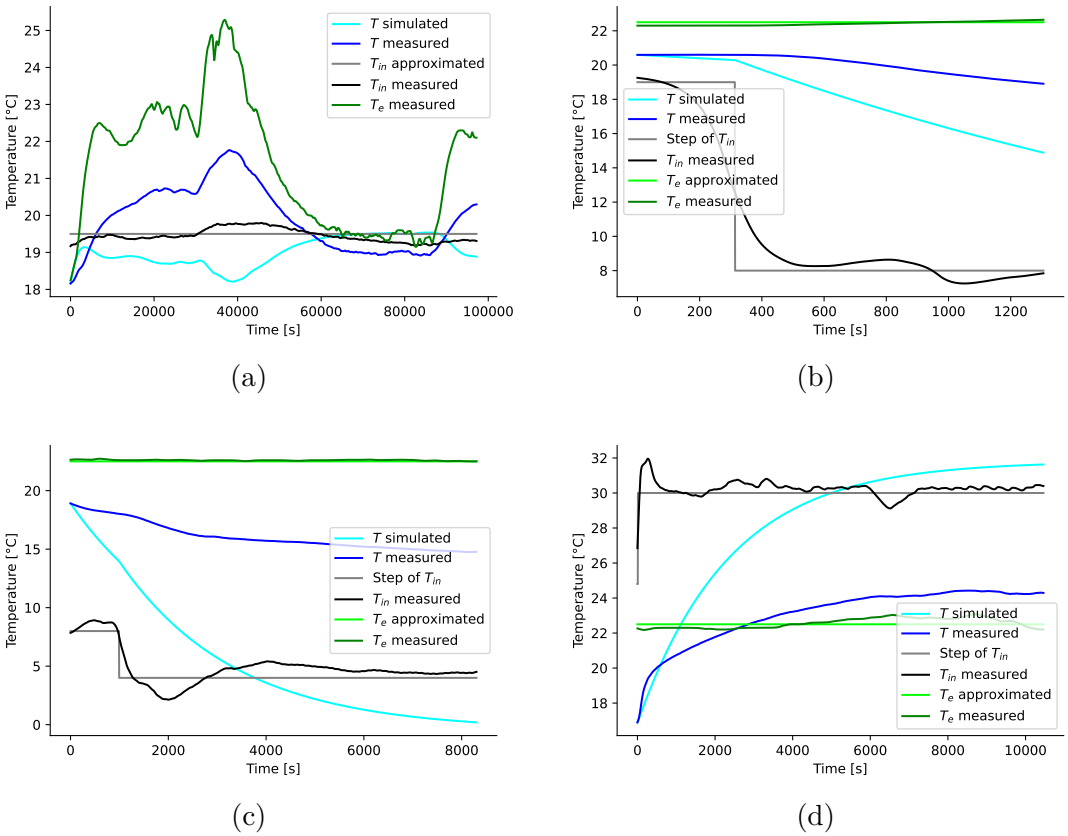

Figure B.13: Simulation of T during experiments (a) 1, (b) 2a, (c) 2b and (d) 3, using α_{exp2b} and $\dot{m}_{exp2b}$ from the step response of experiment 2b with $\beta = 1$

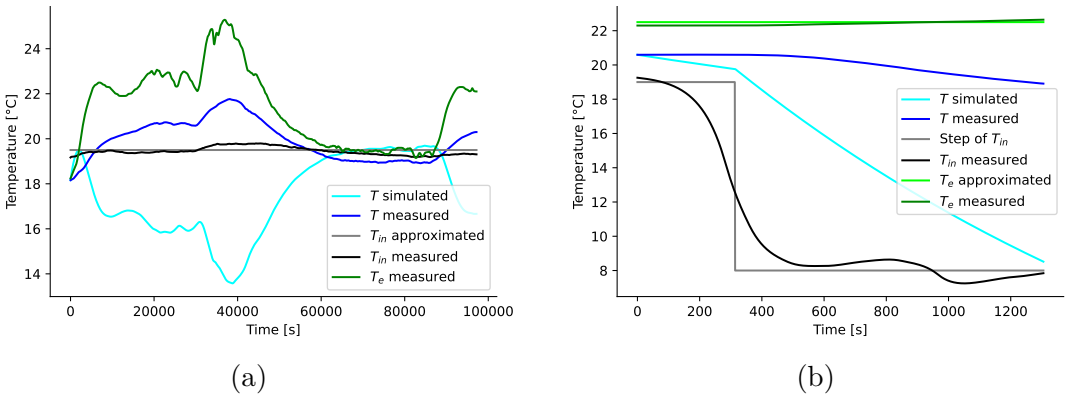

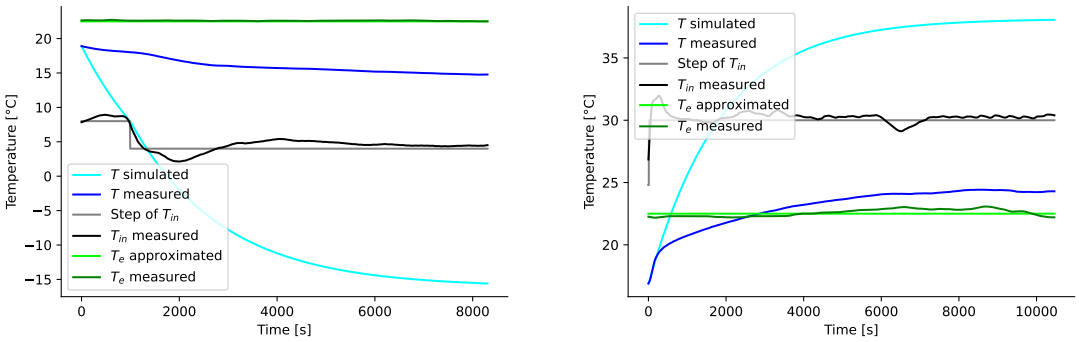

(c) (d)

Figure B.14: Simulation of T during experiments (a) 1, (b) 2a, (c) 2b and (d) 3, using α_{exp3} and $\dot{m}_{exp3}$ from the step response of experiment 3 with $\beta = 1$

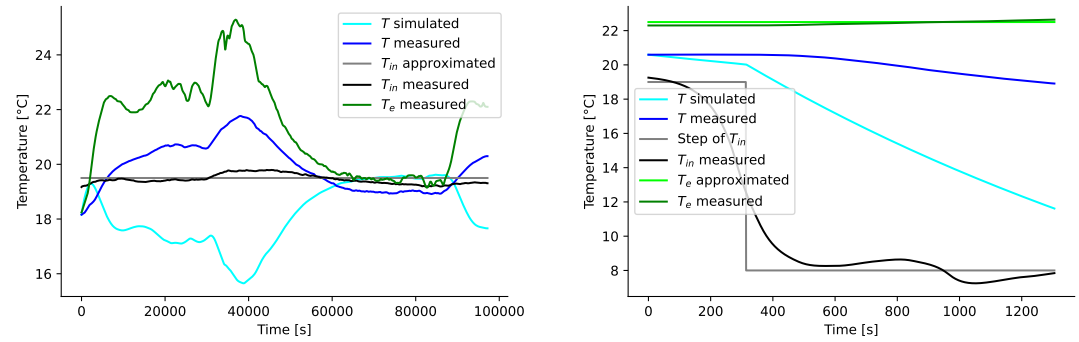

(a) (b)

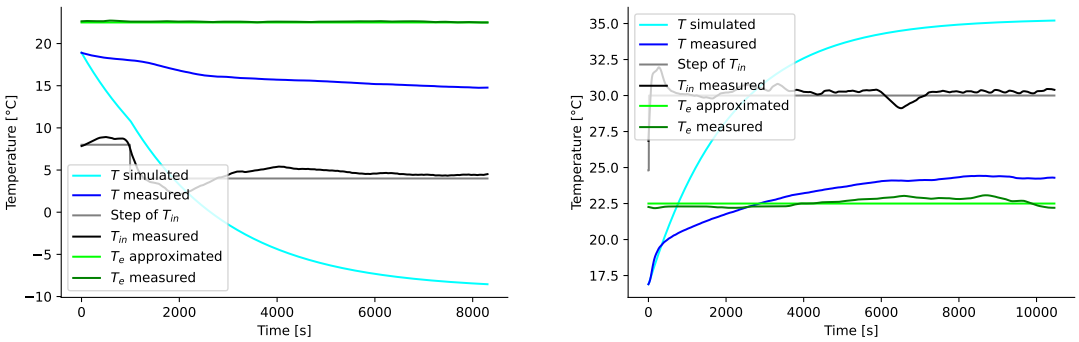

(c) (d)

Figure B.15: Simulation of T during experiments (a) 1, (b) 2a, (c) 2b and (d) 3, using α_{mean} and $\dot{m}_{mean}$ from the step responses with $\beta = 1$

Appendix C

Time derivatives of T not filtered

Calculating $\dot{T}$ when the signal of T is not filtered gives the Figures C.1, C.2 and C.3.

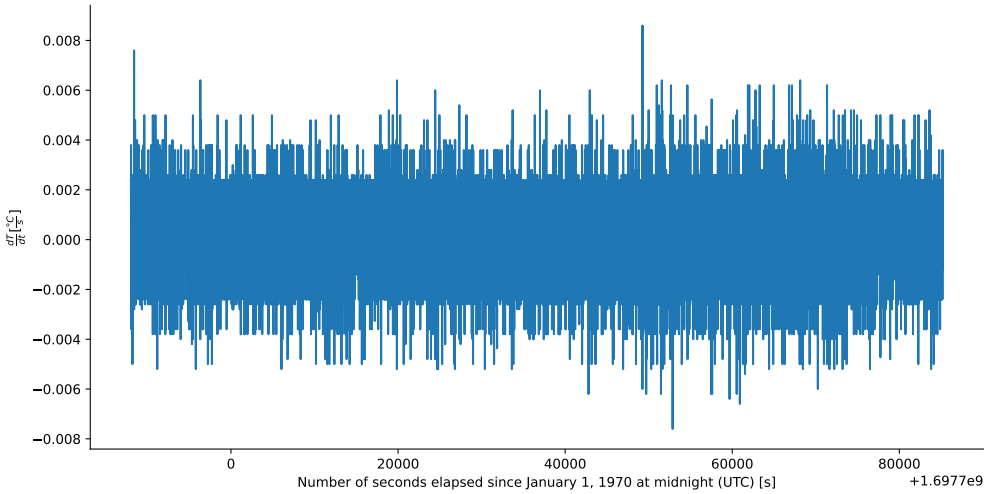

Figure C.1: Time derivative of the mean of the temperatures inside the chamber during experiment 1

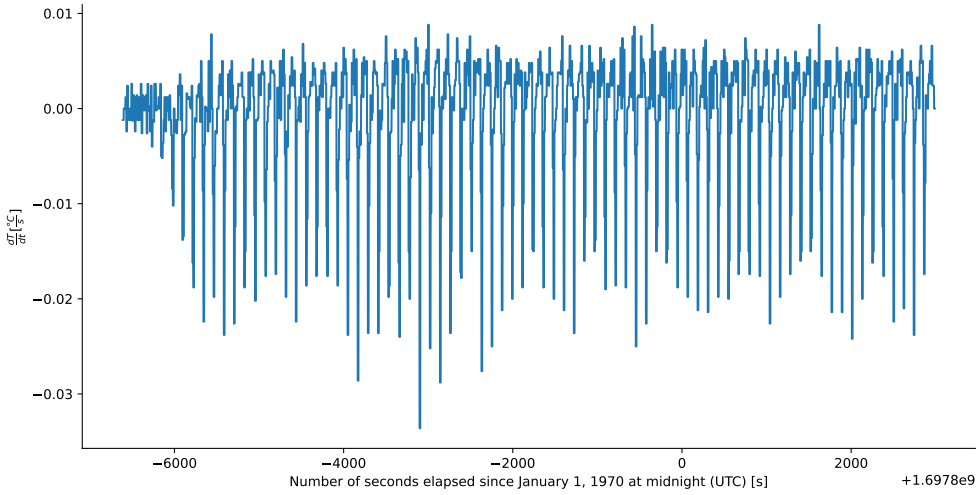

Figure C.2: Time derivative of the mean of the temperatures inside the chamber during experiment 2

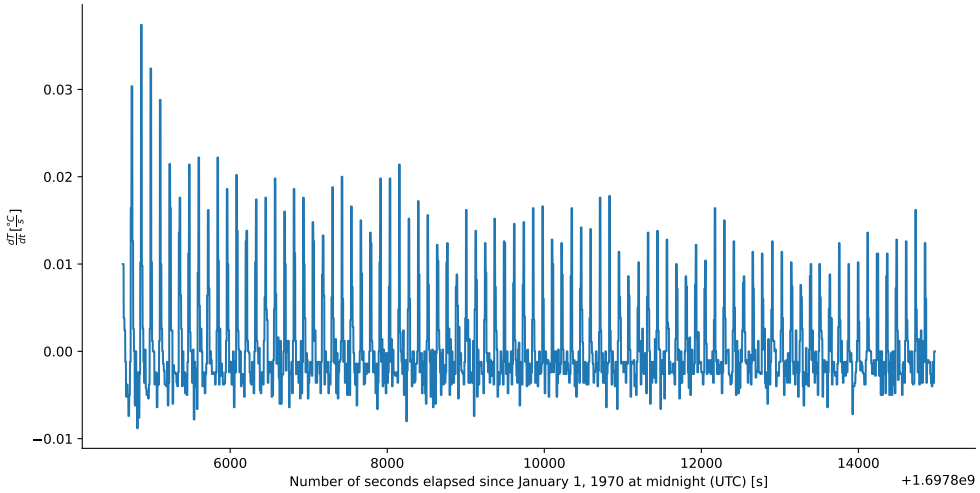

Figure C.3: Time derivative of the mean of the temperatures inside the chamber during experiment 3

Appendix D

Specifications of the cooler

This appendix contains the data sheet of the beer cooler used in the cooling circuit. It was provided by Michel Herman from the company Antoine.

BEER COOLER
model «TR – 60»

Name	Unit	Model
		«TR-60»
Voltage	V	220 +10% -15%
Frequency	Hz	50
Power consumption	W	550
Number of coils (material - stainless steel AISI 304L)	Pcs	3 + 1
Cooler capacity at ΔT = 16 °C	l/h	130
Outlet temperature	°C	2…8
Ice bank	kg	19
Ice forming at water T = 24°C	H	5,5
Water tank capacity (up until the overflow)	l	60
Compressor cooling capacity at T evap. = - 10 °C	W Kcal/ h	620 530
Refrigerant R 134	kg	0,360
Compressor power	h.p.	3/8
Compressor name & serial number	Tecumseh AE 4448 YS	
Fan capacity Power input	m^3/h W	390 33
Agitator - pump: capacity water lifting	 l/h m	 940 12
Pump name and serial number	Totton SPC 42	
Net weight	kg	50
Dimensions (without package): - Width - Length - Height	mm	 450 450 865

Figure D.1: Data sheet of the beer cooler

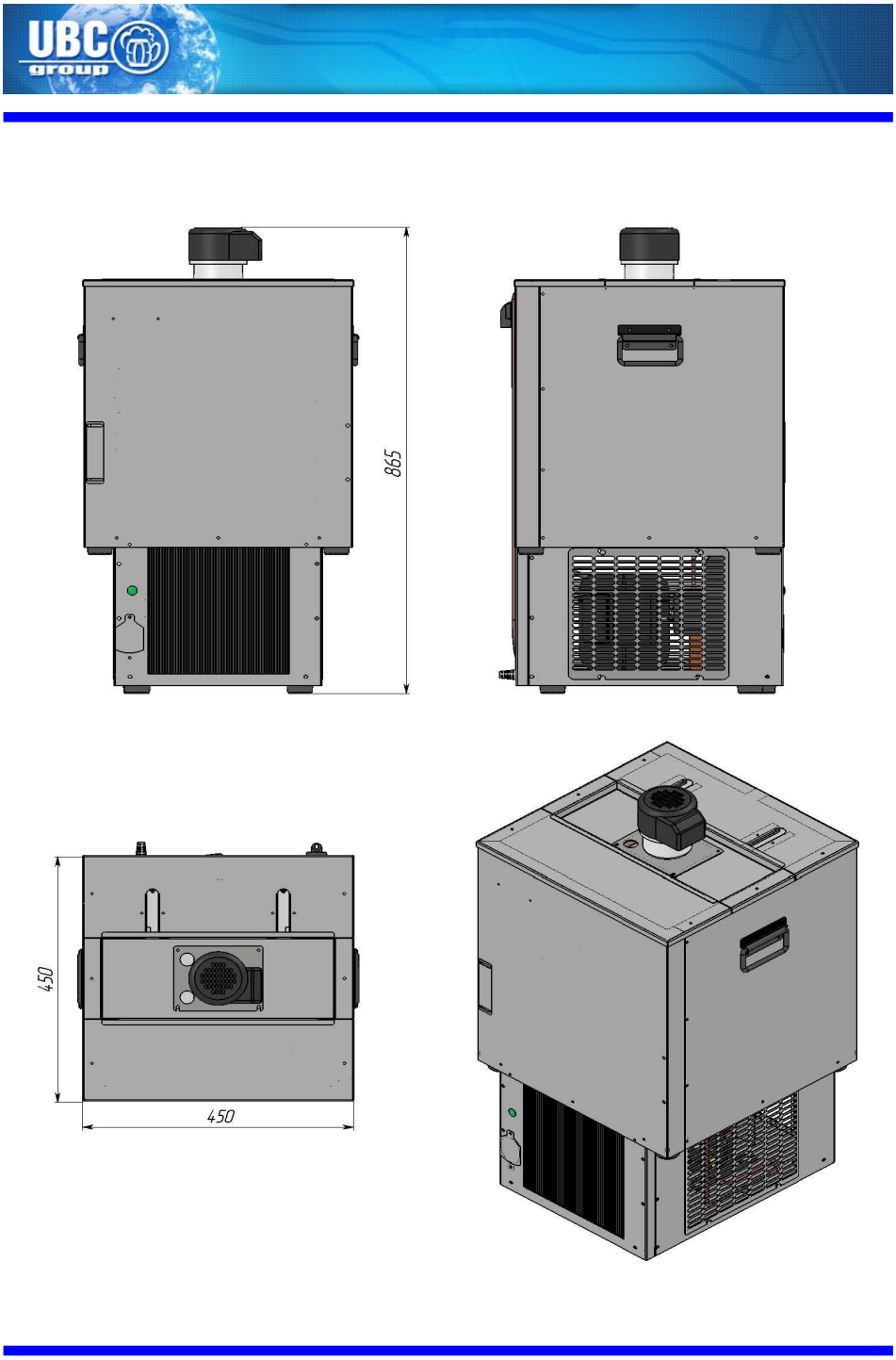

Figure D.2: Data sheet of the beer cooler (cont.)

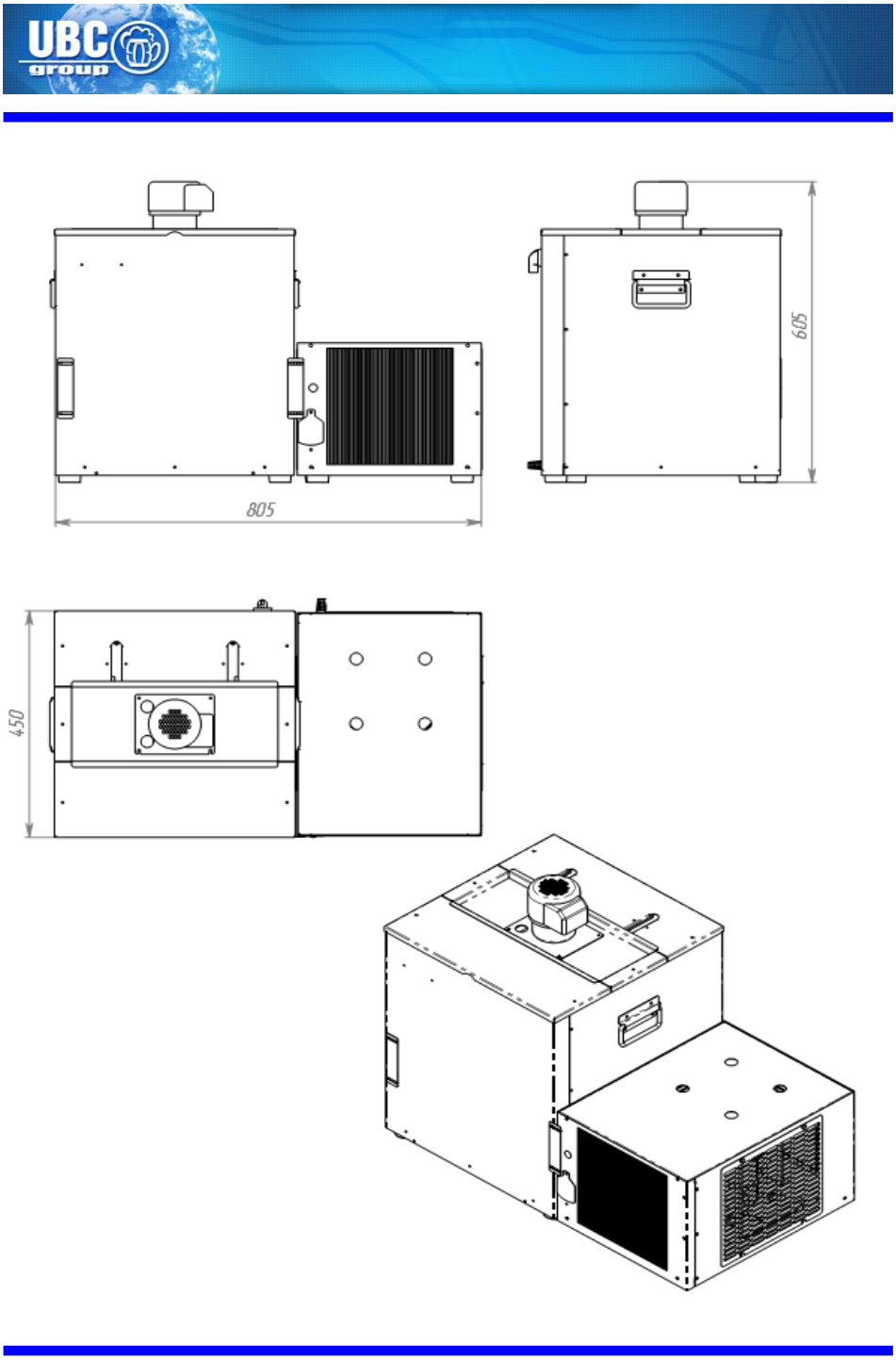

Figure D.3: Data sheet of the beer cooler (cont.)

Appendix E

Performances of the cooling system

The coefficient of performance of the refrigeration cycle is [8]:

$$COP = \frac{P_{evap}}{P_{comp}}$$

Knowing the temperatures at the entrance and exit of the evaporator could permit to compute the power absorbed by the refrigerant [8]:

$$P_{evap} = \dot{m}_{R134a} c_{p,R134a} \Delta T_{R134a}$$

From the data sheet in Appendix D, the power consumed by the compressor is:

$$P_{comp} = \frac{3}{8} h.p. = 279.638W$$

Sensors measuring the temperature of the misting solution at the entrance ($T_{in,1}$) and exit ($T_{in,2}$) of the cooler could be placed. With these data, the power released to cool the misting water would be [8]:

$$P_{in} = \dot{m} c_{p,w} (T_{in,1} - T_{in,2})$$

The efficiency of the heat exchangers could be computed.
At the cold side, the exchange occurs between the refrigerant and the cooling solution (glycol-water mixture) at the evaporator and between the glycol-water mixture and the misting solution [8].

$$\begin{aligned} \eta_{HE,cold} &= \frac{Q_{cold}}{Q_{evap}} \cdot \frac{Q_{in}}{Q_{cold}} \\ &= \frac{Q_{in}}{Q_{evap}} \\ &= \frac{\dot{m} c_{p,w} (T_{in,1} - T_{in,2})}{\dot{m}_{R134a} c_{p,R134a} (T_{R134a,1} - T_{R134a,4})} \end{aligned}$$

At the hot side, the exchange occurs between the refrigerant and the air of the greenhouse at the condenser.

$$\begin{aligned}\eta_{HE,hot} &= \frac{Q_{air}}{Q_{cond}} \\ &= \frac{\dot{m}_{air} c_{p,air} (T_{air,2} - T_{air,1})}{\dot{m}_{R134a} c_{p,R134a} (T_{R134a,2} - T_{R134a,3})}\end{aligned}$$

Bibliography

[1] D. D. Ackerly et al. "The Evolution of Plant Ecophysiological Traits: Recent Advances and Future Directions". In: *BioScience Vol. 50 No. 11* (2000), pp. 979–995.

[2] Analog Devices. *DS18B20*. Accessed: 14/04/2024. URL: https://www.analog.com/en/products/ds18b20.html.

[3] M. R. Anwar et al. "Adapting agriculture to climate change: a review". In: *Theoretical and Applied Climatology* (2012), pp. 225–245.

[4] M. Arifuzzaman et al. "Shovelomics for phenotyping root architectural traits of rapeseed/ canola (Brassica napus L.) and genome-wide association mapping". In: *Molecular Genetics and Genomics* (2019), pp. 985–1000.

[5] J. A. Atkinson et al. "Uncovering the hidden half of plants using new advances in root phenotyping". In: *Current Opinion in Biotechnology, 55* (2019), pp. 1–8.

[6] A. Banse. *LEPL1101, APP2 : solution*. GitHub. Accessed: 13/03/2024. URL: https://github.com/adrienbanse/LEPL1101_APP2/blob/master/regression_python.ipynb.

[7] Y. Bartosiewicz and M. Duponcheel. *LMECA2854 - Heat and mass transfer II*. Ecole polytechnique de Louvain, UCLouvain, 2023.

[8] Y. Bartosiewicz and M. Papalexandris. *LMECA1855 - Thermodynamique et énergétique*. Ecole polytechnique de Louvain, UCLouvain, 2022.

[9] J. E. Bradshaw. "Plant breeding: past, present and future". In: *Euphytica* (2017).

[10] C. Collet. *Chapter 2. A Simple Method to Convert Time Series of Root Tip Coordinates into Dynamic Representations of Plant Root Systems*. 2024.

[11] D. Dochain and M. Perrier. *Commande des Procédés*. Ecole polytechnique de Louvain, UCLouvain, 2024.

[12] Google Earth. *Google Earth*. Accessed: 22/05/2024. 2024. URL: https://earth.google.com/web/@50.66588399,4.62018673,141.5576735a,225.40104125d,35y,-0h,0t,0r/data=OgMKATA.

[13] D. Hainaut and L. Jacques. *LEPL1109 - Statistiques et science des données*. Ecole polytechnique de Louvain, UCLouvain, 2021.

[14] M. Hasanuzzaman et al. *Plant Ecophysiology and Adaptation under Climate Change: Mechanisms and Perspectives I*. Springer, 2020.

[15] Hopkins. *Physiologie végétale*. De Boeck & Larcier s.a., 2003.

[16] L. P. Huelsman. "Analog Electrical Filters". In: *Encyclopedia of Physical Science and Technology (Third Edition)*. Ed. by Robert A. MEYERS. 2003, pp. 519–530.

[17] F. P. Incropera et al. *Fundamentals of heat and mass transfer*. John Wiley & Sons, 2011.

[18] N. Jirafe. *How to filter noise with a low pass filter — Python*. Medium. Accessed: 08/04/2024. 2019. URL: https://medium.com/analytics-vidhya/how-to-filter-noise-with-a-low-pass-filter-python-885223e5e9b7.

[19] R. Kumari and R. Kumar. "Aeroponics: A Review on Modern Agriculture Technology". In: *Indian Farmer 6(4)* (2019), pp. 286–292.

[20] H. Majdi. "Root sampling methods - applications and limitations of the minirhizotron technique". In: *Plant and Soil, 185* (1996), pp. 255–258.

[21] G.S. Malhi, M. Kaur, and P. Kaushik. "Impact of Climate Change on Agriculture and Its Mitigation Strategies: A Review". In: *Sustainability* (2021).

[22] R. K. McGrail, D. A. Van Sanford, and D. H. McNear. "Trait-Based Root Phenotyping as a Necessary Tool for Crop Selection and Improvement". In: *Agronomy* (2020).

[23] S. J. Mooney et al. "Developing X-ray Computed Tomography to non-invasively image 3-D root systems architecture in soil". In: *Plant and Soil* (2012).

[24] R. Nair et al. "High frequency root dynamics: sampling and interpretation using replicated robotic minirhizotrons". In: *Journal of Experimental Botany, Vol. 74, No. 3* (2023), pp. 769–786.

[25] Paneltim. "Brochure constructie panelen". In: ().

[26] S. Prabhakaran. *Interpolation in Python – How to interpolate missing data, formula and approaches*. Machine Learning +. Accessed: 02/04/2024. URL: https://www.machinelearningplus.com/machine-learning/interpolation-in-python-how-to-interpolate-missing-data-formula-approaches/?utm_content=cmp-true.

[27] Professional Plastics. *Thermal Properties of Plastic Materials*. Accessed: 19/03/2024. URL: https://www.professionalplastics.com/professionalplastics/ThermalPropertiesofPlasticMaterials.pdf.

[28] M. Shouran and E. Elgamli. "Design and Implementation of Butterworth Filter". In: *International Journal of Innovative Research in Science, Engineering and Technology, Volume 9, Issue 9* (2020), pp. 7975–7983.

[29] A. Shrestha and B. Dunn. "Hydroponics". In: *Division of Agricultural Sciences and Natural Resources, Oklahoma State University* (2010).

[30] A. L. Smit et al. *Root Methods: A Handbook*. Springer, 2000.

[31] The Editors of Encyclopædia Britannica. *Genetics*. Britannica. Accessed: 08/06/2024. 2024. URL: https://www.britannica.com/science/genetics.

[32] The Editors of Encyclopædia Britannica. *Root*. Britannica. Accessed: 08/04/2024. 2024. URL: https://www.britannica.com/science/root-plant.

[33] S. Trachsel et al. "Shovelomics: high throughput phenotyping of maize (Zea mays L.) root architecture in the field". In: *Plant Soil, 341* (2011), pp. 75–87.

[34] L. Vandendorpe and Wertz V. *LEPL1106 - Signaux et systèmes*. Ecole polytechnique de Louvain, UCLouvain, 2021.

[35] Wikipedia contributors. *Euler method*. Wikipedia. Accessed: 26/03/2024. 2024. URL: https://en.wikipedia.org/wiki/Euler_method.

[36] Wikipedia contributors. *Linear interpolation*. Wikipedia. Accessed: 02/04/2024. 2024. URL: https://en.wikipedia.org/wiki/Linear_interpolation.

[37] S. Zappala et al. "Effects of X-ray dose on rhizosphere studies using X-ray computed tomography". In: *PloS one, Vol. 8, Issue 6, e67250* (2013).

UNIVERSITÉ CATHOLIQUE DE LOUVAIN
École polytechnique de Louvain
Rue Archimède, 1 bte L6.11.01, 1348 Louvain-la-Neuve, Belgique | **www.uclouvain.be/epl**